Title

Investigations of fault zone behavior during earthquake cycles using hydrology and geodesy

Author

Xue, Lian

Publication Date

2015

UNIVERSITY OF CALIFORNIA
SANTA CRUZ

Investigations of fault zone behavior during earthquake cycles using hydrology and geodesy

A dissertation submitted in partial satisfaction of the
requirements of the degree of

DOCTOR OF PHILOSOPHY

in

EARTH SCIENCES
with an emphasis in GEOPHYSICS

by

Lian Xue

September 2015

The Dissertation of Lian Xue is approved:

Professor Emily Brodsky, Chair

Professor Susan Schwartz

Professor Thorne Lay

Professor Andrew Fisher

Tyrus Miller
Vice Provost and Dean of Graduate Studies

Table of Contents

List of figures

Investigations of fault zone behavior during earthquake cycles using hydrology and geodesy

Lian Xue

Abstract

This study investigates processes of three stages of the earthquake cycle: interseismic, post-seismic and coseismic periods. For the inter-seismic period, this thesis explored the inter-seismic strain accumulation on the Nicoya Peninsula, Costa Rica integrating InSAR and GPS data. This work demonstrates that the InSAR data can be used to recover small deformation signal of long wavelength with refined resolution when integrated with GPS observations. The spatial correlation between the distribution of coupling and the locations of slow slip events and low frequency events suggests that fluid and frictional heterogeneities may be the two main factors influencing coupling variations in the Nicoya, Costa Rica subduction zone. For the coseismic period, this thesis studied the coseismic friction associated with the 2008 M_W 7.9 Wenchuan Earthquake using repeat measured temperature profiles across the fault slip zone, since measuring the heating signal on the fault zone after an earthquake is the most direct and efficient way to quantify the coseismic friction. The long-term temperature records following the Wenchuan Earthquake are consistent with low coseismic friction. The observed thermal anomalies above and within the fault zone cannot be the frictional transient from faulting and are likely a result of advective flow. For the post-seismic period, this thesis investigated the healing process after the Wenchuan Earthquake. The hydrogeologic properties of the fault zone can serve as a proxy for fracturing and the post-seismic recovery of fault strength, which is one of the major unconstrained elements of the earthquake cycle. We used continuous monitoring of borehole water response to tidal forcing to measure the continuous in-situ permeability properties of the Wenchuan Earthquake fault damage zone. Observed

post-seismic episodically decreasing permeability over time indicates an interaction between the healing and damage in the aftermath of a major earthquake.

Acknowledgments

I would like to express my highest gratitude to my advisor Prof. Emily Brodsky. I thank her for leading me to the field of earthquake physics which was totally new to me in my first year. I was lucky to get involved in the project of Wenchuan Drilling Program to start my long time journey to find what I am really interested in and want to pursue. Every time when I struggled or got frustrated, her strong support through her guidance, encouragement and passion in science, let me not give up on the journey. Emily is not only an advisor but also a great mentor. She cares a lot about my development of scientific career skills, such as presentation. Without her training, I could not communicate science with other people well. Without her, I could not find my interests in earthquake physics and find it fun to pursue this as a life career.

I also would like to express great gratefulness to my research committee: Prof. Susan Schwartz, Prof. Thorne Lay and Prof. Andrew Fisher. I thank them for their insightful comments and advice. Great thanks to Prof. Susan Schwartz for her advice and encouragement. Without her encouragement and advice, I could not finish the geodetic project of Costa Rica and regain interest in geodesy. I also want to thank her for giving me a chance to join the seismology group in Santa Cruz. Without her, I could not be here. Great thanks to Prof. Thorne Lay. His great advice always makes me move forward and find a new view of a problem. Great thanks to Prof. Andy Fisher. He gave me lots of advice on my projects including and beyond hydrology.

He also taught me how to prepare the field work of borehole logging to let my first borehole logging experience be a success. I was so lucky to be teaching assistant with him to let me learn from a good teaching experience.

Great thanks to all of my co-authors, especially to Dr. Patrick Fulton, Dr. Zhen Liu, Dr. Haibing Li, Dr., Dr. Rob Harris, Dr. Kano, Dr. Jim Mori and Dr. Feng Lujia. I thank all of them for their collaborations and comments on the projects. I thank Patrick for his advice and patient guidance, discussion and sharing of his views of sciences, especially of the fault zone hydraulic and thermal process, and his teaching on the construction of numerical models. I thank Zhen for his advices and guidance on my geodetic project. Under his advice, I mastered solid skills of InSAR analysis and inversion. Without his help, I could not finish the Costa Rica project.

I also want to send my great thankfulness to the faculty members who taught classes to me, particularly Prof. Francis Nimmo and Prof. Patrick Chuang, whose Order of Magnitude Estimation is the most interesting and helpful class I have had; Prof. Andrew Fisher, whose grounder water modeling filled in the gap of my knowledge of hydrology and the related modeling; Elise Knittle, whose Mineralogy class taught me the knowledge of rocks.

I also want to thank my colleagues. Thank our little hydro-physical group: Patrick Fulton, Vincent Allègret and Thibault Candela. We solved and discuss tough problems together. They make me feel not alone in the field, even though we are one of the rare groups using tidal response. Great thanks to seismogroup: Yaofeng He, Yingcai Zheng, Lia Lajoie, Stephen Hernandez, Nicholas van der Elst, Megan Avants, Lingling Ye, Erin Todd, Stephanie Taylor, Grace Barcheck, Esteban Chaves Sibaja and Qingjun Meng. Thank them for the happy time and discussions of our study and work. I am so glad to become one member of the Slug Seismogroup.

I also want to express my thanks to the staff in our department front office, especially to Jennifer Fish, Amy Kornberg and Ed Boring. I thank them for their warmness and patient help. They are always kind and they efficiently solve the problems I brought to them every time.

I would like to send my grateful thankfulness to my beloved family. My family's love makes me always feel warm and connected to them even when I am far away from them. Great thanks to my parents, especially to my mom. I thank her for her deep love and strong support for me. Without her understanding, I could not become myself at this point and work on the field I like. Great thanks to my husband Han Yue. I thank him for sharing every moment with me for a long time. The best thing in life is having each other. I thank greatly and miss my grandfather. His love made me become a strong woman. I am deeply regretful that I could not be there when you passed away. Your encouragement accompanies with me all the time.

Great thanks to my friends. They bring great joy to my life and share their views of the world. Thanks to Abbey Chrystal. She helped me to know the local culture and make friends. She makes me feel I am not alone in Santa Cruz. Thanks to XiaoFei Pu who is like one of my sisters. We shared our joy and sadness at every moment after we came to America even when we are across the whole country. Thanks to Neesha Schnepf. I missed her laughing so much. Her attitude to life makes me more positive. Thanks my friends in Santa Cruz, especially for Sai Xiao, JiaZhong Nie. Thanks for the happy time we spent together. Thanks to our little group: QingJun Meng, Bo Chen, Fei Wu and Lin Jin. Thank them for sharing good times, jokes and food with me when I live alone. Many thanks to my friends in China. Every time when I came back to China, the happy time spent with them made me laugh often even when I was in Santa Cruz.

Great thanks to the people who helped me on the field work. For the people who helped me to do the stop-go logging in the Wenchuan borehole1: Guang Yang, Zheng Gong, Jialiang Shi, Zhi-Ming Sun, Kun Yun, and Yunlong Li. I remembered the time we spent together to get the precious logging data over 20 hours working. I also want to thank the people help me on the Logan Quarry Logan: Patrick Fulton, Vincent Allègre, Thibault Candela, Reed Carter, Barbara E. John and Han Yue.

Great thanks to the Chinese Christian fellowship in Santa Cruz, especially to Husing Papa and Mama, XiangLing Zhang, Jeanny Ji, CY Tung and Grace Tung. It is like another family for us in Santa Cruz. Thanks for bringing the peace in my heart when I had a hard time. Thanks for Peggy Pollard for her kindness and help to me.

Introduction

Earthquake cycles include interseismic, coseismic and post-seismic periods. Between large earthquakes, the strain accumulates in the crust adjacent to major faults during the interseismic period. When the accumulated strain exceeds the strength of the fault plane, the accumulated strain is released by a seismic rupture. Afterwards, fault strength recovers and stress is continuously released postseismicly. Observing the fault zone behavior during each of these stages is important to understanding the development of earthquakes. In this thesis, I focus on investigating fault zone behavior during earthquake cycles using hydrology, geodesy and borehole temperature.

Interseismic Period

The accumulated strain energy during the interseismic period determines the energy released coseismicly. Assessing the interseismic accumulated strain therefore is very important to estimate the potential earthquake hazards and the frictional properties of the plate interface. For more than two decades, geodesy, such as Global Positioning System (GPS) and Interferometric Synthetic Radar (InSAR), has been the primary tool used to measure interseismic deformation and interrogate the degree of locking on the fault plane. In general, GPS data provide excellent temporal resolution but have poor spatial coverage. In contrast, InSAR can alleviate these inadequacies, thus providing an excellent complement in spatial resolution to GPS observations but with coarse temporal sampling (e.g., days to weeks). The combination of InSAR and GPS therefore will achieve better resolution of ground deformation, especially for subtle deformation signals.

Chapter 1 reports on the interseismic deformation on the Nicoya Peninsula, Costa Rica as determined by joint inversion of InSAR and GPS data. I developed new codes to extract the deformation signal from the InSAR time-series, and to invert the coupling pattern of the plate interface. Even though measuring the deformation on the subduction zone using InSAR is challenging, our study shows InSAR data can be used to recover small, long wavelength deformation signals with refined resolution when integrated with GPS observations. Incorporating InSAR data provides a more refined interseismic coupling model than using GPS alone and allows for a more reliable comparison with local seismic and aseismic activity. This comparison indicates that strongly locked regions during the interseismic stage are the loci of coseismic slip, and deep slow slip and low frequency earthquakes occur in regions of low coupling or transition zones from low to high coupling, while shallow slow slip and tremor commingles with strongly coupled regions. The spatial correlation between the distribution of coupling and the locations of slow slip events and low frequency events suggests that fluid and frictional heterogeneities may be the two main factors influencing coupling variations on the Nicoya, Costa Rica subduction zone. This work is published on JGR.

Coseismic Period

The coseismic friction is of paramount importance in earthquake mechanics, as it determines the resisted shear stress, the stress drop, the mechanical work and the coseismic frictional heat during slip. However, the coseismic friction has long been unknown. Recent measurements have shown that a straightforward application of Byerlee's law with a coefficient of friction of 0.6 for most rocks and 0.2 for clays may not yield the correct shear stress at high speed slips. At typical earthquake slip velocities of 1 m/s, laboratory values of friction plummet and span a range of values from 0.05 to 0.4, depending on lithology and experimental conditions. The theory controlling high-velocity friction is vigorously debated, and nonfrictional processes can alter the local shear stress in natural systems. Field measurements are needed to constrain the magnitude of shear resistance during earthquakes on actual faults. To address this observational gap, rapid response drilling projects have measured the temperature in a fault zones directly after major earthquakes. Since most coseismic friction energy is dissipated as heat, measuring the temperature on the fault after an earthquake is the most direct and efficient way to quantify the coseismic friction.

Chapter 2 represents borehole temperature measurements made across the fault zone that ruptured during the 12 May 2008 Mw 7.9 Wenchuan (Sichuan province, China) earthquake, continuing from 1.3 to 5.3 yr after the event. Repeated temperature profiles measured within the fault zone for four years show two thermal anomalies with constant amplitude and width over time. The anomalies cannot be the frictional transient from faulting and are likely a result of advective flow. This temperature data and thermal conductivity measurements place an upper bound on the coseismic friction on the fault. This work is published and fully described in Li et al. (2015).

Postseismic Period

Fault zone permeability serves as a proxy for fracturing and healing as the fault regains strength during one of the most unconstrained phases of the earthquake cycle. Because earthquakes generate fractures in a damage zone around a fault, following a large earthquake, the fault zone permeability should transiently increase. Over time, the permeability may decrease as a result of a combination of chemical and mechanical processes. Measuring the evolution of in situ fault zone hydrogeologic properties can capture the healing processes after an earthquake. However, such measurements require post-earthquake rapid response drilling, and prior to our work appropriate data had not been recorded continuously immediately after a large earthquake.

Continuous observations of water tidal response provide a unique probe to investigate in-situ fault zone hydraulic properties and track its evolution over time. The tidal forcing imposes a dilatational strain on the surrounding rock formation that pumps water cyclically in and out of the well through the rock around the open interval of the well. The transmissivity and storage coefficient determine the phase and amplitude response of the water level to the tidal loading. To first order, phase lag is inversely related to transmissivity, and amplitude response is inversely proportional to storage coefficient. Using the tidal response to measure hydrogeologic properties has two distinct advantages. Firstly, the tidal response is passive and records the in situ properties undisturbed by repeated pump tests or water injections. In addition, the tidal response provides a continuous record of temporal changes of hydrogeologic properties in the rocks below the main rupture zone.

The hydrogeology properties of fault zones also help govern the initiation and propagation of earthquakes. The increase of pore pressure weakens fault zones by reducing the effective stress. During fault slip, how the pore pressure changes depends on the hydrogeologic properties of fault zone. It is therefore very important to establish the in-situ fault zone hydrogeologic structure. Fault zone architecture can be constrained by water tidal response utilizing an array of wells with various distances to the fault zone. Each well samples its own surrounding formation, therefore the array can provide a map of the hydrogeologic properties of the fault zone.

Chapter 3 is the investigation of the healing process after the Wenchuan Earthquake. Water level inside a borehole across the main rupture zone was observed for one and half years after the Wenchuan Earthquake. I analyzed the water level response to tidal forcing to capture the evolution of the permeability after the major earthquake. The observed episodically decreasing permeability over time after the Wenchuan earthquake indicates an interaction between the healing and damage processes in the aftermath of a large earthquake. This is the first direct, continuous hydrologic record of the healing process after a major earthquake. This work is published in Science.

Chapter 4 is a theoretical study of water tidal response. The analysis of water level tidal response assumes the confined aquifer is homogeneous and isotropic. It however is expected that fault zones are strongly anisotropic and heterogeneous. I worked on addressing the problematic assumption of isotropy in the original method. To explore the effect of the anisotropic horizontal flow on water level response to tidal forcing, I used a finite element method. This numerical model showed that the effective permeability is the geometric mean of the permeability in the two principal directions for weakly anisotropic media, and is a lower bound of the permeability in the fast principal direction for strong anisotropy. This helps to quantify the possible range of the permeability measured by water level tidal response under an anisotropic system.

Chapter 5 presents the hydraulic architecture of the San Andreas Fault near the Logan Quarry. I investigated the in-situ hydraulic architecture of the San Andreas Fault zone near the Logan Quarry using water tidal response. The fault zone hydrogeologic architecture is constrained by utilizing an array of wells with various distances to the San Andreas Fault zone near the Logan Quarry. The measured specific storage and permeability show that there is a localized zone near the fault zone (with distance $<$ 40 m) where both the specific storage and permeability are higher than in the surrounding region.

Chapter 1. Interseismic megathrust coupling beneath the Nicoya Peninsula, Costa Rica, from the joint inversion of InSAR and GPS data

Lian Xue[1], Susan Schwartz[1], Zhen Liu[2], Lujia Feng[3]

1. Department of Earth and Planetary Sciences, University of California, Santa Cruz, CA 95064, USA.

2. Jet Propulsion Laboratory, California Institute of Technology, 4800 Oak Grove Drive, Pasadena, CA 91109, USA

3. Earth Observatory of Singapore, Nanyang Technological University, 50 Nanyang Ave, N2-01C-36, Singapore.

*This paper is published as Xue, L., S. Schwartz, Z. Liu, and L. Feng (2015), Interseismic megathrust coupling beneath the Nicoya Peninsula, Costa Rica, from the joint inversion of InSAR and GPS data, Journal of Geophysical Research: Solid Earth, 120(5), 2014JB011844.

Abstract

The Nicoya Peninsula, Costa Rica, was struck by a long-anticipated and gap-filling M_W 7.6 earthquake in 2012. To study interseismic strain accumulation on the megathrust beneath the Nicoya Peninsula, we present an improved interseismic coupling model by integrating InSAR and GPS data. Our model reveals three strongly

coupled patches. The first strongly coupled patch locates beneath the Nicoya Peninsula and ruptured during the 2012 earthquake. The second strongly coupled patch locates offshore the central Nicoya Peninsula and remained largely unbroken. However, this region is close to and possibly intermingled with shallow slow slip and tremor, suggesting that accumulated strain in this region may be released both seismically and aseismically. The third strongly coupled patch offshore of the southeastern end of Nicoya overlaps part of the coseismic rupture of the 1990 M_W 7.0 Nicoya Gulf earthquake, indicating that significant strain has re-accumulated since this event. Incorporating InSAR data provides a more refined interseismic coupling model than using GPS alone and allows for a more reliable comparison with local seismic and aseismic activity. This comparison indicates that strongly locked regions during the interseismic stage are the loci of coseismic slip, and deep slow slip and low frequency earthquakes occur in regions of low coupling or transition zones from low to high coupling, while shallow slow slip and tremor commingles with strongly coupled regions. Our study demonstrates that InSAR data can be used to recover small long wavelength deformation signals with refined resolution in challenging subduction zone environments when integrated with GPS observations.

1-1 Introduction

Subduction zones generate the Earth's largest and most destructive earthquakes. The mechanical properties of the plate interface at subduction zones can be highly heterogeneous. Regions that accumulate strain during the interseismic period have been shown to be the loci of large coseismic slip [e.g., *Loveless and Meade*, 2011;

Metois et al., 2012; *Yue et al.*, 2013; *Zweck et al., 2002*], while adjacent areas often host microearthquakes, slow slip or seismic tremor [*Schwartz and Rokosky*, 2007]. In order to image the heterogeneity of the subduction zone interface and assess potential future seismic hazards, interseismic coupling on the plate interface must be determined.

For more than two decades, the Global Positioning System (GPS) has been a primary tool used to measure interseismic deformation and interrogate the degree of locking on the plate interface at subduction zones [e.g., *Dixon*, 1993, *Hyndman et al.*, 1995; *Mazzotti et al.*, 2000]. In general, GPS data provide excellent temporal resolution but have poor spatial coverage. In contrast, Interferometric Synthetic Radar (InSAR) data can alleviate these inadequacies, thus providing an excellent complement in spatial resolution to GPS observations but with coarse temporal sampling (e.g., days to weeks). Recently, InSAR has been widely used to measure coseismic deformation at subduction zones [e.g., *Biggs et al.*, 2009; *Pritchard and Fielding*, 2008; *Pritchard et al.*, 2002; *Tong et al.*, 2010], however, using InSAR to measure subtle, long-wavelength signals, such as interseismic deformation remains a challenge. The primarily offshore location of strain accumulation and concomitant low amplitude interseismic deformation on land has impeded the success of InSAR in subduction zone environments. Therefore, most interseismic deformation studies using InSAR have been focused on continental fault zones [e.g., *Biggs et al.*, 2007; *Cavalié et al.*, 2008; *Fialko*, 2006; *Gourmelen et al.*, 2010]. Very few InSAR interseismic studies have been published for subduction zones [*Bejar-Pizarro et al.*, 2013; *Cavalié et al.*, 2013; *Hooper et al.*, 2012]. The Nicoya Peninsula in Costa Rica lies directly above the seismogenic zone, which greatly improves its vantage point. The acquisitions of high quality L-band SAR observations over the Nicoya Peninsula between 2007 and 2011 enable us to construct an improved interseismic deformation map constrained by both InSAR and GPS data.

The Nicoya Peninsula is located directly above the subduction zone interface where the Cocos and Caribbean Plates converge at a rate of approximately 8 cm/yr [*DeMets et al.*, 2010] (Figure 1-1). The peninsula's unique location and the presence of a dense operating GPS and seismic network [*Outerbridge et al.*, 2010; *Walter et al.*, 2011] have made it a prime region to study strain accumulation and release at a subduction zone. During the last 160 years, four large megathrust earthquakes occurred beneath the Nicoya Peninsula in 1853, 1900, 1950 (*M*w 7.7) and 2012 (*M*w 7.6) [*Protti et al.*, 2014]. Moreover, since 2003 GPS and seismic networks on the Nicoya Peninsula have recorded seven slow slip events (SSEs) accompanied by tremor [*Dixon et al.*, 2014, *Jiang et al.*, 2012; *Outerbridge et al.*, 2010; *Walter et al.*, 2011]. The most recent 2012 M_W 7.6 Nicoya earthquake ruptured a significant portion of a large locked patch previously identified using GPS data alone [*Feng et al.*, 2012], leaving another identified locked region offshore of the northwestern Peninsula unbroken [*Protti et al.*, 2014]. Understanding the detailed spatial distribution of the locked and creeping patches to assess whether the fully locked patches are distinct from and/or surrounded by slowly slipping regions is particularly important for earthquake hazard studies [*Schwartz and Rokosky*, 2007]. To better determine the location and size of locked patches and compare them to the ruptured and slow slipping regions, this paper provides an improved interseismic coupling model by integrating InSAR and GPS data.

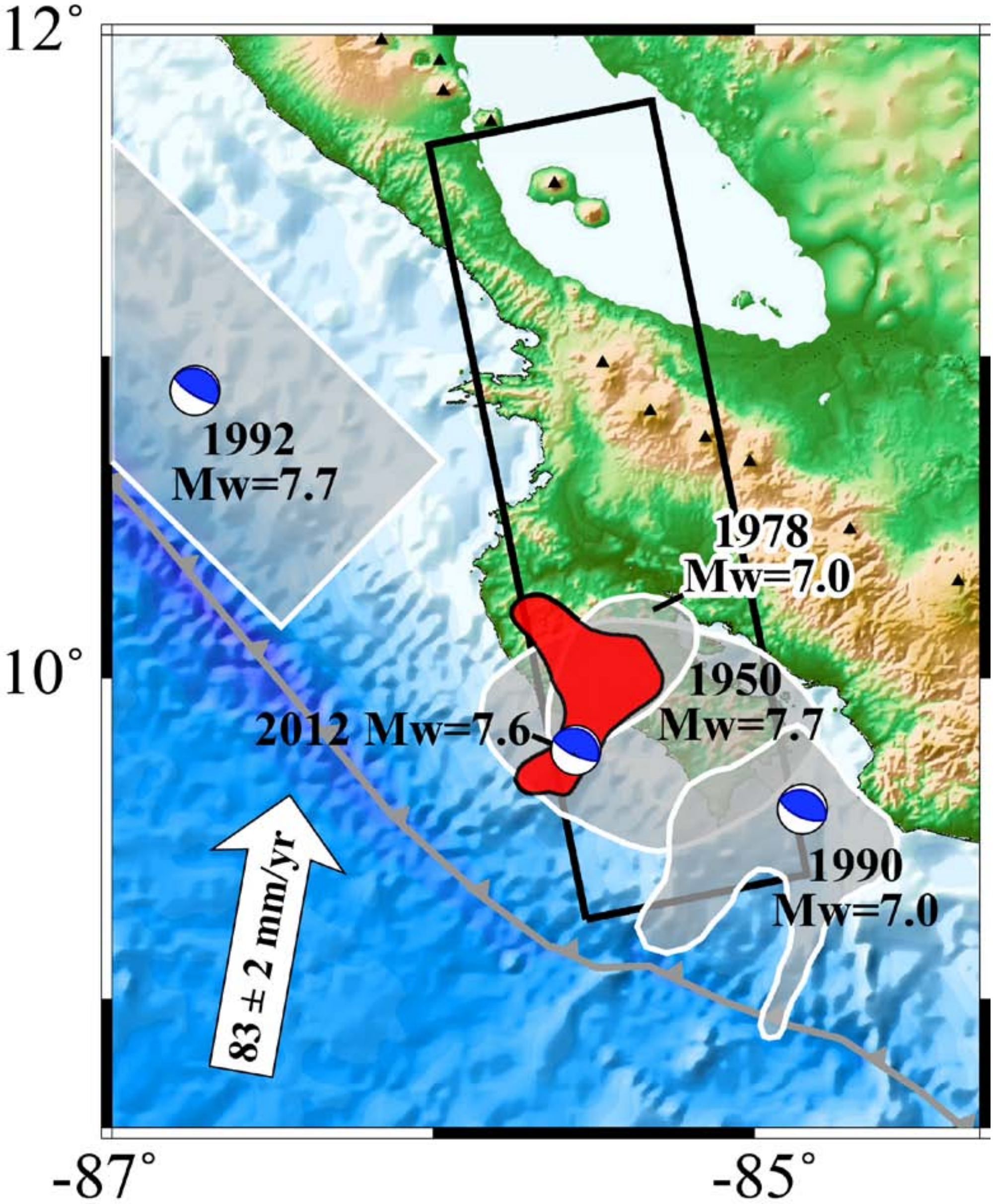

Figure 1-1. The tectonic setting of the Nicoya Peninsula. Aftershock areas of the 1950, 1978, 1990, and 1992 events are indicated with gray-filled patches. The

coseismic region of the 2012 event is shown as the red-filled patch [Yue et al., 2012]. Focal mechanisms for the 1990, 1992 and 2012 events from the global CMT catalog are also indicated. The black rectangle indicates ALOS PALSAR track 164 used in this study. The white arrow indicates the convergence vector between the Cocos and Caribbean Plates [DeMets et al., 2010]. The trench is marked with the gray barbed solid line. The black triangles are the Holocene active volcanoes [Siebert and Simkin, 2002].

1-2 InSAR data and analysis

We use the L-band SAR data from the Advanced Land Observing Satellite (ALOS) Phase Array L-band Synthetic Aperture Radar (PALSAR) with ~23.6 cm wavelength. The dense vegetation on the Nicoya Peninsula limits the use of SAR data with shorter wavelengths because of low coherence of available interferograms. The SAR images were collected from January 2007 to October 2010 and are now archived at the Alaska Satellite Facility. Unfortunately, the ALOS PALSAR ceased operation in March 2011. Three ascending and three descending tracks are available for this region. However, the descending tracks have too few scene acquisitions and the two adjacent ascending tracks have poor spatial coverage over our region of interest. Therefore, in our analysis, we only use ascending track 164 that provides enough SAR acquisitions and covers nearly the entire area of the Nicoya Peninsula (Figure 1-1) to image its interseismic deformation.

1-2.1 InSAR data processing

We processed 18 SAR acquisitions from track 164 between 2007 and 2010 by using the JPL/Caltech Repeat Orbit Interferometry Package (ROI_PAC) [*Rosen et al.*, 2004], version 3.0.1. We constructed 120 possible interferograms with perpendicular baselines less than 1200 m. We used a SRTM3 DEM, which has a 90 m resolution (downloaded from http://dds.cr.usgs.gov/srtm/version2_1/SRTM3/South_America/), to remove the topographic phase from the interferograms. Decorrelation of the interferograms is significant due to the heavy vegetation of the Nicoya Peninsula, so we reduced (complex averaged) the interferograms in the range and azimuth direction by 16 and 32 pixels to improve the signal coherence, resulting in a pixel size of ~75 m×113 m in radar coordinate. We used the SNAPHU program [*Chen and Zebker*, 2000] to unwrap the phase. We used a triplet stacking phase which forms a loop as an indicator for the unwrapping errors [*Biggs et al.,* 2007]. Very localized unwrapping errors might still remain in the interferograms, but these are typically small and do not introduce major errors into the analysis of the interferograms.

1-2.2 Orbital error correction

One of the main issues in InSAR analysis is proper removal of residual orbital errors. These errors contribute to phase artifacts in the interferograms because of uncertainty in orbital parameters. Typical orbital errors are on the order of ~0.19 mm/km over space [*Fattahi and Amelung*, 2014; *Hanssen*, 2001]. To avoid tectonic signals being masked by long wavelength orbital signals, a correction for the residual orbital signals is necessary. However, because of the spatially long-wavelength nature of interseismic deformation [e.g., *Bürgmann et al.*, 2000; *Simons and Rosen*, 2007], it is difficult to identify a subregion that is completely free of the deformation signal in order to estimate and correct for orbital errors. Moreover, the distribution of GPS stations is sparse in the northern region of the Nicoya Peninsula, so accurate corrections cannot be made using these GPS stations alone. Therefore, we corrected for residual orbital signals using a GPS-derived interseismic strain accumulation model from *Feng et al.*, [2012]. The long wave length deformation information in the corrected InSAR data is maintained and should be similar to the GPS data. Since this GPS-derived interseismic model includes all of the GPS stations and fits the observations very well, it provides reliable information on the long wave length deformation

First, we projected the predicted horizontal and vertical components of the GPS-derived interseismic velocities to the line of sight (LOS) direction by using a unit vector of LOS [0.60, 0.13, -0.79] in the east, north, and vertical directions. Then we removed the predicted LOS deformation from the unwrapped interferograms and applied a polynomial fit to remove the residual orbital error. Finally, we added the predicted LOS deformation back to the signals. This correction is similar to the SURF approach of *Tong et al.*, [2013]. We do not observe significant stratified atmospheric noise in the remaining phase signal, so no correction for stratified atmospheric noise is included. We chose a point outside of the deformation region as a reference (Figure 1-3), and subtracted the mean value of the pixels around the reference point from all pixels in the images. This reference point also collocates with a campaign GPS station (BAGA) with a LOS velocity of ~9 mm/yr which is relatively small compared with the other stations in the forearc region.

1-2.3 Stacking

In order to access whether InSAR can detect the interseismic deformation signal, we constructed a simple rate map by stacking. We selected eight corrected SAR interferograms, whose perpendicular baseline is <300m, and temporal duration is >2 yr, to construct a time weighted stacked image. Repetitions of the selected master or slave SAR acquisitions (Figure 1-2) are limited to no more than four. Assuming the interseismic deformation accumulates at a constant rate, the stacked velocity for each

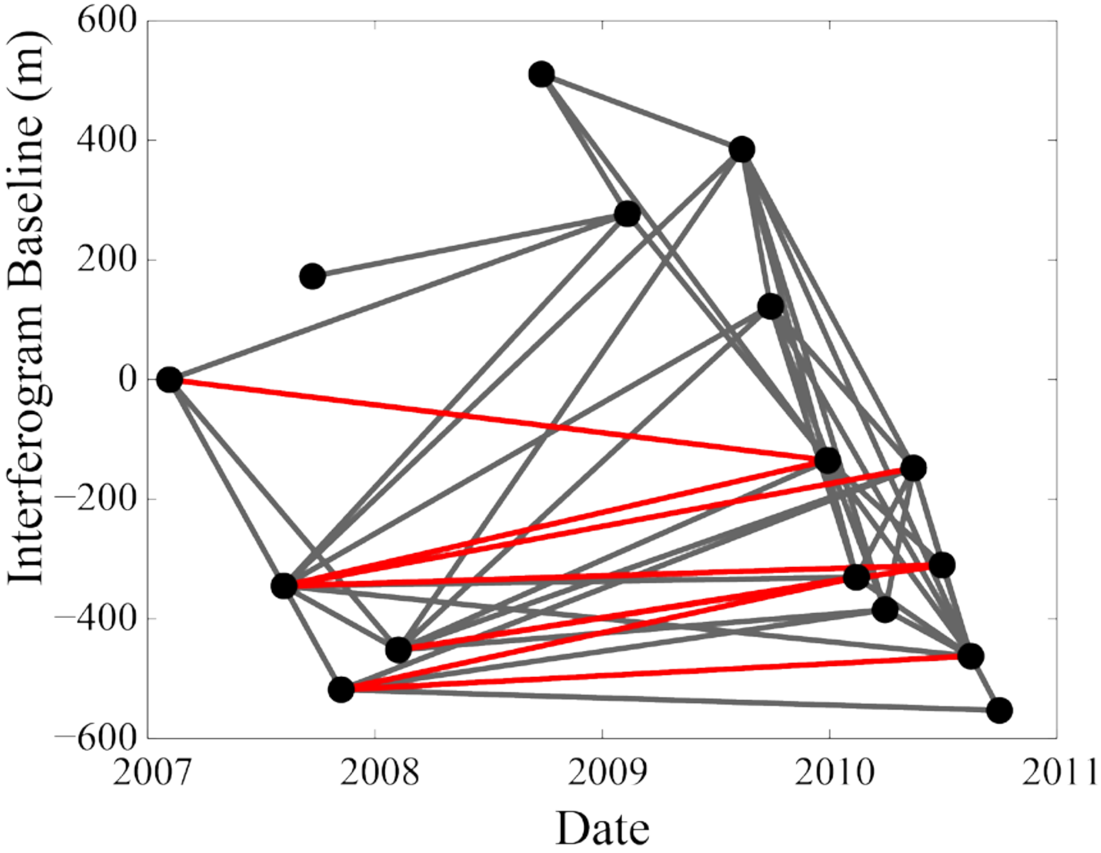

Figure 1-2. Time interval and spatial baseline of the 52 interferograms. The red lines indicate the interferograms selected for stacking.

pixel can be expressed as $d_a = \sum_i^n d_i \Big/ \sum_i^n T_i$, where d_a is the average displacement over one year, d_i is the *ith* displacement during time T_i, and n is the number of selected pairs. The interferograms with longer time intervals contribute more to the stacking result. Stacking is based on pixels, and the number of interferograms used for stacking can be different for each pixel. The resultant LOS rate map shows two significant regions of deformation in the southern part of the peninsula with magnitudes of ~10-15 mm/yr, comparable to the GPS observations. It also shows deformation features that are correlated with the location of volcanoes that are not obvious in the GPS measurements. In general the stacked rate map is noisier near the coastal region and northern portion of the image than the rest of the area (Figure 1-3).

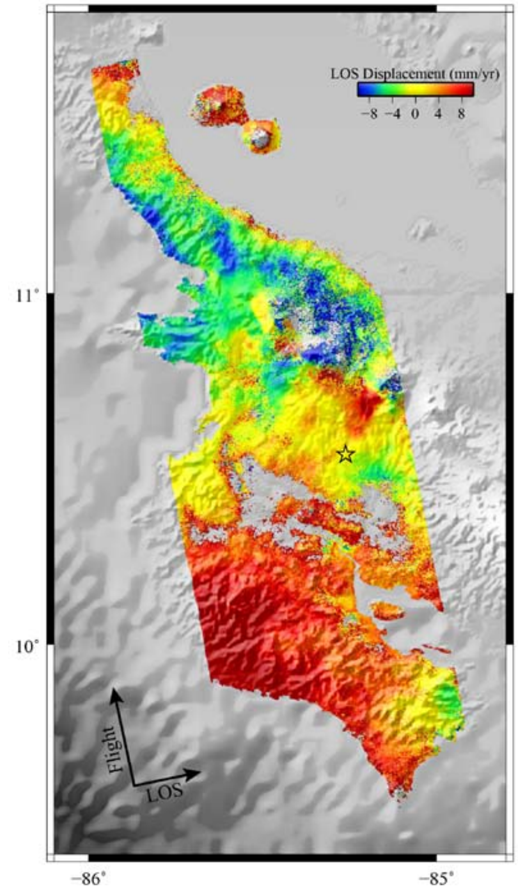

Figure 1-3. Average velocity map constructed by stacking the eight interferograms with durations longer than two years and baselines under 300 m. The arrow shows the line of sight and flight directions. Positive displacements indicate surface motion away from the satellite. The black star indicates the reference point.

1-2.4 Time series

To make use of all available SAR data, we used the small baseline subset (SBAS) method to invert for the LOS displacement time series from January 2007 to October 2010 at each pixel [*Berardino et al.*, 2002]. First, we used all possible interferograms to construct a time series, and calculate the root mean square (RMS) difference between the observed interferograms and the reconstructed interferograms from the inverted time series for all the interferograms [*López-Quiroz et al.*, 2009]. We then chose 54 interferograms with the smallest RMS (Figure 1-2) to invert for the final time-series. We applied a Gaussian function with a half width of 0.25 year as a temporal smoothing filter to the final time-series to suppress atmospheric noise [e.g., *Berardino et al.*, 2002; *Liu et al.*, 2011]. The final time-series still have considerable scatter due to residual atmospheric noise. Examination of individual time series shows no clear signals related to known SSEs that occurred in 2007 and 2009 during the InSAR data period [*Jiang et al.*, 2012]. Since we are focused on average "interseismic" strain accumulation (see discussion in Section 5.1), we estimated a constant linear velocity by using linear regression of the time series for each coherent pixel. Scattering in the InSAR residual LOS time series after linear fitting is ~5.4 mm, and the typical total displacement of the slow slip events in the LOS direction is ~ 6.4 mm. This suggests that using InSAR time series to detect transient slow slip events in this region will be challenging. The major features of the linear rate map are similar to the stacking result (Figure 1-4), but the linear rate map shows a much cleaner pattern (Figure 1-3). Our ultimate goal is to combine the linear rate map from the InSAR time series analysis and GPS velocities to construct an interseismic coupling model.

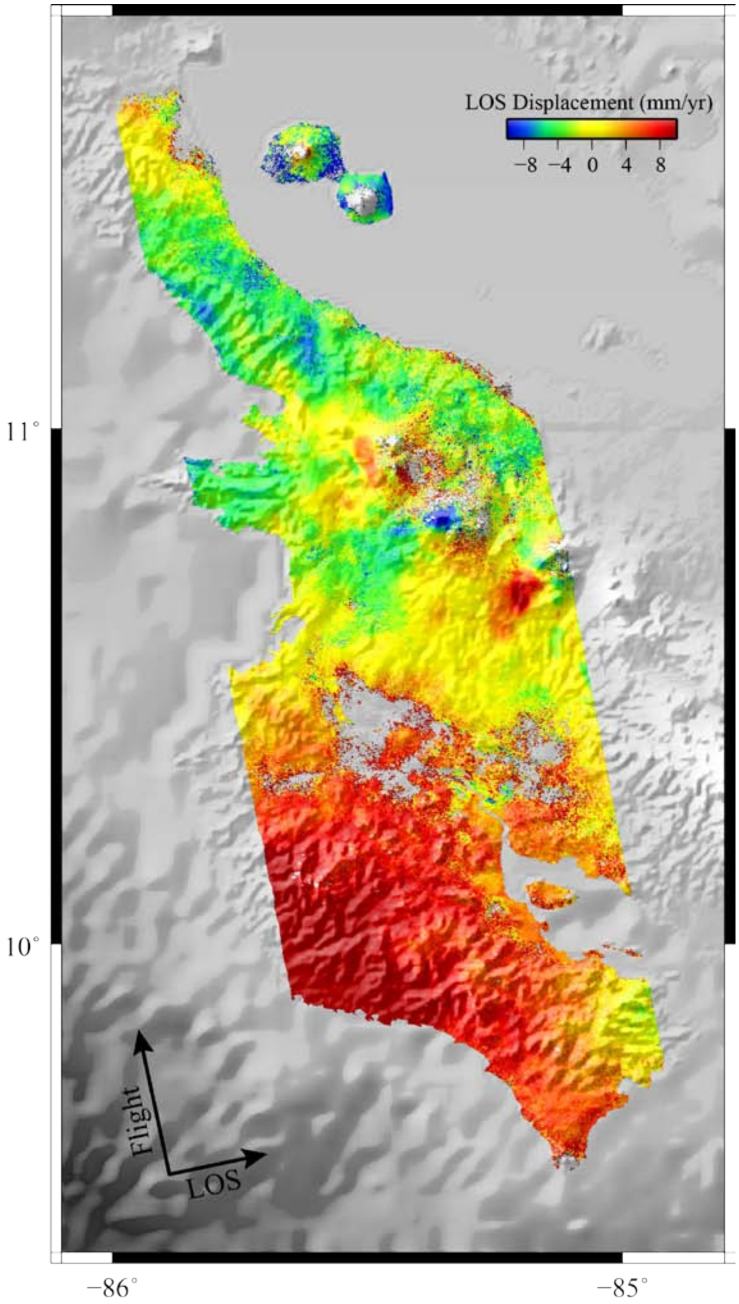

Figure 1-4. Linear deformation rate map derived from the linear regression of the deformation time series at each pixel. Positive displacements indicate surface motion away from the satellite.

Since the InSAR image has tens of thousands of data points, we applied a quadtree algorithm based on variance change to downsample the InSAR linear rate map [*Jónsson et al.*, 2002]. For the variance threshold of 0.81 cm^2, the downsampled linear rate map approximates the original LOS displacement well (see Supplementary Material). Since the signal in the vicinity of the volcanic arc is not related to the interseismic deformation, we masked the signal in this region. After downsampling the total number of pixels is 988.

1-2.5 Error analysis

To assess uncertainties of model parameters, it is useful to characterize the noise level in the data. One of the main sources of spatially correlated noise in InSAR data comes from residual atmospheric signal [e.g., *Hanssen*, 2001; *Lohman and Simons*, 2005; *Liu et al.*, 2014]. To estimate the contribution of this spatially correlated noise in the linear rate map we adopted a sample covariogram approach in which the atmospheric errors can be approximated as spatially stationary and isotropic. The definition of the sample covariogram is

$$\hat{C}(h) = \frac{1}{2N} \sum_{\substack{i=1 \\ \|r_i - s_i\| \approx h_c}}^{N} d(r_i) \cdot d(s_i) \, ;$$

where N is the number of pixel pairs at location r_i and s_i which satisfy $\|r_i\text{-}s_i\|=h$, h is the distance between pixel pairs, and $d(r_i)$ is the observation at pixel r_i [*Hanssen*, 2001; *Lohman and Simons*, 2005]. We masked the signal at the southern end of the peninsula and near the volcanic arc to assure that no deformation signal is included in the atmospheric noise estimation (Figure 1-5a). The sample covariogram is calculated by averaging the covariance of each pixel pair within 10 m intervals in the distance range from 0 to 50 km. We used an empirical covariance function $\hat{C}(h)=\sigma^{2}e^{-x/L}$ [*Hanssen*, 2001] to fit the calculated sample covariogram. For the linear rate map, the estimated σ^2 is 6.5 mm^2 and L is 35.2 km (Figure 1-5b). To construct the covariance matrix of the quadtree sampled linear rate map, we propagated the covariance of each pair, which was calculated by the estimated covariance function, into the corresponding quadtree square [*Sudhaus and Sigurjón*, 2009]. This covariance matrix was used in the InSAR/GPS joint inversion for interseismic coupling.

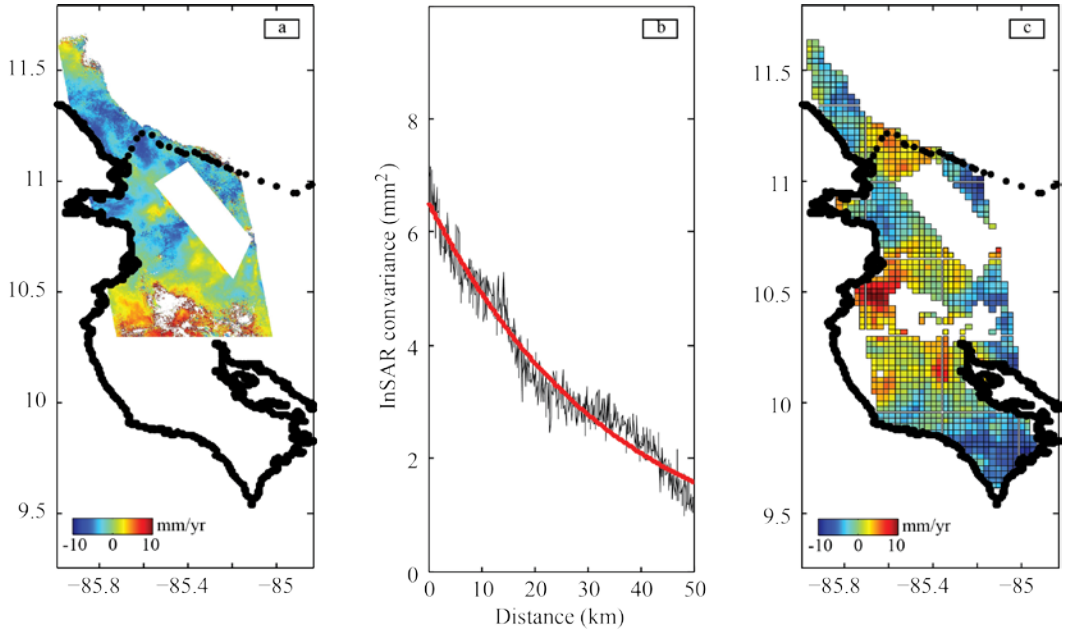

Figure 1-5. (a) The masked linear rate velocity map used for atmosphere noise estimation. (b) 1-D covariance from the masked linear rate velocity map shown in (a). The black line is the estimated covariogram, and the red line is the best fit of covariance function. (c) Quadtree sampled synthetic atmospheric noise by using covariance function.

In order to assess the effects of this spatially correlated noise in the inversion, we generated a synthetic atmospheric signal (Figure 1-5c) by using the estimated covariance matrix of the quadtree sampled linear rate map [*Parsons et al.*, 2006]. The simulated synthetic atmospheric noise has similar characteristics to the noise in the linear rate map, so it presents a good approximation for the residual atmospheric noise in the data. This synthetic atmospheric signal was used in the checkerboard test to include the influence of the spatial correlated noise.

1-3 GPS data

The continuous and campaign GPS interseismic velocities used in our model are taken from *Feng et al.*, [2012]. There are 19 continuous GPS stations (installation initiated in 2002 and completed in late 2009 [*Outerbridge et al.*, 2010]) and 29 campaign stations (which were occupied at least twice for three consecutive days each time) [*Feng et al.*, 2012]. These GPS data have different observation periods, but most of them overlap the temporal coverage of the InSAR data. The GPS network covers the entire Nicoya Peninsula (Figure 1-6a). To better constrain the downdip limit of the seismogenic zone, we included high quality GPS vertical velocities. All GPS velocities are relative to the stable Caribbean plate [*Feng et al.*, 2012].

1-4 Modeling

1-4.1 Modeling method

We used a back-slip model to invert for the slip deficit on the plate interface [*Savage*, 1983], assuming the interseismic strain accumulation is elastic. The back-slip approximates the coupling on the plate interface. Regions where the back-slip is the same as the plate motion rate are considered to be fully coupled [e.g. *Hetland and Simons*, 2010; *Liu et al.*, 2010a; *Savage*, 1983; *Wang and Dixon*, 2004].

The plate interface geometry is adopted from the model of *Feng et al* [2012], which was derived from the slab seismicity [*Ghosh et al.*, 2008]. The plate dip angle changes from the surface to a depth of 62 km. From the trench to a depth of 18.6 km, the dip angle has a constant value of 11.4°. Below the depth of 18.6 km, a parabolic function is fit to the dip angle change, which has a maximum dip angle of 48.1° at a depth of 62 km (Figure 1-6b). The total interface has a length of 200 km along the trench strike direction, and a width of 145 km along the dip direction. It is discretized into 40×29 rectangular patches with a patch size of 5 km ×5.1 km (Figure 1-6a).

Since oblique convergence has been suggested to be accommodated mostly by forearc sliver motion rather than strike slip motion on the plate interface during the interseismic period [*Feng et al.*, 2012; *Norabuena et al.*, 2004], and the strike slip motion is negligible relative to the dip slip motion on the plate interface (see the Supplementary Material), we only consider the back slip component along the dip direction. We resolved the 3-D GPS velocities to trench-normal and vertical components, which provide good constraints on the downdip transition depth from locked to aseismic creeping. We excluded GPS stations near the volcanic arc due to

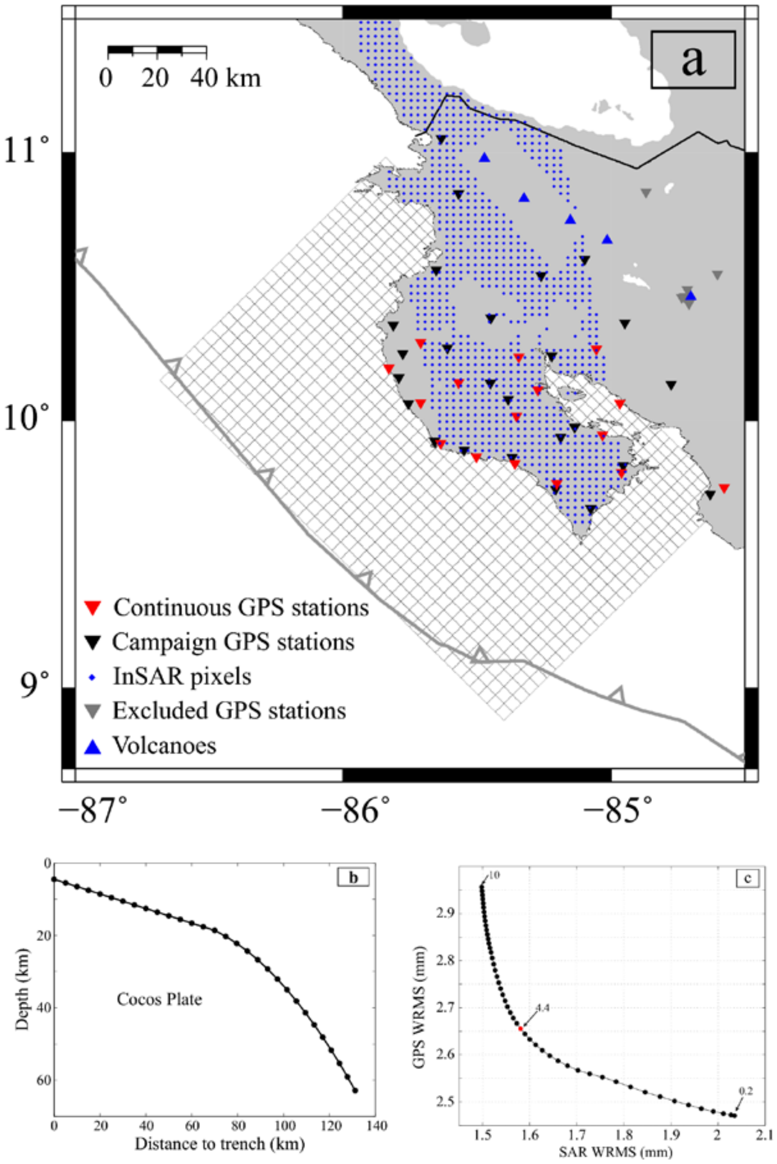

Figure 1-6. Fault model parameterization. (a) Surface projection of the fault plane model with grid spacing of 5 km along strike and dip direction respectively. The red inverse triangles indicate the location of the continuous GPS stations, and the black inverse triangles indicate the location of the campaign GPS stations. The blue diamonds indicate the location of the InSAR pixels. The gray triangles indicate the location of the excluded GPS stations. The blue triangles are the Holocene active volcanoes [*Siebert and Simkin*, 2002]. (b) Cross section of the plate interface used in our model. The black nodes denote the ends of the planar row segments. (c) Trade-off curve between the weighted root mean square (WRMS) errors of both InSAR and the GPS. The preferred weight number is 4.2 which can fit both InSAR and GPS well.

possible contamination from volcanic deformation (Figure 1-6a). The linear inverse problem is

$$\begin{bmatrix} aW_{sar}G_{sar} & I \\ W_{gps}G_{gps} & 0 \\ \gamma D & 0 \end{bmatrix}\begin{bmatrix} U \\ C \end{bmatrix} = \begin{bmatrix} aW_{sar}d_{sar} \\ W_{gps}d_{gps} \\ 0 \end{bmatrix}$$

where U is a $M \times 1$ slip vector along the fault dip direction, M is the number of fault patches, C is the nuisance offset between GPS and InSAR, a is the relative weighting ratio between InSAR and GPS, W_{sar} is a weighting matrix for the InSAR data set, which satisfies $W_{sar}^T * W_{sar} = \sum_{sar}^{-1}$, $\sum_{sar}$ is the InSAR data covariance matrix, G_{sar} is the $N \times M$ Green function matrix with the elastic response at each InSAR pixel for unit dip slip at each fault patch, N is the number of InSAR pixels, I is a $N \times 1$ vector whose elements are all one, d_{sar} is a $N \times 1$ displacement vector at each InSAR pixel, W_{gps} is a weighting matrix for the GPS data set, which satisfies $W_{gps}^T * W_{gps} = \Sigma_{gps}^{-1}$, $\sum_{gps}$ is the GPS data covariance matrix, G_{gps} is a $3N_2 \times M$ Green function matrix which is the elastic response in the north, east, and vertical directions at each GPS station for unit dip slip at each fault patch, N_2 is the number of GPS stations, d_{gps} is a $3N_2 \times 1$ displacement vector including the east, north, and up components. $D = \nabla^2$ is a $M \times M$ Laplace smoothing matrix that is a scale-dependent second order finite difference operator along both dip and strike directions, and γ is the smoothing factor. All the Green functions are calculated using an elastic dislocation model in a half space [*Okada*, 1985]. The covariance matrix of the GPS Σ_{gps} is

$diag\{\sigma_{1e}^2, \sigma_{1n}^2, \sigma_{1u}^2, ..., \sigma_{ie}^2, \sigma_{in}^2, \sigma_{iu}^2\}$, where $\sigma_{ie}^2, \sigma_{in}^2, \sigma_{iu}^2$ is the standard deviation of the east, north, and vertical components of the *ith* GPS. The GPS error estimation accounts for both the time-uncorrelated and time-correlated noises [*Feng et al.*, 2012]. The covariance matrix of InSAR is calculated based on the estimated covariance function in section 2.5.

We investigate the effect of the different weighting factors between InSAR and GPS on the inversion by varying this parameter from 0.1 to 10. The higher weighting of InSAR provides a better fit to the InSAR but a worse fit to the GPS data. We find a weight of 4.2:1 between InSAR and GPS provides a good balance between fitting both the InSAR and GPS data (Figure 1-6c).

Our model is solved by using a least squares constrained inversion. The back slip rate at each fault element is constrained between zero and the trench-normal convergence rate between the Cocos and Caribbean plates (Co-CA). We impose a zero slip constraint at the trench and free slip at all other fault boundaries. Imposing zero slip constraints on all the fault boundaries does not change the inversion results. The smoothing factor γ is determined by the trade-off between model roughness and weighted data misfit (Figure 1-7d). Larger smoothing factors reduce the roughness of the model, but increase data misfit [*Feng et al.*, 2012; *Jónsson et al.*, 2002; *Liu et al.*, 2010a]. The weighted root mean square (WRMS) residual is used for the model misfit. We choose λ=1 as the preferred smoothing factor, which provides a balance between the roughness and WRMS residual (Figure 1-7d). This preferred model fits both the InSAR and GPS data well (Figure 1-8).

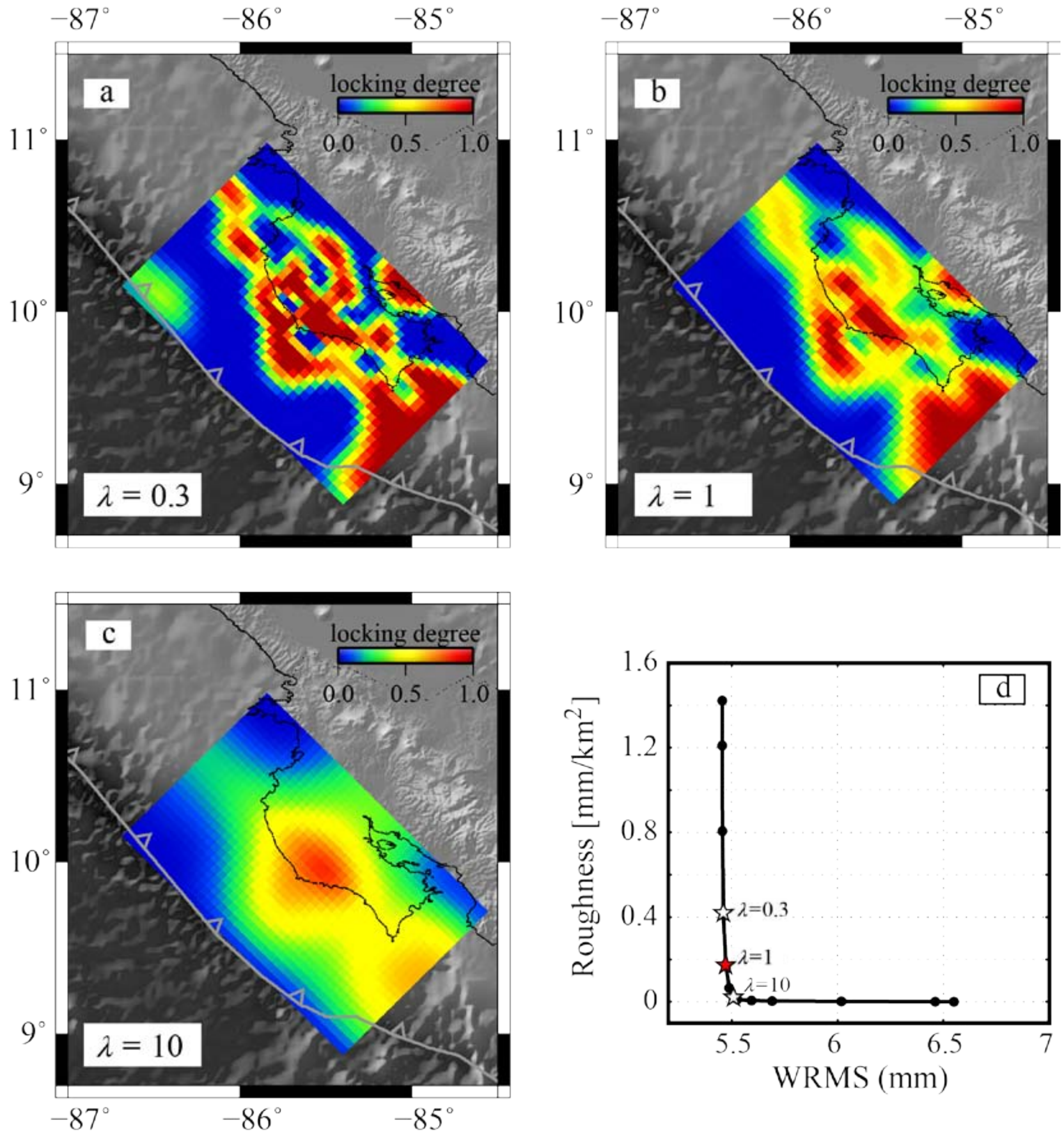

Figure 1-7. Surface projection of interseismic locking pattern for selected smoothing factors λ: (a) λ=0.3 , (b) λ=1 , (c) λ=10. (d) Trade-off curve between model roughness and the weighted root mean square (WRMS) residual of the model fit. Our preferred smoothing factor λ=1 provides a balance between the roughness and the model misfit. The dataset includes both GPS and InSAR data, and a weighting factor between GPS and InSAR of 1:4.2 for all the models with different smoothing factors.

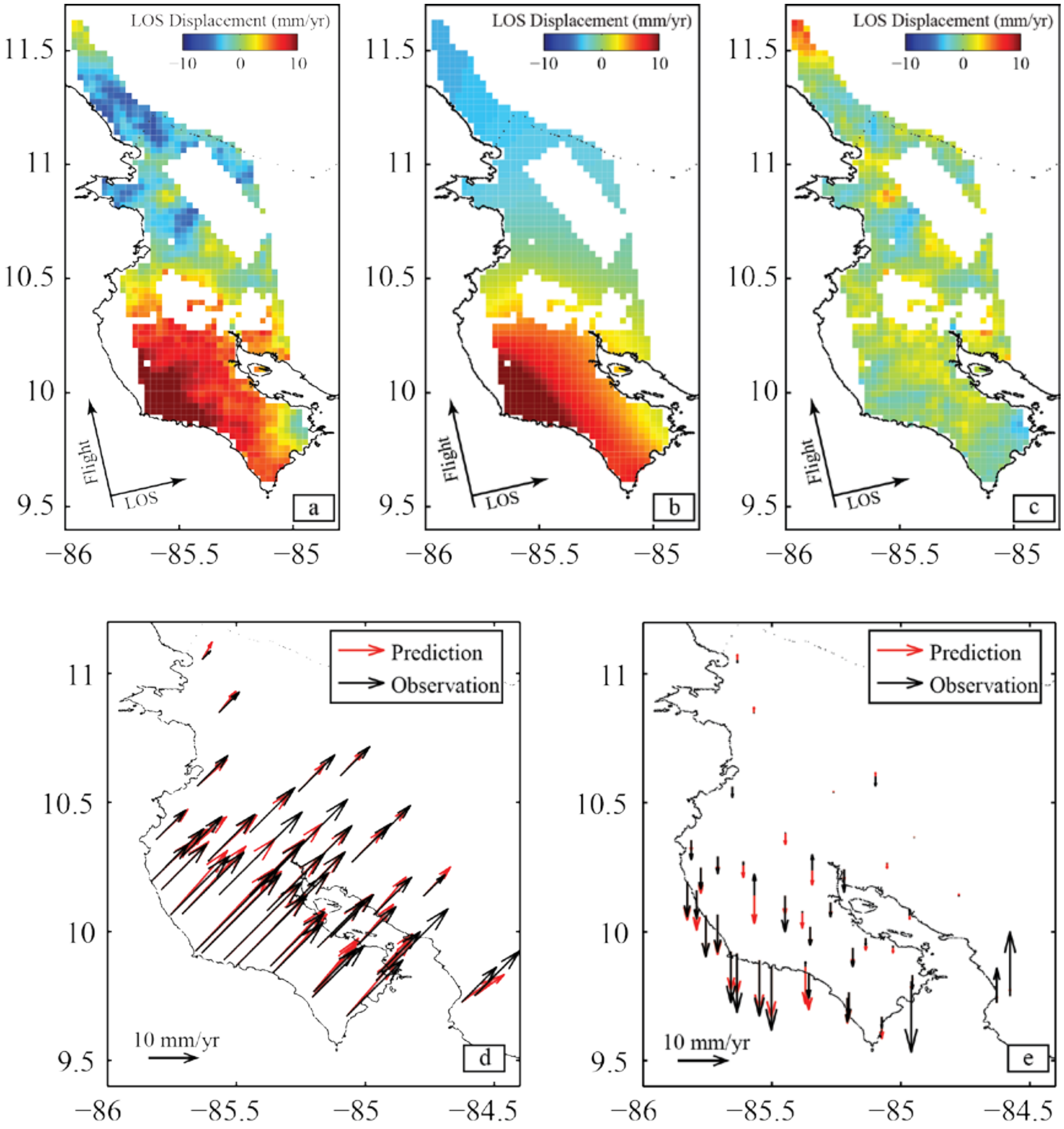

Figure 1-8. Misfit of the preferred back slip model to the observed data (a) Quadtree sampled InSAR linear rate velocity. (b) Predicted surface displacement in LOS direction from the preferred model. (c) LOS residual. (d) Predicted GPS horizontal velocity (red) versus the observed GPS horizontal velocity (black). (e) Predicted GPS vertical velocity (red) versus the observed GPS vertical velocity (black).

1-4.2 Checkerboard resolution test

To examine the spatial resolution in our model, we performed a checkerboard test. Since the average length scale of the coupling pattern in the resulting model is ~ 40×40 km^2, we divided the fault surface into patches of this size and imposed alternating full and zero back slip as the synthetic input model (Figure 1-9a). We then calculated the surface displacement at the GPS stations and the LOS displacement at each SAR pixel. We added random noise to the synthetic GPS velocities. The random noise follows a normal distribution with zero mean and the same uncertainty as the observed GPS data. We also added synthetic atmospheric noise (Figure 1-5c) to the synthetic InSAR data to assess the effect of spatially coherent noise on the inversion. The covariance matrixes of GPS and InSAR used in the checkerboard tests are the same as used in the modeling. The same inversion method was applied to the checkerboard test and the results using different smoothing factors are shown in Figures 1-9b-d. All the tests show that the region under the Nicoya Peninsula is well resolved with little resolution near the trench and reduced resolution downdip on the fault interface. After testing the effect of different smoothing factors on the resolution, we find a factor of 1 provides the best spatially recovered pattern.

1-4.3 Modeling Results

Our preferred model shows three robust strongly coupled regions (Figure 1-10). One patch locates beneath the middle portion of the Nicoya Peninsula centered at ~ 22 km depth. This locked region is very consistent for different smoothing factors (Figure 1-

7), and also coincides well with the rupture area of the 2012 M_W 7.6 Nicoya, Costa

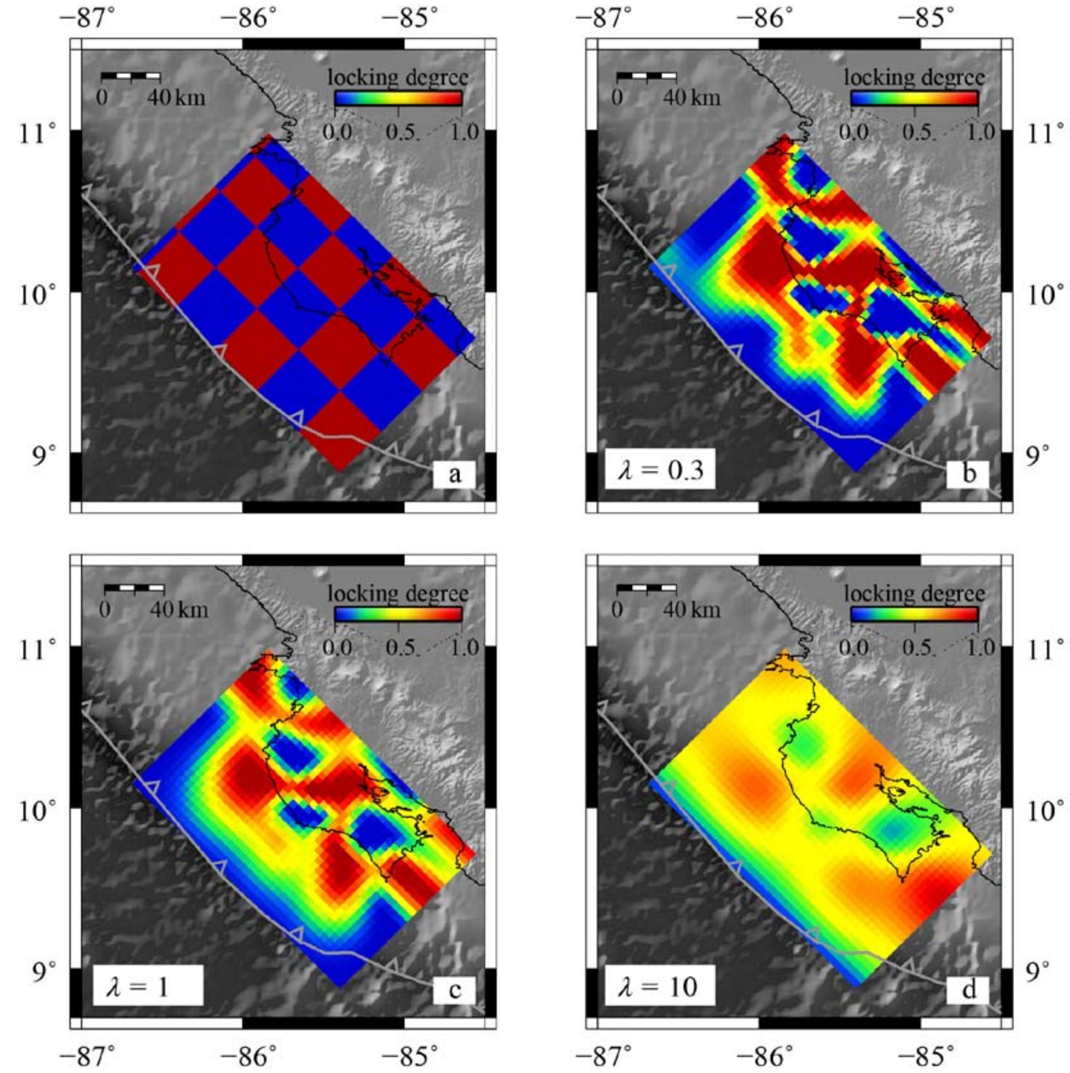

Figure 1-9. Checkerboard test showing the spatial resolution of the joint inversion of GPS and InSAR. (a) the imposed locking pattern, (b) recovered locking pattern at λ=0.3 using the same inversion method and data distribution as in the real data set, (c) recovered locking pattern at λ=1 which is our preferred smooth factor, (d) recovered locking pattern at λ=10. The weighting factor between GPS and InSAR is 1:4.2.

Rica Earthquake. The second locked patch locates just offshore the central Peninsula, centered at ~14 km depth and is nearly parallel to the first patch. This feature persists even when a larger smoothing factor is used. This region experienced little slip during the 2012 Nicoya, Costa Rica Earthquake. The third strongly locked patch locates offshore the southeastern end of the Nicoya Peninsula, and the coupling pattern close to the coastline is a robust feature and appears in results using different smoothing factors. This area also overlaps part of the rupture area of the 1990 M_W 7.0 Gulf of Nicoya earthquake (see Figure 1-11). The model indicates another strongly coupled region at the downdip edge of the fault; however, because it occurs in an area of low resolution due to a data gap and high noise near the inlet to the Nicoya Gulf, we do not believe that it is reliable. The accumulated geodetic strain moment rate of the first strongly coupled patch (a ~1100 km^2 area defined by the 70% locking contour) is equivalent to ~2.2×10^{18} Nm/yr (assuming a rigidity of 30 GPa). If this rate is assumed to be constant, the accumulated strain between 1950 and 2012 corresponds to a M_W 7.3 (~1.3×10^{20} Nm) earthquake. The accumulated moment rate of the central offshore locked patch is ~1.4×10^{18} Nm/yr (fault area of ~765 km^2), corresponding to a M_W 7.2 earthquake over this same 62 year period.

Our model also indicates several regions with partial coupling (~55% locking, Figure 1-10): two patches downdip of the onshore strongly coupled region and one patch offshore of the northwestern part of the Nicoya Peninsula. The two downdip partially coupled regions are directly beneath land with excellent data coverage, so they are robustly resolved. The partially coupled area offshore to the northwest is also well resolved near the coastline, based on the resolution tests (Figure 1-9c).

The updip limit of our preferred coupling model is at ~10 km depth, which is shallower than the upper limit of microearthquakes in this region [*Newman et al.*, 2002], and the depth of the 100 °C isotherm [*Harris et al.*, 2010] although admittedly this updip limit is not well constrained because of a lack of data offshore. The downdip limit of coupling does not appear as an abrupt transition (Figure 1-10). The depth of the deepest strong coupling (<70%) is ~24 km, while 55% coupling persists to almost 40 km depth.

1-5 Discussion

1-5.1 Interseismic strain accumulation

Slow slip, like earthquake motion occurs in the opposite direction of interseismic locking on the plate interface and releases part of the accumulated strain [e.g., *Liu et al.*, 2010b, *Beroza and Ide* 2011]. The long term accumulated elastic strain therefore includes the effect of any SSEs [e.g., *Correa-Mora et al.*, 2008; *Outerbridge et al.*, 2010]. Both GPS and InSAR data reflect the long-term strain accumulation averaged over several SSEs. The GPS data set we utilized is the velocity averaged over many years and includes transient offsets due to several SSEs [*Feng et al.*, 2012]. The InSAR linear rate map is also an average velocity over four years that includes the occurrences of several SSEs. Therefore, our resulting coupling model investigates the average “interseismic” strain accumulation rather than “inter-transient” strain accumulation.

1-5.2 Comparison to the GPS-only coupling model

Our preferred GPS/InSAR integrated model is similar to the GPS-only model in its long wavelength features, but differs from it in detail. Although both models contain two strongly coupled patches, one beneath and the other offshore the central part of the Peninsula, the two strongly coupled patches have slightly different spatial patterns in the two models (Figure 1-10). The onshore locked patch in the GPS-only model extends to greater depth and is indented or notched compared with the integrated model. The central offshore locked patch in the two models has a similar depth, but clear variations along strike. The GPS-only model shows moderate coupling south of the boundary between Cocos-Nazca spreading center and East Pacific Rise (CNS-EPR) derived crust, while the integrated model indicates strong coupling south of this boundary (Figure 1-10). The two strongly locked patches in the integrated model also have more separation along dip and more elongation along strike. The high resolution of these two strongly locked patches (Figure 1-9) and their robustness (see supplementary material section 6) suggests these differences between the InSAR/GPS integrated and the GPS only models are statistically significant. The third strongly locked region just offshore the southeastern portion of the Peninsula is more prominent in the integrated model than in the GPS-only model. This region is near the edge of our grid and a portion has poor resolution (Figure 1-9), so we have less confidence in the difference between the models in this area.

In contrast to these somewhat subtle differences in the strongly coupled regions, the two models are significantly different in the distribution of partially coupled regions and the transition from strong to weak coupling. For example, our integrated model reveals two onshore partially coupled areas with ~55% locking downdip of the strongly locked patch (Figure 1-10), while the GPS-derived model reveals very low coupling (0-30% coupling) in these two areas [*Feng et al,* 2012]. This difference between models beneath the land reflects a better resolution of the combined InSAR and GPS data set (see supplementary section 7). Moreover, an elongated ~55% locked patch exists in the northwestern offshore region in the integrated model while this partially coupled feature appears stronger and extends further inland in the GPS only model. Similarly, a downdip ~55% coupled region in the GPS only model appears to be uncoupled in our integrated model (northwestern most part of the peninsula in Figure 1-10). Another downdip ~55% coupled region to the southeast is not well resolved in either model. The integrated model images an abrupt updip transition from strong to zero coupling about half way between the shoreline and the trench while the GPS derived model shows a much smoother transition. In general, we find that the integrated and GPS only models share similar long wavelength characteristics, but inclusion of InSAR data improves model resolution and reveals more refined features at the local scale.

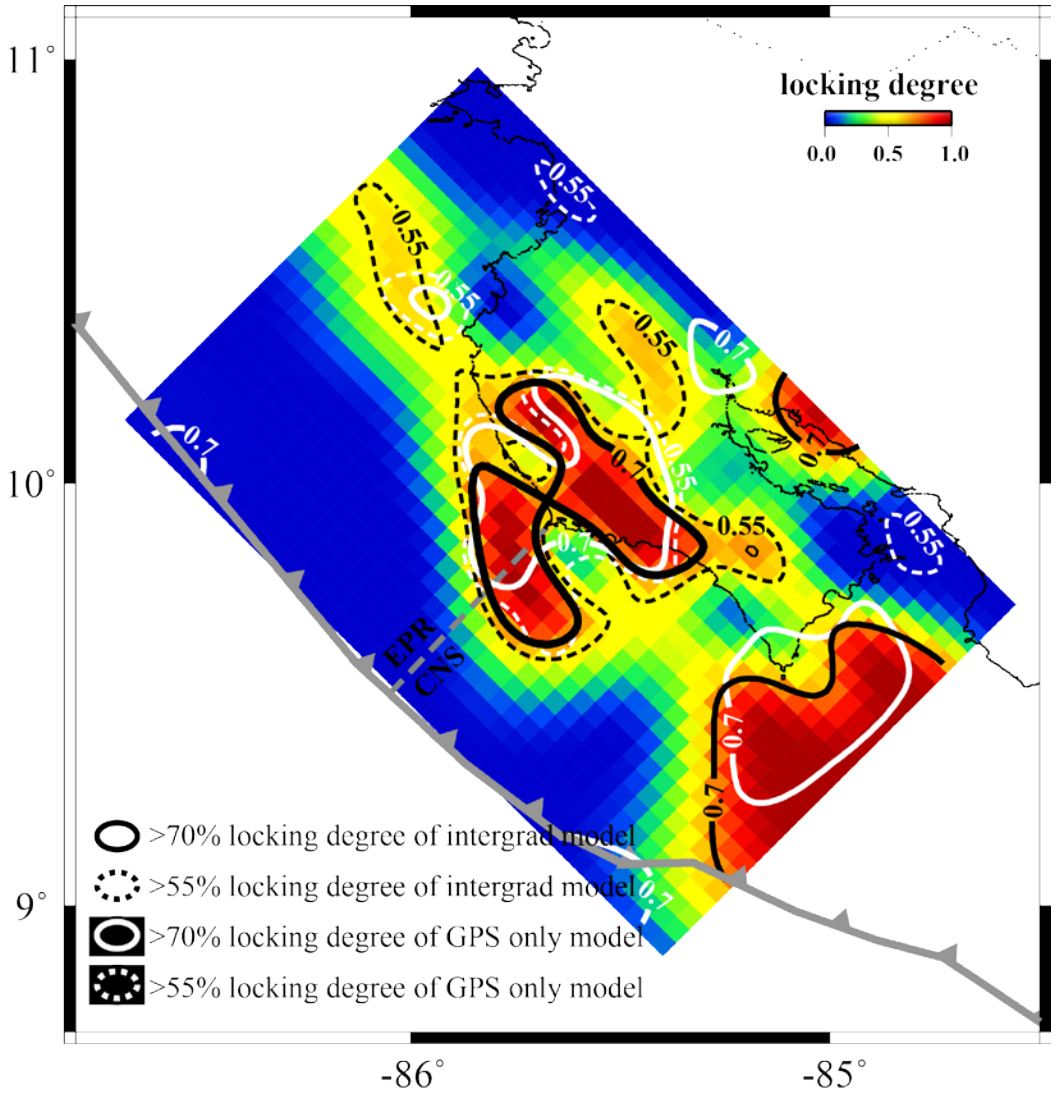

Figure 1-10. Comparison between the integrated interseismic coupling model and the GPS only model. The regions of our model with coupling degree > 70% are outlined by solid black lines, and the regions with coupling degree >55% are outlined by dashed black lines. The regions of *Feng et al.*, [2012] with coupling degree > 70% are outlined in solid white lines, and the regions with coupling degree > 55% are outlined by white dashed lines

1-5.3 Comparison with local seismic and aseismic events

The 5 September 2012 M_W 7.6 Nicoya earthquake nucleated offshore and ruptured down dip with the largest slip occurring coincident with the onshore strongly coupled patch as anticipated [*Protti et al.*, 2014; *Yue et al.*, 2013], while most of the central offshore strongly coupled patch remained intact. The 2012 coseismic rupture extended into the transition region from strong to weak coupling (Figure 1-11), which suggests dynamic rupture is capable of penetrating into regions with conditional stability. Most thrust aftershocks of the 2012 event occurred near the upper edge of the onshore strongly coupled patch that failed in the earthquake (Figure 1-11). Few of these aftershocks and any previously identified plate boundary events [*DeShon et al.*, 2006] locate in the central offshore strongly coupled patch. The lack of coseismic and interseismic slip on this patch suggests a different mechanical behavior from the onshore locked patch. The fate of the central offshore locked patch and its mode of future failure are unclear. It may have the potential to generate a future large earthquake (Mw 7.2 as estimated in section 4.3). However, the occurrence of afterslip (R. Malservisi, personal comm., 2014), its proximity to geodetically determined slow slip [*Dixon et al.*, 2014] and accompanying tremor and very low frequency earthquakes (see Supplementary Material) suggests that this region may have released some of the accumulated strain. A recent inversion of the GPS data using a refined 3-D plate interface model for the Nicoya Peninsula produced a muted offshore locking pattern [*Kyriakopoulos and Newman*, 2013]. The significantly reduced offshore strain accumulation of their model may in part be released during aseismic transient events. The third strongly locked region offshore the southeast part of the Peninsula that overlaps the rupture area of the 1990 M_W 7.0 earthquake did not slip during the 2012

Nicoya earthquake and we believe it has the potential to fail in another future earthquake.

Large slow slip events (SSEs) have occurred repeatedly on the plate interface near Nicoya every 21±6 months, while smaller events are much more frequent [*Jiang et al.*, 2012; *Dixon et al.*,2014]. All of the SSEs are accompanied by tremor with both low frequency (LFE) and very low frequency (VLFE) earthquakes embedded within this tremor [*Brown et al.*, 2009*; Walter et al.*, 2013]. There were 7 SSEs recorded by GPS stations between 2007-2012, and all had some slip both updip and downdip of the seismogenic zone [*Outerbridge et al.*, 2010; *Dixon et al.*,2014]. A comparison of slow slip locations with the coupling pattern of our model shows that downdip slow slip mainly occurs in the weakly coupled regions (locking <55%) while updip slow slip overlaps part of the strongly locked areas (Figure 1-11). A more detailed interpretation of the relative locations of these features should consider the different fault geometries used in the inversion schemes.

The abundant tremor and very low frequency earthquakes that accompany slow slip are poorly located, but corroborate the overlap of slow slip phenomena with the offshore locked patch (Supplementary Material). If shallow slow slip indeed overlaps part of the strongly coupled region, it suggests that strain accumulation may be in part released by the recurrent SSEs in the shallow seismogenic zone in Costa Rica, similar to what has been found in other subduction zones [e.g., *Liu et al*., 2010b; *Beroza and Ide*, 2011]. The overlap of stick-slip and slow slip behavior may be real or more likely

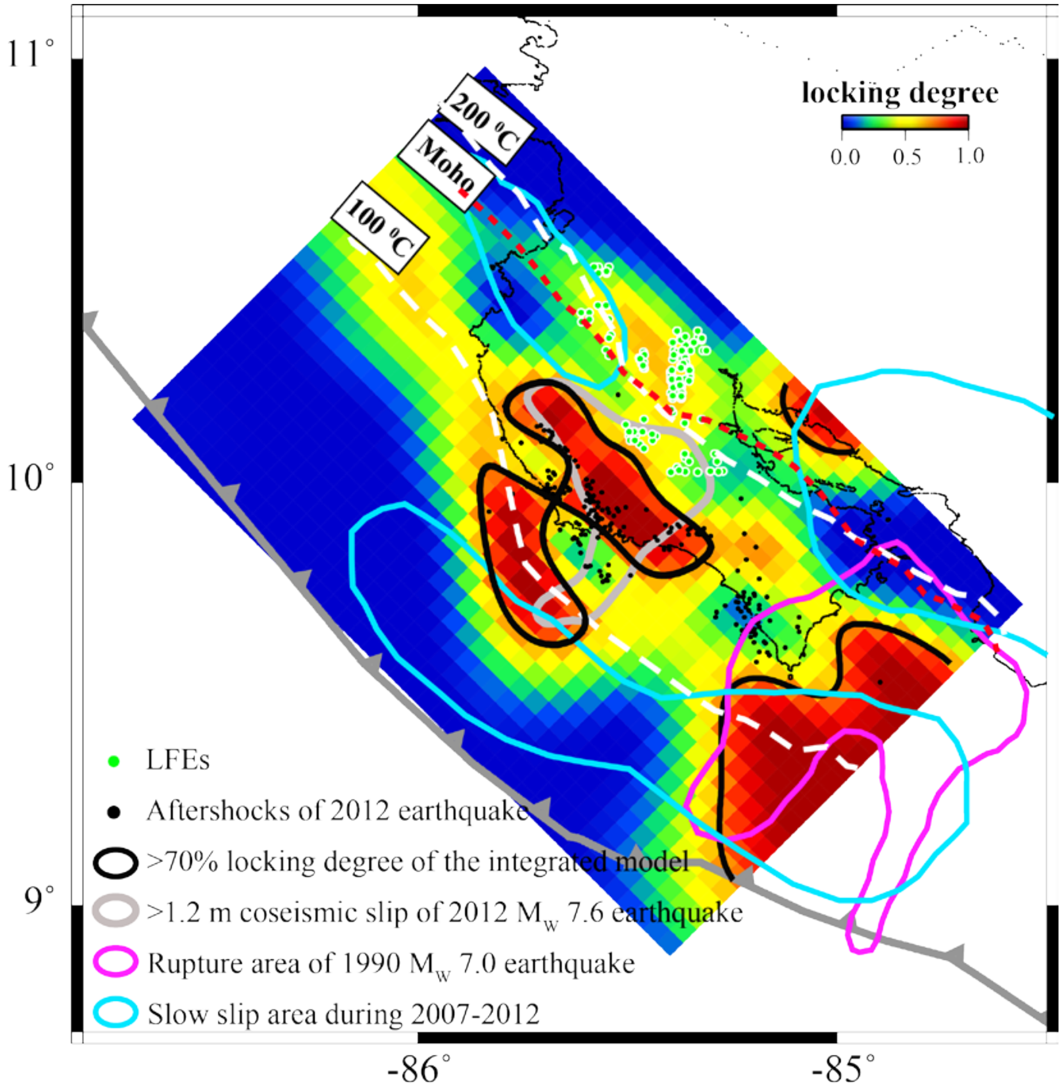

Figure 1-11. Comparison between the integrated interseismic coupling model and local seismic and aseismic events. The regions of our model with coupling degree > 70% are outlined in solid black lines. The region of coseismic slip >1.2 m is outlined in gray color. The coseismic rupture zone of 1990 M_W 7.0 earthquake is outlined in pink color. The sum of the slow slip during 2007-2012 is outlined in the light blue color [*Dixon, et al.*, 2014]. Low-frequency earthquakes (LFE) [*Brown et al.*, 2009] are plotted with green-filled, white-bordered circles. Thrust aftershocks of the 2012 event are indicated with black dots. The 110°C and 200°C isotherms are indicated as the white dashed lines [*Harris, et al.*, 2010], and the Moho is indicated as the red dashed line.

reflects our inability to distinguish small length scale variations in frictional behavior due to limited resolution. Closely located brittle and viscous deformation modes have been shown to exist in rock assemblages from exhumed subduction zones [*Fagereng and Sibson*, 2010]. These authors proposed that subduction plate boundary shear zones are very heterogeneous and may consist of alternating weak and strong components that can host seismic and aseismic deformation modes within a small volume.

Brown at al., [2009] located deep low frequency earthquakes (LFEs) in Costa Rica using a network autocorrelation approach, which allows individual S waves to be identified. These LFEs are the most accurately located slow slip phenomena in the region and occur over a depth range of 30-40 km on the plate interface. They mainly occur in the partially locked (~55%) areas at the transition from strong to weak coupling just downdip of the strongly locked patch (Figure 1-11). LFEs and partial coupling indicate the transition in frictional properties from stick-slip to stable sliding.

Integration of our coupling model with the local seismic/aseismic events provides some insights into possible mechanisms producing variations in locking behavior of the Nicoya, Costa Rica subduction interface. The fact that the 100^{o}C isotherm intersects the central offshore strongly coupled region, and the 200^{o}C isotherm occurs deeper than the dowdip limit of locking suggests that temperature is not the primary control on coupling variations in Nicoya, Costa Rica. Similar conclusions were also drawn for the Hikirangi subduction zone, New Zealand and the Cascadia subduction zone [*MaCaffrey et al.*, 2008, *Gomberg*, 2010]. Numerical models show that SSEs typically occur at transitions from velocity weakening to velocity strengthening [e.g., *Liu and Rice*, 2005a; *Liu and Rice*, 2007]. The coincidence of SSEs with low coupling in our model suggests that differences in frictional properties are an important factor affecting coupling variations. The occurrence of LFEs, and slow slip in general, has been attributed to fluid-rich environments with high pore pressure [*Schwartz and Rokosky*, 2007; *Shelly*, 2010]. Previous studies in Costa Rica indicate that the fluid production is very high at both shallow and deep depths along the subducting plate interface beneath Nicoya Peninsula [e.g. *Tryon et al.*, 2010; *Hensen et al.*, 2004, *Audet and Schwartz*, 2013]. Dehydration of clay minerals in the subducted marine sediments at shallow depth and serpentinization at deep depth could provide sources for such high fluid production [*Tryon et al.*, 2010; *Hensen et al.*, 2004; *DeShon and Schwartz*, 2004]. In this regard, fluid distribution at the plate interface may be another important factor contributing to the observed coupling variations in the Costa Rica subduction zone.

1-6 Conclusions

The interseismic InSAR linear rate map for the Nicoya Peninsula reveals a LOS deformation rate on the southern coastline of ~10-15 mm/yr that gradually decreases inland from the trench. Our study demonstrates that InSAR data can be used to recover small, long wavelength deformation signals in challenging subduction zone environments when integrated with GPS observations. The interseismic coupling model using both GPS and InSAR data reveals three robust strongly coupled regions:

1) beneath the middle portion of the Nicoya Peninsula centered at ~ 22 km depth; 2) offshore the central part of the peninsula, parallel to the first patch; and 3) offshore the southeast end of the peninsula. The first patch ruptured during the 2012 *M*w 7.6 Costa Rica earthquake as expected. The second patch did not and its mode of future failure is unclear. It might have the potential for a future seismic event of ~M_W 7.2, or much of its accumulated strain may be released by slow slip. The third strongly coupled patch overlaps part of the rupture area of the Gulf of Nicoya 1990 *M*w 7.0 earthquake and will likely slip again in a future earthquake.

Our integrated model and the GPS-only model share similar long wavelength characteristics, but inclusion of InSAR data improves model resolution and reveals more refined features at local scales. This allows for improved comparison with local seismic and aseismic events. Well-located low frequency earthquakes that accompany slow slip, occur at downdip transitions from strong to weak coupling. Geodetically detected deep slow slip tends to occur in weakly coupled regions while updip slow slip may overlap with strongly locked areas and help to release part of the accumulated strain. The spatial correlation between the distribution of coupling and the locations of SSEs and LFEs suggests that fluid and frictional heterogeneities may be the two main factors influencing coupling variations.

1-7 Acknowledgements

This study was supported by OCE-0841061 and EAR-1321550. ALOS PALSAR data is copyright JAXA/METI and was provided by the GEO Supersites and the US Government Research Consortium Data pool at the Alaska Satellite Facility (https://www.asf.alaska.edu/). The research described in this paper was carried out in part at the Jet Propulsion Laboratory, California Institute of Technology, under a contract with the National Aeronautics and Space Administration. We greatly appreciate the support of Prof. Emily Brodsky, and thank all the people who provided advice on this project. Figures were created using Generic Mapping Tools [*Wessel and Smith*, 1991].

1-8 References

Audet, P., and S. Y. Schwartz (2013), Hydrologic control of forearc strength and seismicity in the Costa Rican subduction zone, *Nature Geoscience*, *6*(10), 852-855.

Bejar-Pizarro, M., A. Socquet, R. Armijo, D. Carrizo, J. Genrich, and M. Simons (2013), Andean structural control on interseismic coupling in the North Chile subduction zone, Nature Geosci, 6(6), 462-467.

Berardino, P., G. Fornaro, R. Lanari, and E. Sansosti (2002), A new algorithm for surface deformation monitoring based on small baseline differential SAR interferograms, *Geoscience and Remote Sensing, IEEE Transactions on*, *40*(11), 2375-2383.

Beroza, G. C., and S. Ide (2011), Slow earthquakes and nonvolcanic tremor, *Annual Review of Earth and Planetary Sciences, 39,* 271-296.

Biggs, J., D. P. Robinson, and T. H. Dixon (2009), The 2007 Pisco, Peru, earthquake (M8.0): seismology and geodesy, *Geophysical Journal International*, *176*(3), 657-669.

Biggs, J., T. Wright, Z. Lu, and B. Parsons (2007), Multi-interferogram method for measuring interseismic deformation: Denali fault, Alaska, *Geophysical Journal International*, *170*(3), 1165-1179.

Brown, J. R., G. C. Beroza, S. Ide, K. Ohta, D. R. Shelly, S. Y. Schwartz, W. Rabbel, M. Thorwart, and H. Kao (2009), Deep low-frequency earthquakes in tremor localize to the plate interface in multiple subduction zones, *Geophysical research letters*, *36*(19), L19306.

Bürgmann, R., P. A. Rosen, and E. J. Fielding (2000), Synthetic aperture radar interferometry to measure Earth's surface topography and its deformation, *Annual Review of Earth and Planetary Sciences*, *28*(1), 169-209.

Cavalié, O., C. Lasserre, M. P. Doin, G. Peltzer, J. Sun, X. Xu, and Z. K. Shen (2008), Measurement of interseismic strain across the Haiyuan fault (Gansu, China), by InSAR, *Earth and planetary science letters*, *275*(3-4), 246-257.

Cavalié, O., E. Pathier, M. Radiguet, M. Vergnolle, N. Cotte, A. Walpersdorf, V. Kostoglodov, and F. Cotton (2013), Slow slip event in the Mexican subduction zone: Evidence of shallower slip in the Guerrero seismic gap for the 2006 event revealed by the joint inversion of InSAR and GPS data, Earth and planetary science letters, 367(0), 52-60.

Chen, C. W., and H. A. Zebker (2000), Network approaches to two-dimensional phase unwrapping: intractability and two new algorithms, *JOSA A*, *17*(3), 401-414.

Correa-Mora, F., C. DeMets, E. Cabral-Cano, B. Marquez-Azua, and O. Diaz-Molina (2008), Interplate coupling and transient slip along the subduction interface beneath Oaxaca, Mexico, *Geophysical Journal International*, *175*(1), 269-290.

DeMets, C., R. G. Gordon, and D. F. Argus (2010), Geologically current plate motions, *Geophysical Journal International*, *181*(1), 1-80.

DeShon, H. R., and S. Y. Schwartz (2004), Evidence for serpentinization of the forearc mantle wedge along the Nicoya Peninsula, Costa Rica, *Geophysical research letters*, *31*(21), L21611.

Dixon, T. H. (1993), GPS measurement of relative motion of the Cocos and Caribbean Plates and strain accumulation across the Middle America Trench, Geophysical research letters, 20(20), 2167-2170.

Dixon, T. H., Y. Jiang, R. Malservisi, R. McCaffrey, N. Voss, M. Protti, and V. Gonzalez (2014), Earthquake and tsunami forecasts: Relation of slow slip events to subsequent earthquake rupture, *Proceedings of the National Academy of Sciences, 111*(48), 17039-17044.

Fagereng, Å., and R. H. Sibson (2010), Melange rheology and seismic style, Geology, 38(8), 751-754. Gomberg, J. (2010), Slow-slip phenomena in Cascadia from 2007 and beyond: A review, Geological Society of America Bulletin, 122(7-8), 963-978.

Fattahi, H., and F. Amelung (2014), InSAR uncertainty due to orbital errors, Geophysical Journal International, 199(1), 549-560.

Feng, L., A. V. Newman, M. Protti, V. González, Y. Jiang, and T. H. Dixon (2012), Active deformation near the Nicoya Peninsula, northwestern Costa Rica, between 1996 and 2010: Interseismic megathrust coupling, *Journal of Geophysical Research: Solid Earth (1978–2012)*, *117*(B6).

Fialko, Y. (2006), Interseismic strain accumulation and the earthquake potential on the southern San Andreas fault system, *Nature, 441*(7096), 968-971.

Ghosh, A., A. V. Newman, A. M. Thomas, and G. T. Farmer (2008), Interface locking along the subduction megathrust from b-value mapping near Nicoya Peninsula, Costa Rica, *Geophysical research letters, 35*(1), L01301.

Gomberg, J. (2010), Slow-slip phenomena in Cascadia from 2007 and beyond: A review, *Geological Society of America Bulletin*, *122*(7-8), 963-978.

Gourmelen, N., F. Amelung, and R. Lanari (2010), Interferometric synthetic aperture radar–GPS integration: Interseismic strain accumulation across the Hunter Mountain fault in the eastern California shear zone, *J. geophys. Res*, *115*.

Hanssen, R. F. (2001), *Radar interferometry: data interpretation and error analysis*, Kluwer Academic Pub.

Harris, R. N., G. Spinelli, C. R. Ranero, I. Grevemeyer, H. Villinger, and U. Barckhausen (2010), Thermal regime of the Costa Rican convergent margin: 2. Thermal models of the shallow Middle America subduction zone offshore Costa Rica, *Geochemistry, Geophysics, Geosystems*, *11*(12), Q12S29.

Hensen, C., K. Wallmann, M. Schmidt, C. R. Ranero, and E. Suess (2004), Fluid expulsion related to mud extrusion off Costa Rica—a window to the subducting slab, *Geology*, *32*(3), 201-204.

Hetland, E. A., and M. Simons (2010), Post-seismic and interseismic fault creep II: transient creep and interseismic stress shadows on megathrusts, *Geophysical Journal International*, *181*(1), 99-112.

Hooper, A., D. Bekaert, K. Spaans, and M. Arıkan (2012), Recent advances in SAR interferometry time series analysis for measuring crustal deformation, Tectonophysics, 514–517(0), 1-13.

Hyndman, R., K. Wang, and M. Yamano (1995), Thermal constraints on the seismogenic portion of the southwestern Japan subduction thrust, *Journal of Geophysical Research: Solid Earth (1978–2012)*, *100*(B8), 15373-15392.

Jiang, Y., S. Wdowinski, T. H. Dixon, M. Hackl, M. Protti, and V. Gonzalez (2012), Slow slip events in Costa Rica detected by continuous GPS observations, 2002–2011, *Geochemistry, Geophysics, Geosystems*, *13*(4), Q04006.

Jónsson, S., H. Zebker, P. Segall, and F. Amelung (2002), Fault slip distribution of the 1999 Mw 7.1 Hector Mine, California, earthquake, estimated from satellite radar and GPS measurements, *Bulletin of the Seismological Society of America*, *92*(4), 1377-1389.

Kyriakopoulos, C. A. V. Newman, R. Malservisi, T. H. Dixon, J. I. Walter, M. Protti, V. Gonzalez, Geodetic and Structural Constraints on Locking and Failure Around the 5 September 2012 Nicoya (Mw7.6), Costa Rica Earthquake, Abstract presented at the Fall AGU meeting, G31C-04, 2013.

Liu, Y., and J. R. Rice (2005), Aseismic slip transients emerge spontaneously in three-dimensional rate and state modeling of subduction earthquake sequences, *Journal of Geophysical Research: Solid Earth*, *110*(B8), B08307.

Liu, Y., and J. R. Rice (2007), Spontaneous and triggered aseismic deformation transients in a subduction fault model, *Journal of Geophysical Research: Solid Earth*, *112*(B9), B09404.

Liu, Z., D. Dong, and P. Lundgren (2011), Constraints on time-dependent volcanic source models at Long Valley Caldera from 1996 to 2009 using InSAR and geodetic measurements, *Geophysical Journal International*, *187*(3), 1283-1300.

Liu, Z., H. S. Jung, Z. Lu (2014), Joint correction of ionosphere noise and orbital error in L-band SAR interferometry of interseismic deformation in southern California, IEEE Transactions on Geosciences and Remote Sensing, 52(6), 3421-3427, doi: 10.1109/TGRS.2013.2272791

Liu, Z., S. Owen, D. Dong, P. Lundgren, F. Webb, E. Hetland, and M. Simons (2010a), Estimation of interplate coupling in the Nankai trough, Japan using GPS data from 1996 to 2006, *Geophysical Journal International*, *181*(3), 1313-1328.

Liu, Z., S. Owen, D. Dong, P. Lundgren, F. Webb, E. Hetland, M. Simons, (2010b), Integration of transient strain events with models of plate coupling and areas of great earthquakes in southwest Japan, 181, 1292-1312, *Geophys. J. Int*., doi:10.1111/j.1365-246X.2010.04599.x.

Lohman, R. B., and M. Simons (2005), Some thoughts on the use of InSAR data to constrain models of surface deformation: Noise structure and data downsampling, *Geochemistry, Geophysics, Geosystems*, *6*(1).

López-Quiroz, P., M.-P. Doin, F. Tupin, P. Briole, and J.-M. Nicolas (2009), Time series analysis of Mexico City subsidence constrained by radar interferometry, *Journal of Applied Geophysics*, *69*(1), 1-15.

Loveless, J. P., and B. J. Meade (2011), Spatial correlation of interseismic coupling and coseismic rupture extent of the 2011 MW= 9.0 Tohoku-oki earthquake, *Geophysical research letters*, *38*(17), L17306.

Mazzotti, S., X. Le Pichon, P. Henry, and S.-I. Miyazaki (2000), Full interseismic locking of the Nankai and Japan-west Kurile subduction zones: An analysis of uniform elastic strain accumulation in Japan constrained by permanent GPS, *Journal of Geophysical Research: Solid Earth*, *105*(B6), 13159-13177.

McCaffrey, R., L. M. Wallace, and J. Beavan (2008), Slow slip and frictional transition at low temperature at the Hikurangi subduction zone, *Nature Geoscience*, *1*(5), 316-320

Metois, M., A. Socquet, and C. Vigny (2012), Interseismic coupling, segmentation and mechanical behavior of the central Chile subduction zone, Journal of Geophysical Research: Solid Earth (1978–2012), 117(B3).

Newman, A. V., S. Y. Schwartz, V. Gonzalez, H. R. DeShon, J. M. Protti, and L. M. Dorman (2002), Along-strike variability in the seismogenic zone below Nicoya Peninsula, Costa Rica, *Geophysical research letters*, *29*(20), 1977.

Norabuena, E., T. H. Dixon, S. Schwartz, H. DeShon, A. Newman, M. Protti, V. Gonzalez, L. R. Dorman, E. R. Flueh, and P. Lundgren (2004), Geodetic and seismic constraints on some seismogenic zone processes in Costa Rica, *Journal of Geophysical Research-Solid Earth*, *109*, B11403.

Okada, Y. (1985), Surface deformation due to shear and tensile faults in a half-space, *Bulletin of the Seismological Society of America*, *75*(4), 1135-1154.

Outerbridge, K., T. Dixon, S. Schwartz, J. Walter, M. Protti, V. Gonzalez, J. Biggs, M. Thorwart, and W. Rabbel (2010), A tremor and slip event on the Cocos-Caribbean subduction zone as measured by a global positioning system (GPS) and seismic network on the Nicoya Peninsula, Costa Rica, *Journal of Geophysical Research: Solid Earth*, *115*(B10), B10408.

Parsons, B., T. Wright, P. Rowe, J. Andrews, J. Jackson, R. Walker, M. Khatib, M. Talebian, E. Bergman, and E. Engdahl (2006), The 1994 Sefidabeh (eastern Iran) earthquakes revisited: new evidence from satellite radar interferometry and carbonate dating about the growth of an active fold above a blind thrust fault, *Geophysical Journal International*, *164*(1), 202-217.

Pritchard, M. E., and E. J. Fielding (2008), A study of the 2006 and 2007 earthquake sequence of Pisco, Peru, with InSAR and teleseismic data, *Geophysical research letters*, *35*(9), L09308.

Pritchard, M. E., M. Simons, P. A. Rosen, S. Hensley, and F. H. Webb (2002), Co-seismic slip from the 1995 July 30 Mw= 8.1 Antofagasta, Chile, earthquake as constrained by InSAR and GPS observations, *Geophysical Journal International*, *150*(2), 362-376.

Protti, M., V. Gonzalez, A. V. Newman, T. H. Dixon, S. Y. Schwartz, J. S. Marshall, L. Feng, J. I. Walter, R. Malservisi, and S. E. Owen (2014), Nicoya earthquake rupture anticipated by geodetic measurement of the locked plate interface, *Nature Geosci*, *7*(2), 117-121.

Rosen, P. A., S. Henley, G. Peltzer, and M. Simons (2004), Updated repeat orbit interferometry package released, *Eos*, Transactions American Geophysical Union 85(5), 47-47.

Savage, J. (1983), A dislocation model of strain accumulation and release at a subduction zone, *Journal of Geophysical Research: Solid Earth (1978–2012)*, *88*(B6), 4984-4996.

Schwartz, S. Y., and J. M. Rokosky (2007), Slow slip events and seismic tremor at circum-Pacific subduction zones, *Reviews of Geophysics*, *45*(3).

Schwartz, S. Y., and H. DeShon (2007), Distinct up-dip limits to geodetic locking and microseismicity at the northern Costa Rica seismogenic zone: Evidence for two mechanical transitions, *The Seismogenic Zone of Subduction Thrust Faults*, 576-599.

Shelly, D. R. (2010), Migrating tremors illuminate complex deformation beneath the seismogenic San Andreas fault, Nature, 463(7281), 648-652.

Siebert, L., and T. Simkin (2002), Volcanoes of the World: An Illustrated Catalog of Holocene Volcanoes and Their Eruptions, Global Volcanism Program Digital Inf. Ser., vol. GVP-3, Smithsonian Inst., Washington,D. C. [Available at http://www.volcano.si.edu].

Simons, M., and P. Rosen (2007), Interferometric synthetic aperture radar geodesy, 391-446.

Sudhaus, H., and J. Sigurjón (2009), Improved source modelling through combined use of InSAR and GPS under consideration of correlated data errors: application to the June 2000 Kleifarvatn earthquake, Iceland, *Geophysical Journal International*, *176*(2), 389-404.

Tong, X., D. Sandwell, and B. Smith-Konter (2013), High-resolution interseismic velocity data along the San Andreas Fault from GPS and InSAR, *Journal of Geophysical Research: Solid Earth*, 1-21.

Tong, X., D. Sandwell, K. Luttrell, B. Brooks, M. Bevis, M. Shimada, J. Foster, R. Smalley, H. Parra, and J. C. Báez Soto (2010), The 2010 Maule, Chile earthquake: Downdip rupture limit revealed by space geodesy, *Geophysical research letters*, *37*(24).

Tryon, M. D., C. G. Wheat, and D. R. Hilton (2010), Fluid sources and pathways of the Costa Rica erosional convergent margin, *Geochemistry, Geophysics, Geosystems*, *11*(4).

Walter, J. I., S. Y. Schwartz, J. M. Protti, and V. Gonzalez (2011), Persistent tremor within the northern Costa Rica seismogenic zone, *Geophysical research letters*, *38*(1).

Walter, J. I., S. Y. Schwartz, M. Protti, and V. Gonzalez (2013), The synchronous occurrence of shallow tremor and very low frequency earthquakes offshore of the Nicoya Peninsula, Costa Rica, Geophysical research letters, 40(8), 1517-1522.

Wang, K., and T. Dixon (2004), "Coupling" Semantics and science in earthquake research, *Eos, Transactions American Geophysical Union*, *85*(18), 180-180.

Wessel, P., and W. H. F. Smith (1991), Free software helps map and display data, Eos Trans. AGU, 72, 441, doi:10.1029/90EO00319.

Yue, H., T. Lay, S. Y. Schwartz, L. Rivera, M. Protti, T. H. Dixon, S. Owen, and A. V. Newman (2013), The 5 September 2012 Nicoya, Costa Rica Mw 7.6 earthquake rupture process from joint inversion of high-rate GPS, strong-motion, and teleseismic P wave data and its relationship to adjacent plate boundary interface properties, *Journal of Geophysical Research: Solid Earth*, *118*(10), 5453-5466.

Zweck, C., J. T. Freymueller, and S. C. Cohen (2002), Three-dimensional elastic dislocation modeling of the postseismic response to the 1964 Alaska earthquake, Journal of Geophysical Research: Solid Earth (1978–2012), 107(B4), ECV 1-1-ECV 1-11.

Appendix 1-A: Synthetic Interferogram

To correct the residual orbital errors, we used the GPS derived interseismic model of *Feng et al.*, [2012]. The model is based on back slip in an elastic half space, in which the trench normal and vertical components of GPS velocities are inverted for back slip along the dip direction. To generate a synthetic interferogram (Figure 1-A1) from this model, we projected its predicted horizontal and vertical components at the ground surface to the SAR line of sight (LOS) direction using a unit vector of [0.60, 0.13, -0.79] in the east, north, and vertical directions. This unit vector was derived by using the average incidence angle of 38° and the heading direction of 12°. This synthetic interferogram shows that the accumulated LOS deformation is parallel to the trench with two deformation foci occurring at the southwest and central location of the Nicoya Peninsula coastline (Figure 1-A1). The LOS deformation rate is ~15-20 mm/yr near the coastline and decreases inland.

Appendix 1-B: Downsampled linear rate map

We applied a quadtree algorithm based on variance change to downsample the InSAR linear rate map [*Jónsson et al.*, 2002]. We masked the signal in the vicinity of the volcanic arc and downsampled the linear rate map using a variance threshold of 0.81 cm^2 to ~988 pixels. The downsampled linear rate map approximates the original LOS displacement well (Figure 1-A2).

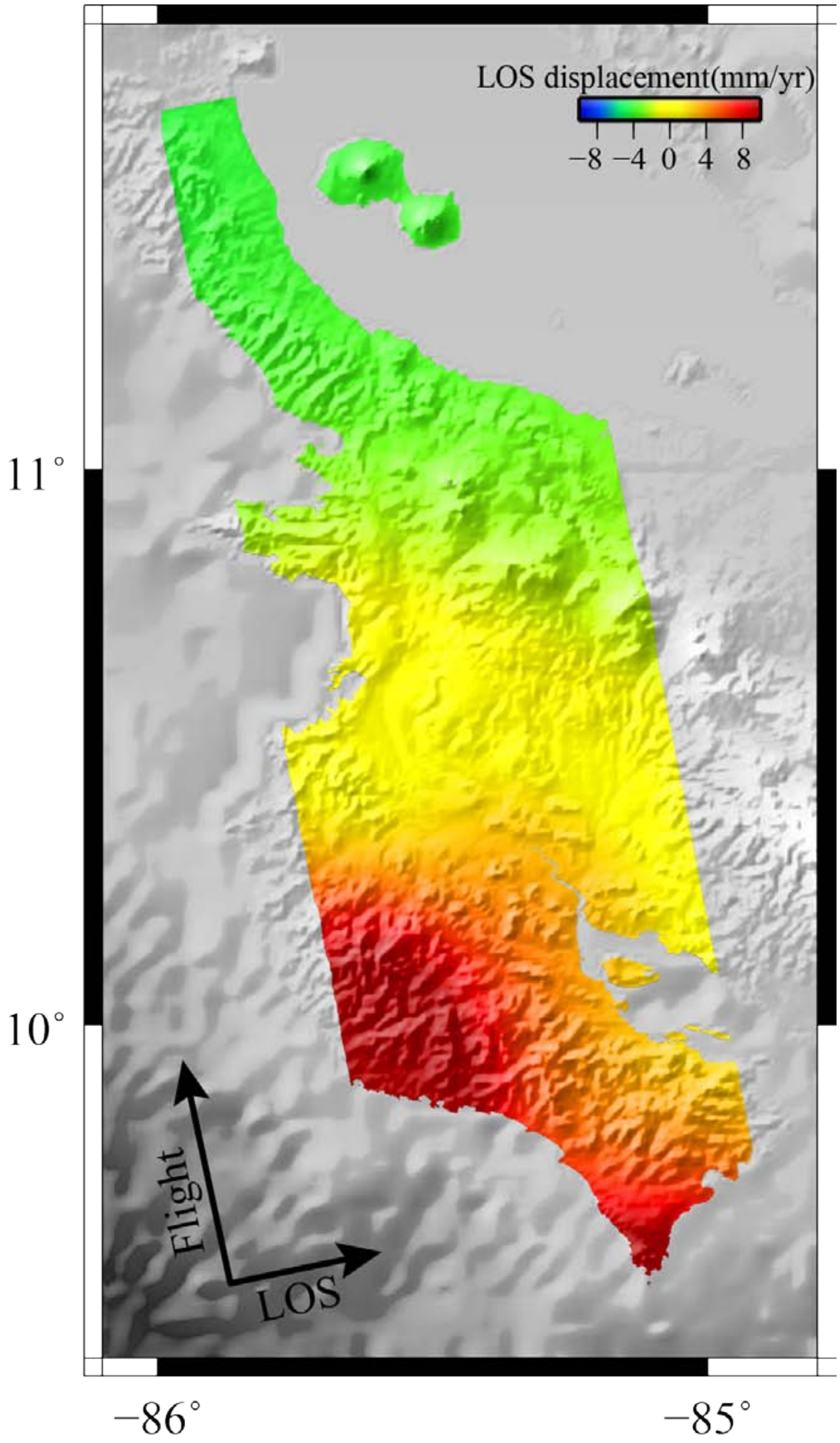

Figure 1-A1. LOS rate map using the interseismic model of *Feng et al.,* [2012]. Positive displacements indicate surface motion away from the satellite.

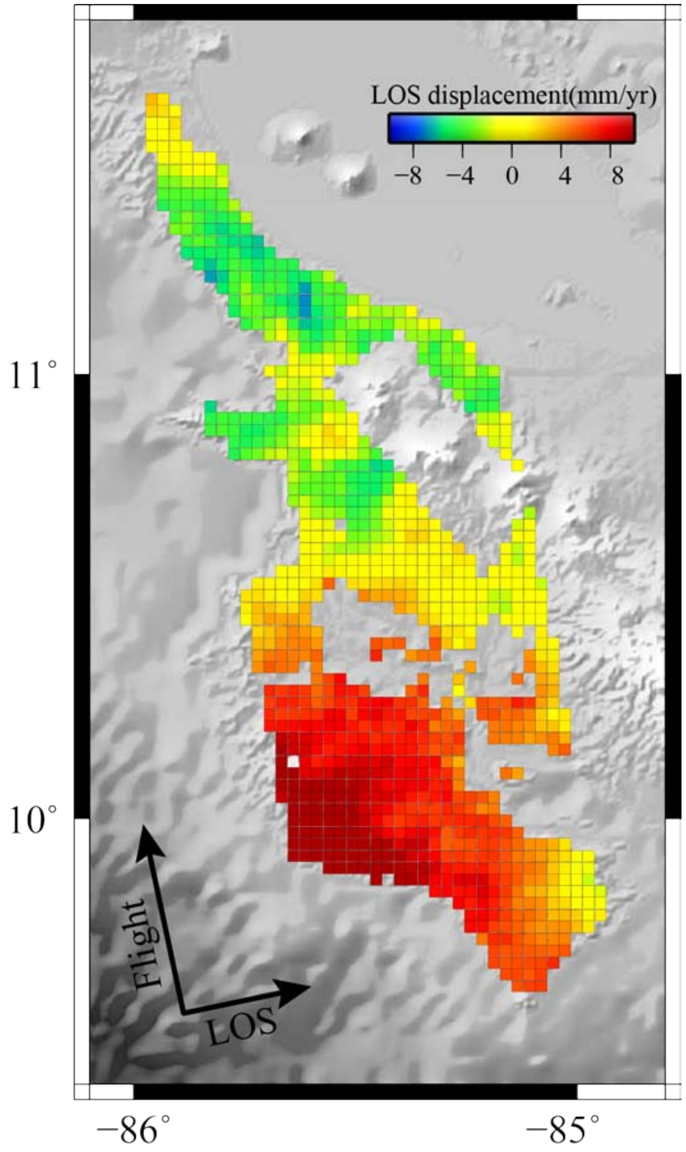

Figure 1-A2. Quadtree sampled InSAR linear rate map.

Appendix 1-C: Interseimic coupling model including both strike and dip components

We inverted for the back slip on the plate interface including both strike and dip components. The fault geometry was the same as described in the main text section

4.1. *Feng et al.,* [2012] show a uniform trench parallel velocity of 11 mm/yr for all the stations in the forearc region; to reduce the effect of the forearc motion of the Nicoya Peninsula, we subtracted an 11 mm/yr trench parallel component from the GPS horizontal velocities for all the stations, and excluded the GPS stations located on the east side of the volcanic arc. After removing an average sliver motion of 11 mm/yr, most of the GPS stations have < 2 mm/yr residual trench parallel motion. Four stations near the coast line have larger trench parallel motion (< 5 mm/yr) that could be caused by a strike slip component of interseismic strain accumulation on the plate interface. To consider this effect, we solved for both strike and dip back slip components on the plate interface. The GPS data used in this inversion include trench normal and residual trench parallel velocities after removing 11 mm/yr. Note that since the InSAR data are relative to the reference point in the forearc region, this removes most forearc motion in the InSAR data. The setup of the linear inverse problem and the constraints on the slip at fault boundaries are the same as described in the main text section 4.1. The slip vectors include both strike and dip components, and the Laplace smoothing operation is implemented on the strike and dip directions separately. We investigated the effect of different weighting factors between InSAR and GPS on the inversion by varying this parameter from 0.1 to 10. We found a weight of 4.5:1 between InSAR and GPS provides a good balance of fitting both data sets. The smoothing factor λ (=7) is determined by the trade-off between model roughness and weighted root mean square (WRMS) residual (Figure 1-A3d).

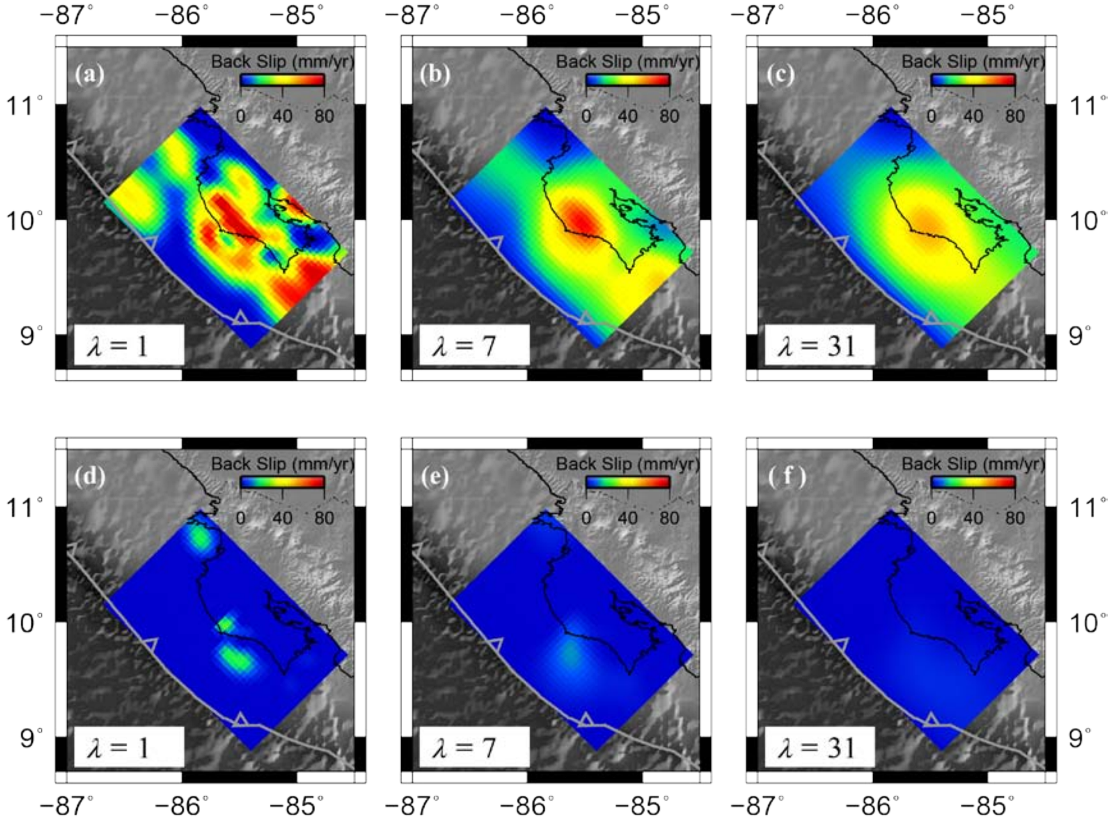

Figure 1-A3. Surface projection of the back slip in the dip direction for selected smoothing factors λ: (a) λ=1, (b) λ=7, (c) λ=31. Surface projection of the back slip in the strike direction for selected smoothing factors λ: (d) λ=1, (e) λ=7, (f) λ=31. The dataset includes GPS and InSAR data, and a weighting factor between GPS and InSAR of 1:4.5.

The coupling patterns using different smoothing factors are shown in the Figure 1-A3. These results show that the coupling pattern in the dip direction (Figure 1-A3a-c) has two centrally located locked patches, similar to the inversion for dip component only (see Figure 1-7 in the main text). The onshore locked patch persists even when a larger smoothing factor is used, while the offshore locked patch becomes smeared out when

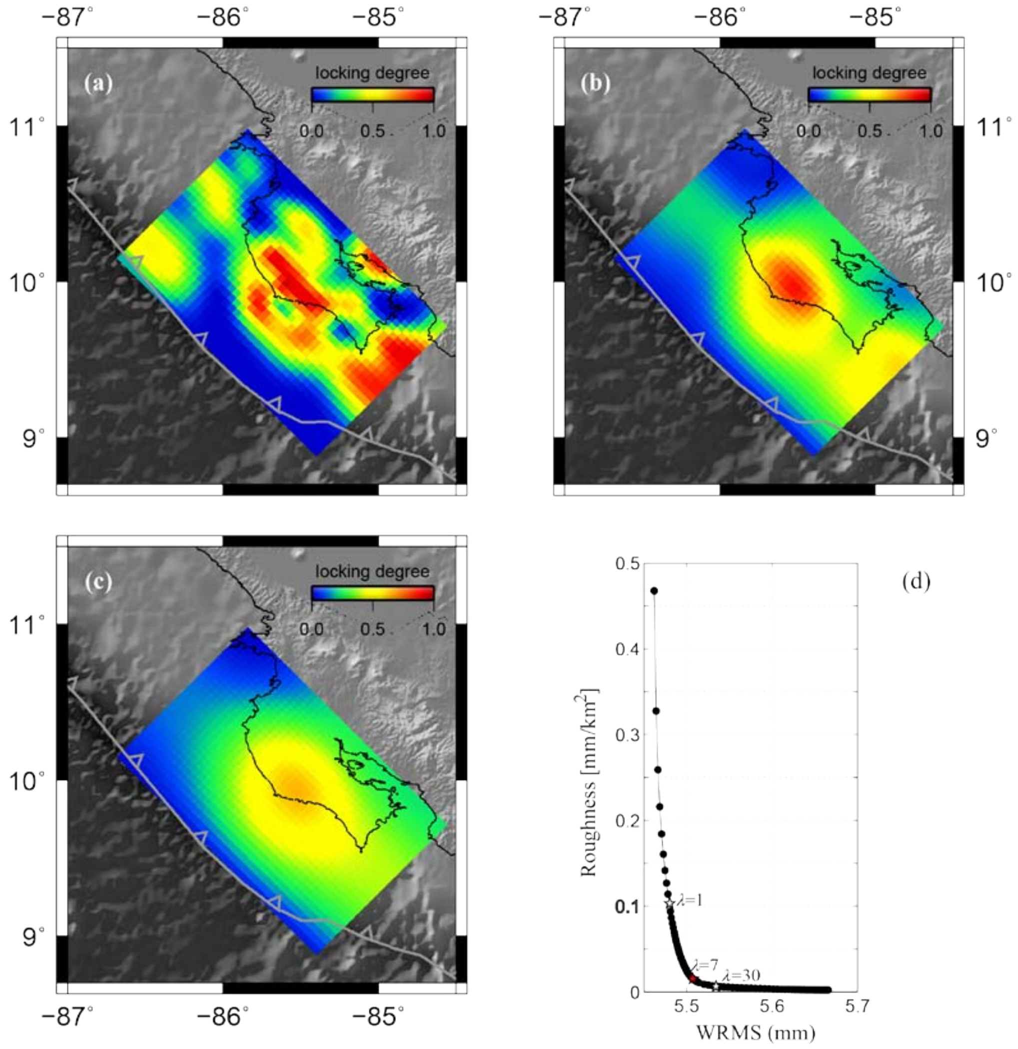

Figure 1-A4. Surface projection of the interseismic locking pattern for selected smoothing factors λ: (a) λ=1, (b) λ=7, (c) λ=31. (d) Trade-off curve between model roughness and the weighted root mean square (WRMS) residual of the model fit. The smoothing factor λ=7 is the turning point of this curve. The dataset includes GPS and InSAR data, and a weighting factor between GPS and InSAR of 1:4.5

the smoothing factor increases. The strike slip coupling pattern (Figure 1-A3d-f) shows a single locked patch offshore the central Nicoya Peninsula that becomes weaker when the smoothing factor increases. Even though λ=7 provides a good balance between roughness and WRMS (Figure 1-A4), this smoothing factor is too large to resolve refined features. We believe that inverting for locking in both dip and strike directions increases the number of parameters in the inversion thus requiring a larger smoothing factor to regularize the inversion. Because the contribution of the strike slip to the interseismic deformation is negligible compared to the dip slip component, we favor an interseismic coupling model that considers only the dip slip component.

Appendix 1-D: Tremor distribution

The Nicoya Peninsula is one of the subduction zones where tremor and very low frequency earthquakes (VLFEs) are common at shallow depth [*Walter, et al.,* 2011; *Walter, et al.,* 2013]. *Walter et al.* [2013] used a spectral detection method to identify and locate tremor during the 2008 Nicoya slow slip event (SSEs) (Figure 1-A5a). We used an automated envelope cross-correlation algorithm modified from *Wech and Creager* [2008] to locate tremor during the 2009 and 2010 Nicoya SSEs. Tremor locations are poor due to the difficulty of identifying individual P and S wave arrival times. We therefore only retain tremor locations that fall within +-10 km of the plate interface. The results indicate that most of the tremor accompanying the 2008, 2009 and 2010 Nicoya slow slip events occurs offshore (Figure 1-A5a-c). Moreover, *Walter et al.,* [2013] used a beamforming technique to detect VLFEs embedded within the 2008 tremor. The distances and azimuths of the VLFE are consistent with the tremor locations, offshore of the Nicoya Peninsula. The tremor and possible VLFEs that appear to occur adjacent to and overlap with offshore strongly coupled patch (Figure 1-A5a-c) suggest that this patch has different mechanical properties from the onshore locked patch.

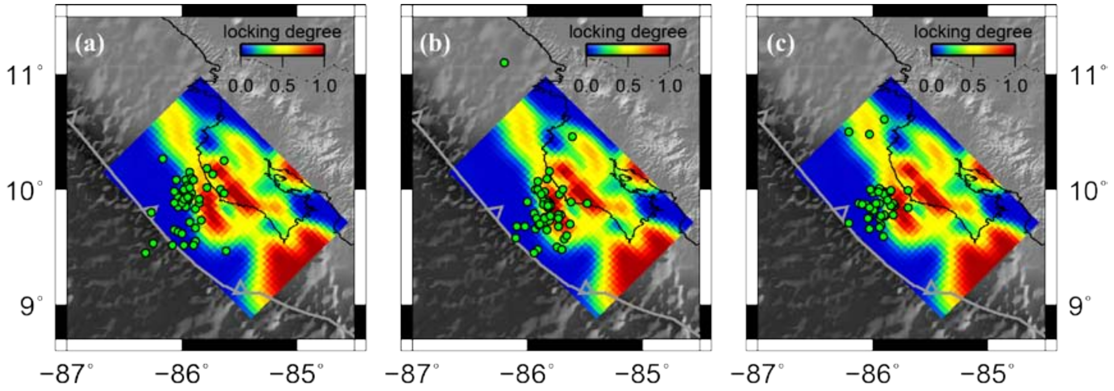

Figure 1-A5. Tremor distributions during slow slip events in (a) 2008 [*Walter et al.*, 2011], (b) 2009 and (c) 2010. The tremor locations determined in 2009 and 2010 were determined using an envelope cross-correlation algorithm modified from *Wech and Creager* [2008]. The color patches show our preferred coupling model determined in the dip direction only.

Appendix 1-E: Stratified atmospheric signal

The stratified atmospheric signal for the entire image is not significant as indicated by the linear relationship between phase and elevation (Figure 1-A6). The signal of the volcanic arc region is masked for the inversion problem. We fit a linear relationship to the phase which excludes residual orbital signal and deformation signal and the corresponding attitude for all the pairs used in the construction of InSAR time-series. The distributions of slope for all the pairs are random (Figure 1-A6), so it does not affect the linear velocity estimates.

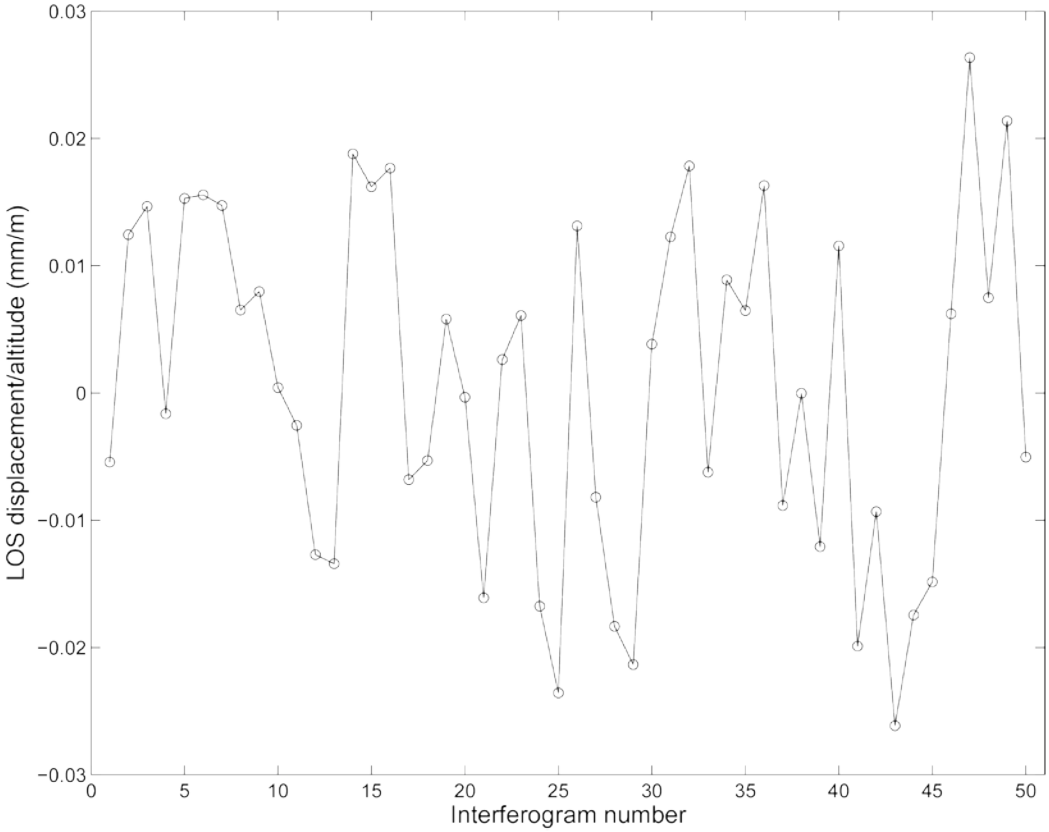

Figure 1-A6. The distribution of the slope of the phase vs. altitude for all pairs used in the construction of the InSAR time series.

Appendix 1-F: Uncertainties of the preferred coupling model

To estimate the uncertainties in the preferred coupling model, we use a Monte Carlo simulation to estimate the confidence intervals of the coupling ratio on each fault patch. Different realizations of noise are added to synthetic InSAR and GPS data generated from the preferred coupling model for each simulation, and the synthetic data are inverted using the constrained inversion. GPS noise is simulated from a

Gaussian distribution with zero mean and the same variance as the observed data. The InSAR noise is generated by the same method described in the main text section 2.5. The weighting and the smoothing factors used in the inversion are the same values used for the preferred coupling model. The simulation is repeated 4×10^4 times and the standard deviation of the coupling ratio at each patch (Figure 1-A7) indicates the uncertainty of the inverted model. The largest standard deviation of all of the patches is < 0.28, suggesting that our coupling model is robust. The fault patches near the trench with small standard deviations are an artifact of the constrained inversion. They are not well resolved because of the lack of the data coverage, so the results are biased to values close to the slip bound by the constrained inversion.

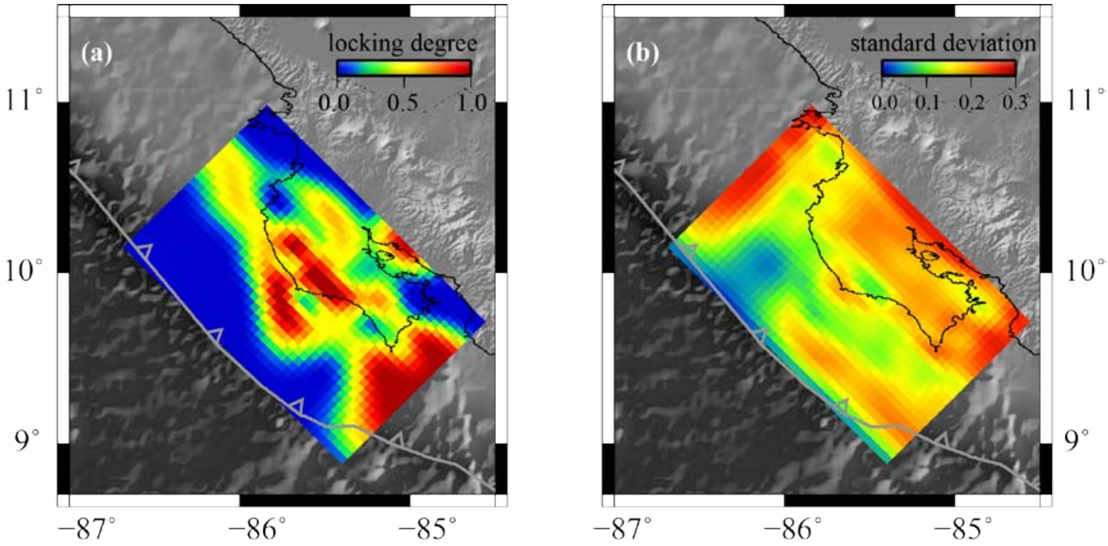

Figure 1-A7. (a) The preferred coupling model, and (b) The standard deviation of the coupling ratio on each fault patch.

Appendix 1-G: Checkerboard test of InSAR/GPS integrated and GPS only models

To compare the spatial resolution of the GPS only and the InSAR/GPS integrated coupling models, we performed a checkerboard test using the two data sets separately. For these checkerboard tests, we consider only the dip slip component of motion. Since the InSAR/GPS integrated model has finer features, we divided the fault surface into ~25×25 km^2 patches, a smaller size than shown in the main text, and imposed an input model with an alternating pattern of full and zero back slip (Figure 1-A8a). The checkerboard test of the InSAR/GPS integrated model was performed in the same manner as described in the main text section 4.2 except for the size of the imposed patches. We used the same alternating slip pattern to generate synthetic GPS data, adding random noise that followed a normal distribution with zero mean and the same uncertainty as the observed GPS data. The checkerboard test of GPS only model followed the same procedure as previously described and used an optimized smoothing factor of 1 (obtained from the curve of the roughness versus the weighted data misfit from the inverted models using GPS data only). Comparison of the results of the two checkerboard tests (Figure 1-A8) indicates that resolution of the InSAR/GPS data is superior to GPS data only beneath land and near the coastline. Both data sets lack the resolution near the trench.

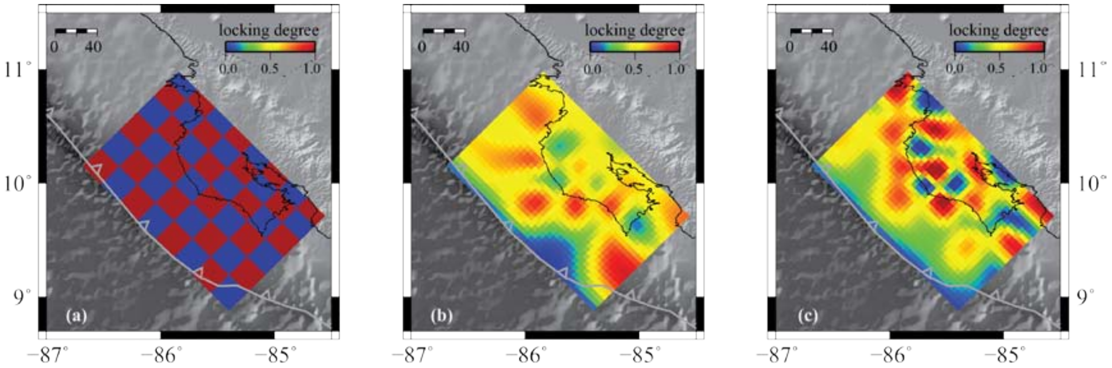

Figure 1-A8. Checkerboard test showing the spatial resolution of InSAR/GPS model and GPS only model. (a) the imposed locking pattern, (b) recovered locking pattern using GPS data only at λ=1 which is the optimized smoothing factor from the curve of the roughness and the weighted data misfit of the inverted models using GPS data only, (c) recovered locking pattern using both InSAR and GPS data using λ=1 which is our preferred smooth factor in the inversion. The weighting factor between GPS and InSAR is 1:4.2.

References

Feng, L., A. V. Newman, M. Protti, V. González, Y. Jiang, and T. H. Dixon (2012), Active deformation near the Nicoya Peninsula, northwestern Costa Rica, between 1996 and 2010: Interseismic megathrust coupling, *Journal of Geophysical Research: Solid Earth (1978–2012)*, *117*(B6).

Jónsson, S., H. Zebker, P. Segall, and F. Amelung (2002), Fault slip distribution of the 1999 Mw 7.1 Hector Mine, California, earthquake, estimated from satellite radar and GPS measurements, *Bulletin of the Seismological Society of America*, *92*(4), 1377-1389.

Walter, J. I., S. Y. Schwartz, J. M. Protti, and V. Gonzalez (2011), Persistent tremor within the northern Costa Rica seismogenic zone, *Geophysical research letters*, *38*(1).

Walter, J. I., S. Y. Schwartz, M. Protti, and V. Gonzalez (2013), The synchronous occurrence of shallow tremor and very low frequency earthquakes offshore of the Nicoya Peninsula, Costa Rica, Geophysical research letters, 40(8), 1517-1522.

Wech, A. G., and K. C. Creager (2008), Automated detection and location of Cascadia tremor, Geophysical research letters, 35(20), L20302.

Chapter 2. Long-term temperature records following the M_w 7.9 Wenchuan (China) earthquake are consistent with low friction

Haibing Li[1]*, Lian Xue[2], Emily E. Brodsky[2], James Mori[3], Patrick M. Fulton[2], Huan Wang[1], Yasuyuki Kano[3], Kun Yun[1], Robert N. Harris[4], Zheng Gong[1], Chenglong Li[1], Jialiang Si[1], Zhiming Sun[5], Junling Pei[5], Yong Zheng[1], and Zhiqin Xu[1]

[1]State Key Laboratory of Continental Tectonics and Dynamics, Institute of Geology, Chinese Academy of Geological Sciences, Beijing, China

[2]Department of Earth & Planetary Sciences, University of California–Santa Cruz, Santa Cruz, California 95064, USA

[3]Disaster Prevention Research Institution, Kyoto University, Gokasho, Uji, Kyoto, Japan

[4]Oregon State University, Corvallis, Oregon 97331, USA

[5]Institute of Geomechanics, Chinese Academy of Geological Sciences, Beijing, China

*****This paper is published as Li, H., and L. Xue., et al. (2015), Long-term temperature records following the Mw 7.9 Wenchuan (China) earthquake are consistent with low friction, Geology, 43(2), 163-166.

Abstract

Knowledge of the shear stress on a fault during slip is necessary for a physical-based understanding of earthquakes. Borehole temperature measurements inside the fault zone immediately after an earthquake can record the energy dissipated by this stress.

In the first Wenchuan Earthquake Fault Zone Scientific Drilling Project hole (Sichuan province, China) we repeatedly measured temperature profiles from 1.3 to 5.3 yr after the 12 May 2008, M_w 7.9 Wenchuan earthquake. The previously identified candidate for the principal slip surface had only a small local temperature increase of at most 0.02 °C with no obvious decay. The small amplitude of the temperature increase provides an upper bound for the frictional heat–generated coseismic slip, but is unlikely to be a frictionally generated signal. Two larger temperature anomalies are located above and within the fault zone. However, neither anomaly evolves as expected from a frictional transient. We conclude that the frictional heat from the Wenchuan earthquake remains elusive and the total heat generated at this location is much less than 29 MJ/m^2. Low friction during slip is consistent with the temperature data.

2-1 Introduction

The magnitude of the shear stress resisting slip along a fault during an earthquake has long been unknown. Recent measurements have shown that a straightforward application of Byerlee’s law with a coefficient of friction of 0.6 for most rocks and 0.2 for clays may not yield the correct shear stress at high speeds [*Byerlee,* 1978]. At typical earthquake slip velocities of 1 m/s, laboratory values of friction plummet and span a range of values from 0.05 to 0.4, depending on lithology and experimental conditions [*Di Toro et al.,* 2011]. The theory controlling high-velocity friction is vigorously debated, and nonfrictional processes can alter the local shear stress in natural systems. Field measurements are needed to constrain the magnitude of shear resistance during earthquakes on actual faults.

To address this observational gap, rapid response drilling projects have measured the temperature in fault zones directly after major earthquakes. Single profiles in both shallow and deep boreholes after the 1999 M_w 7.7 Chi-Chi earthquake (Taiwan) recorded temperature anomalies interpreted to be equivalent to a dynamic coefficient of friction of ~0.1 [*Tanaka et al.*, 2006; *Kano et al.*, 2006] and a similar value was inferred for the 2011 M_w 9.0 Tohoku earthquake (Japan) from the Japan Trench Fast Drilling Project [*Fulton et al.*, 2013]. All of these experiments tracked the temperature over <1 yr.

In this paper, we report on borehole temperature measurements made across the fault zone that ruptured during the 12 May 2008 M_w 7.9 Wenchuan (Sichuan province, China) earthquake, continuing from 1.3 to 5.3 yr after the event. We use the temperature data and thermal conductivity measurements to place an upper bound on the coseismic friction on the fault.

2-2 Methods and Strategy

The Wenchuan Fault Earthquake Zone Scientific Drilling Project (WFSD) has successfully collected a data set over a 4 yr period with 23 temperature profiles in a single borehole. The measurement hole (WFSD-1; Figure 2-1A) was drilled from November 2008 to July 2009 to a maximum depth of 1201 m (Figure 2-1B) with a cased interval to a depth of ~810 m.

The borehole intersects a major fault at 589 m borehole (core) depth, i.e., as measured along the hole, which is equivalent to 578 m vertical depth (all depths in this article are borehole depths, unless otherwise specified). The 589 m fault is near the boundary between the Neoproterozoic Pengguan complex, which here consists of diorite, porphyrite, pyroclastics and other volcanics, and the Late Triassic Xujiahe Formation, which here consists of interbedded sandstone and shale [*Li et al.*, 2013]. The cataclasite, fault breccia, and fault gouge layers in the core continue to 759 m core depth (746 m vertical depth). Multiple faults exist throughout the 589–759 m zone, and the identification of a single principal slip surface corresponding to the 2008 Wenchuan earthquake is difficult. Togo *et al.* [2011b] reported that at a nearby surface outcrop, the surface break is localized on the Sichuan basin side of the fault zone packet, which corresponds to the 759 m depth in the core. However, internal evidence from the core suggests that the 589 m fault is the strongest candidate for the principal slip zone of the Wenchuan earthquake because of the fresh gouge appearance, microstructures relating to coseismic slip, high magnetic susceptibility values [*Li et al.*, 2013], clay mineral composition in cores [*Si et al.*, 2014], borehole logging data [*Li et al.*, 2014], and drilling mud gas concentrations [*Tang et al.*, 2013]. Breaking both the surface rupture on the basin side and the 589 m fault at depth during the Wenchuan earthquake either requires a 65° dipping fault crossing the gouge packet [*Li et al.*, 2013] or, more likely, slip transfer across the packet on to the subparallel en echelon surfaces.

Repeated temperature measurements were made in the well from October 2009 through September 2013 (Figure 2-1C). For each of the 23 profiles, temperature was measured by lowering a string of two or three temperature sensors (RBR Ltd. model 1050/2050) at a rate of ~1 m/min downward through the well to the bottom of the casing (800 m) and then raising the string at the same rate. Measurements were recorded every second and a built-in pressure sensor was intended to record depth. Only the down going data from the bottom sensor are interpreted because both the trailing sensors and up going runs are affected by the disturbance of the fluid in the well during temperature logging. For three profiles from June and December 2012, a stop-go logging technique was used with the sensor held stationary for at least 90 s to allow equilibration at fixed intervals that varied between 0.2 and 1 m. The data were then fit through the hold time to find the asymptotic steady-state temperature for comparison with data obtained with the sensors in motion [*Harris and* Chapman, 2007]. The profile from 20 September 2011 was unusable due to a faulty pressure sensor. Profiles on 23 October 2009 and 23 June 2012 do not extend through the cased zone and the 18 October 2010 profile was lowered too quickly for accurate temperature gradient estimates. The remaining 19 profiles were used for the following analysis.

We used the temperature gradient change associated with a change of lithology documented in the core and gamma ray logs at core depth of 394 m to align the logs (Figs. 2-A1 and 2-A2 in the Appendix 2-A) because instrumental problems and variable densities in the muddy water in the borehole made the depth inferred from the pressure transducer inaccurate. The shifted 19 profiles overlay almost exactly, indicating that the data quality is good and the long-term geothermal gradient of ~0.02 °C/m is stable (Figure 2-1C). This inference of stability is independent of the corrections applied here.

The temperature measurements are interpreted in conjunction with measurements of thermal conductivity of the recovered core (see the Appendix 2-B). The thermal conductivity was measured by an optical scanner at 5 m intervals over the core from 350 to 800 m depth with denser sampling near 589 m under dry conditions. Saturated thermal conductivities are estimated from a composite thermal model (the Appendix 2-B. Eqs. (2-B1)-(2-B2) as described in the Appendix 2-B.

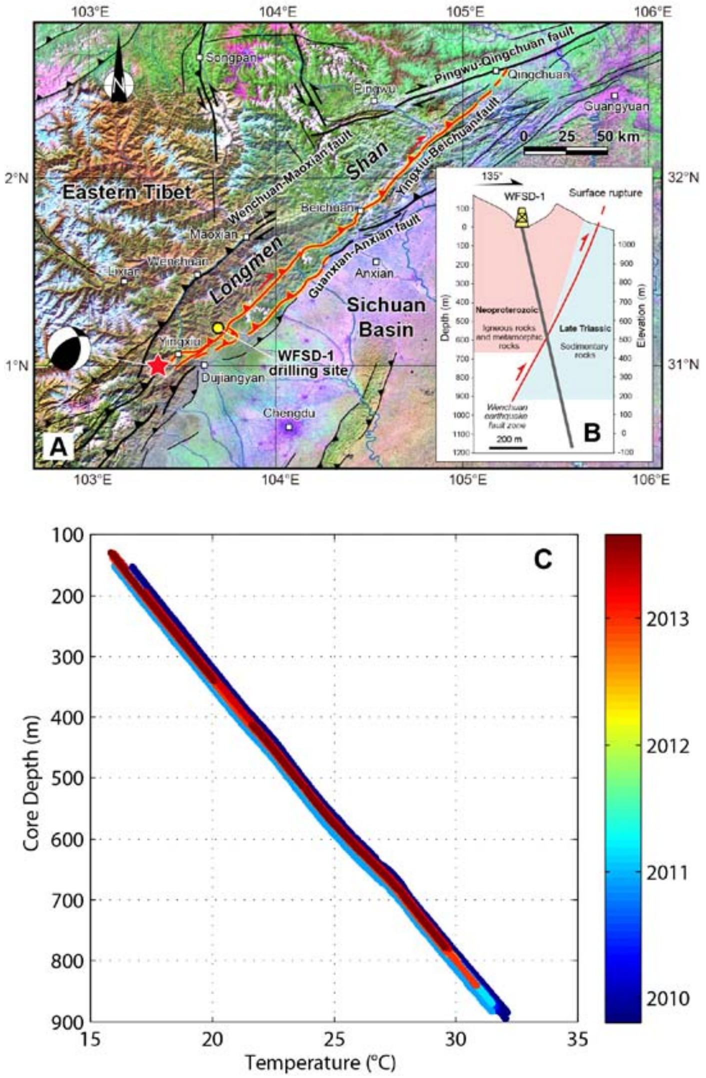

Figure 2-1. Location of Wenchuan Earthquake Fault Zone Scientific Drilling hole (WFSD-1) Sichuan province, China, and observed temperature profiles. A: Map of major active faults of the Longmen Shan area and WFSD-1 location. Red lines show coseismic surface rupture. Red star denotes epicenter of the 2008 earthquake main shock. B: Simple geologic cross section at the WFSD-1 site, including the 1201-m-deep hole (gray line) and candidate Wenchuan earthquake fault. C: Temperature profiles in the WFSD-1 hole (short profile on 23 October 2009 and profile with malfunctioning sensor on 20 September 2011 are omitted). The profiles are vertically aligned using small-scale features (see text) (Figs. 2-A1 and 2-A2).

2-3 Thermal Observations

Just below the previously identified candidate principal slip zone at 589 m core depth, a small 15-m-wide temperature deviation of 0.02 °C persisted throughout the observation period. The perturbation to the geotherm is most clearly resolved by the highest precision experiments that used stop-go logging (Figure 2-2B). These high-precision logs also have the best depth control of any data collected. Similar amplitude temperature perturbations exist elsewhere in all profiles taken after the end of drilling. A temperature log taken during drilling reported a 0.15 °C anomaly at this same location [*Li et al.*, 2014; Figure 2]; however, as the drilling was stuck at ~590 m for over 30 days due to the difficulties of penetrating the fault zone, the early time data are strongly influenced by the drilling fluid temperature (see the Appendix 2-D). For the data considered here, only the association with the strongest geological candidate for the principal slip zone distinguishes the 0.02 °C feature as worthy of further examination.

A larger feature in the temperature profile is centered at ~690 m depth with a width of ~130 m, which nearly spans the fault zone (Figure 2-2A). The amplitude decays from 0.25 °C to 0.20 °C over the observation interval, but the width does not change. Above the primary fault zone, a feature with a similar width but smaller amplitude is centered at ~450 m. All of these features exist in both the continuous and the stop-go logs, indicating that sensor reequilibration is not a factor in their identification.

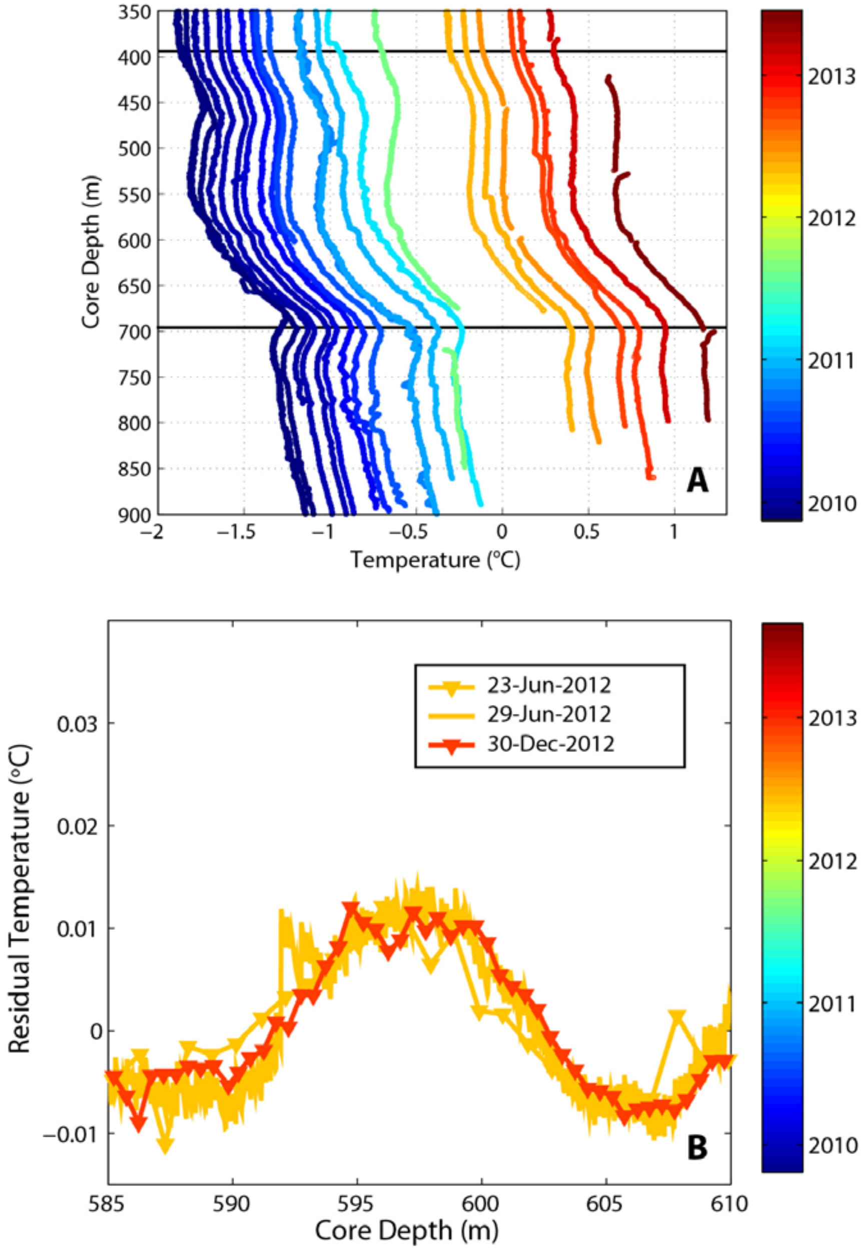

Figure 2-2. Temperature profiles with a constant gradient of 0.02 °C/m removed. For clarity, profiles are shifted on the x axis in proportion to the time since the earthquake. A: Complete data set. Data are interpretable at depths below the seasonal and hydrologically driven changes in temperature within the casing. We focus on 350–800 m depths. B: Close-up of the 589 m zone from the high-precision stop-go logs with arbitrary zeros. Apparent smoothing of the logs is due to detrending. Stop-go logs are not available for other periods (Fig. 2-A7).

We follow standard interpretive procedure and examine temperature as a function of thermal resistance to form a Bullard plot [*Beardsmore and Cull*, 2001]. Thermal resistance incorporates variations in thermal conductivity and the procedure allows us to estimate the steady-state conductive heat flow. The mean resultant heat flow is 69 mW/m^2 with a range of 68–70 mW/m^2 over all the profiles (see the Appendix 2-B). We remove the steady-state conductive temperature profile at each depth and define the residual temperature as the anomaly (Figure 2-3A). The resultant anomalous temperature rise over the 589 m fault is still small and no anomaly >0.01 °C exists over the second candidate fault zone at 759 m. The wider features noted in the raw data are also anomalies in the residual temperature centered at 450 m and 690 m depth.

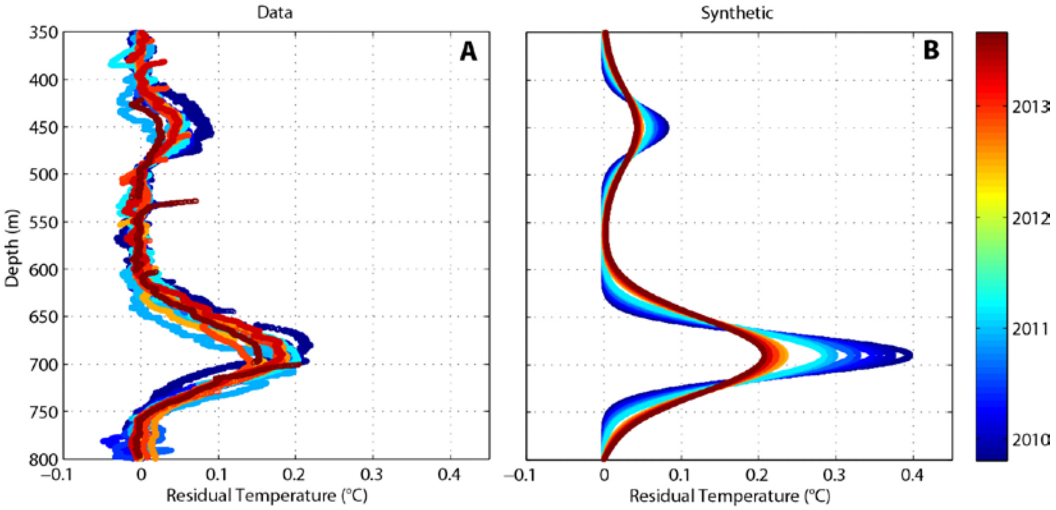

Figure 2-3. Residual (anomalous) temperature after the conductive geotherm is removed. A: Observed residual temperature for each profile color coded by date. Thermal conductivity structure is in Table 2-A1. B: Modeled residual temperature for frictional dissipation on 450 m and 690 m surfaces with diffusive heat transport. Total dissipated energy is constrained by the observed residual thermal energy (see the

Appendix 2-C). The time evolution in the model in B is absent in the observations in A, suggesting that the anomalies are not due to the diffusion of a frictional heat.

2-4 Analysis of Thermal Anomalies

In our search for the frictionally generated heat, we first consider the largest thermal anomalies: the 450 and 690 m depth features. Although there is no well-developed fault plane documented at either of 450 or 690 m depth, there are fault breccias within each of the anomalies (Figure 3 of *Li et al.,* [2013]).

If these thermal anomalies are frictionally generated, the residual temperature provides a direct constraint on the thermal energy S generated on the faults, i.e.,

$$S = \int \rho C_p \Delta T dz \tag{2-1}$$

where ρ is the density and c_p is the heat capacity. Estimating c_p = 800 J/m^3 [*Beardsmore and Cull,* 2001] and ρ = 2500 kg/m^3 [*Li et al.*, 2014] results in S of 5 ± 2 MJ/m^2 at 450 m and 24 ± 6 MJ/m^2 at 690 m; error ranges indicate 1 standard deviation on the estimates over the suite of profiles.

To test the consistency of the data with a frictional model, we calculate the evolution of the temperature field over time assuming that the thermal energy is generated on fault planes at 450 and 690 m depth and diffuses into the surrounding rock (Figure 2-3B). The diffusive model predicts that the anomalies should widen and decay resolvably in amplitude over time. Although some reduction is seen in the 450 m depth anomaly, neither observed anomaly widens over time and both are narrower than predicted at the end of the study period.

We conclude that the lack of observed time evolution implies that the 450 m and 690 m anomalies are unlikely to be due to diffusion of frictional heat away from a fault. These anomalies could be the result of frictional heating combined with another source of heat transport. For example, advective flow could generate a narrow thermal pulse limited by the high hydraulic diffusivity structure in the damage abutting the main fault zone [*Fulton et al.*, 2010; *Xue et al.*, 2013]. A fluid flow explanation is qualitatively the most attractive possibility, and detailed modeling of such a fluid flow is the focus of future work. We confine ourselves here to concluding that the temperature data provide an upper bound of 29 MJ/m^2 of frictionally dissipated energy. The heat energy could have been dissipated on any number of planes within the region; there is no direct constraint on the localization of the energy.

The geologically significant 589 m depth fault has a subtle temperature increase. However, the width of a frictionally generated anomaly is predicted to be much greater than observed. For a homogeneous medium with a thermal diffusivity of 1.5×10^{-6} m^2/s and heat generation at the time of the earthquake, the anomaly is expected to be ~100 m wide at the time of measurement, which is not observed (Figure 2-2B). Furthermore, the signal does not decay or widen (Figs. 2-A2 and 2-A7).

The temperature increase at 589 m could be attributed to a gradient change associated with local thermal conductivity structure. We evaluate this possibility in Figure 2-4 by calculating the steady-state thermal profile consistent with the full suite of thermal conductivity measurements in the 589 m zone and a constant heat flow of 69 mW/m^2

constrained by the analysis in Figure 2-3. The procedure is similar to that of Tanaka *et al.* (2007). Although the symmetry of the observed temperature increase is not reproduced by a realistic thermal conductivity structure, the measured variation in thermal conductivity suggests an even larger range of temperatures than observed.

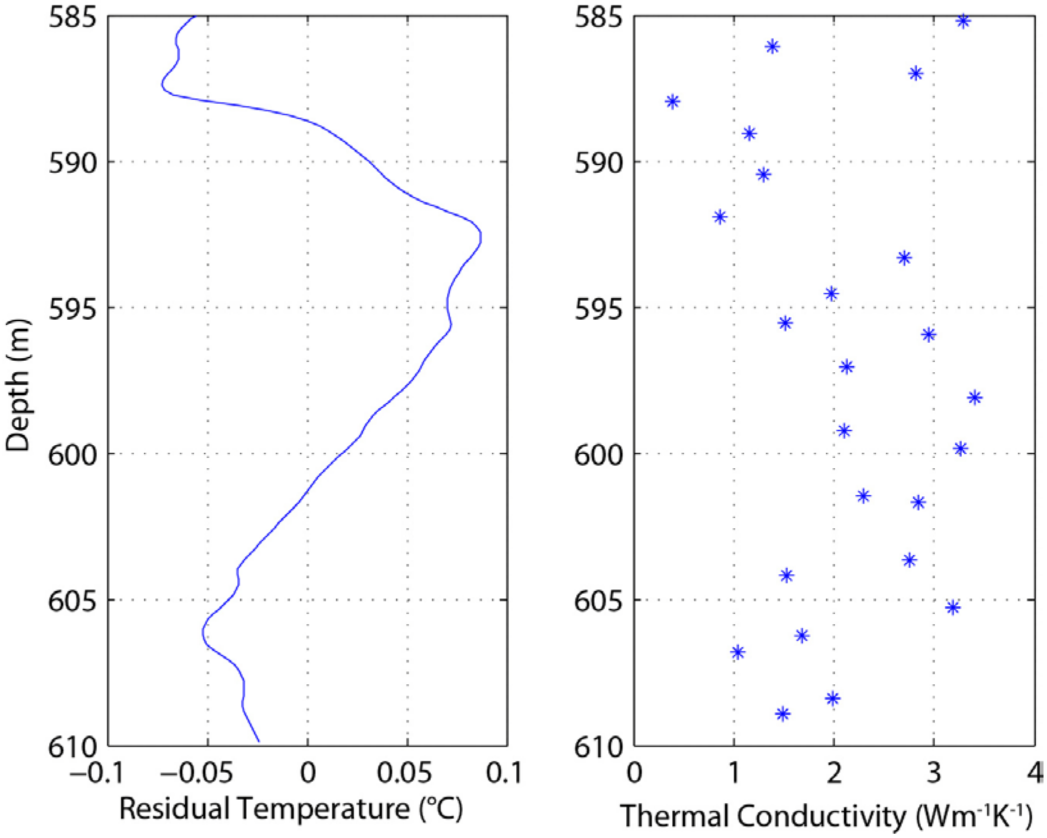

Figure 2-4. Steady-state temperature profile with variable thermal conductivity. At each depth, we divide the heat flow of 69 mW/m^2 as constrained by Figure 3 by the local thermal conductivity measured on the core to infer the local thermal gradient. We integrate the gradient and detrend the resultant 590–610 m depth temperature profile for comparison with Figure 2B.

Here we use only the dry laboratory values and therefore Figure 2-4 may over-estimate thermal conductivity variations. In the model of Figure 2-A3, we took the opposite approach and designed an inversion in which porosity completely compensates for thermal conductivity variations in the laboratory samples. Figure 2-4 is primarily useful as a warning of the potential effects of heterogeneous structure, but is unlikely to provide an accurate estimate of the residual temperature as saturation effects are not included. We have already concluded based on the width and lack of time dependence that the temperature increase below 589 m is unlikely to be frictionally generated and now modeling shown in Figure 2-4 permits the feature to be the result of heterogeneous thermal conductivity structure.

The lack of a resolvable frictional heat anomaly yields an upper bound for frictional heat dissipated here during the earthquake. For frictional heating during slip, the decay of the peak temperature, T, on a planar fault due to one-dimensional heat conduction away from the fault is

$$T = (\mu \sigma_n d / c_p \rho) / [2(\pi \kappa t)^{1/2}] \qquad \text{(2-2)}$$

where μ is the average coefficient of friction during slip, σ_n is the effective normal stress, d is the slip, c_p is the specific heat capacity, ρ is the density, κ is the thermal diffusivity, and t is the time elapsed since the event [*Carslaw and Jaeger*, 1959]. The model of Equation 2-2 is for an infinitesimally thin fault. The times of the data recorded here are sufficiently long after the earthquake that a thermal anomaly would have spread over a region larger than the shear width and the planar solution is indistinguishable from the finite shear zone solution. Based on Equation 2-2 and a normal stress on the fault equal to the lithostatic overburden less the hydrostatic pore pressure, the 0.02° C upper bound in the 589 m zone implies that the effective coefficient of friction during the earthquake is <0.02 if 7 m of slip happened on this surface (see Figure 2-A6 caption for parameters). Although the bound in terms of the coefficient of friction enables easy comparison with previous work, dynamic reduction of normal stress or inaccurate estimate of slip are also acceptable explanations of the data. The data most directly constrain the dissipated heat energy, which over the depth of Figure 2-2B is <1.2 MJ/m^2.

2-5 Conclusions

In summary, the total energy dissipated frictionally at the locale penetrated by the WFSD-1 borehole is <29 MJ/m^2 and the dissipated energy on the previously identified fault surface is <1.2 MJ/m^2. The upper bound for the entire zone (29 MJ/m^2) is less than would be anticipated with a coefficient of friction of 0.6, but could be consistent with the range of coefficients of friction seen in dynamic weakening experiments [*Di Toro et al.*, 2011]. Other studies have inferred dramatic weakening for the Wenchuan fault material based on laboratory studies of fault zone rocks from surface outcrops subject to high-velocity shear [*Togo et al.*, 2011a; *Chen et al.*, 2013; *Yao et al.*, 2013; *Zhang and He,* 2013]. The high organic and clay content or presence of graphite may be critical factors [*Zhang and He*, 2013; *Kuo et al.*, 2014]. All of the cited studies concluded that the coefficient of friction during slip was <0.2, which would be consistent with the upper bound on the dissipated energy. The Wenchuan earthquake fault appears to have been weak during slip.

2-6 Acknowledgments

This research was supported by the Chinese National Science and Technology Planning Project (Wenchuan Earthquake Fault Zone Scientific Drilling Project, WFSD), National Science Foundation of China grant 41330211 (to Li) and U.S. National Science Foundation grant EAR-1220642 (Brodsky). We thank W. Zhang, G. Yang, R. Guo, and Y. Huang for data collection assistance. Detailed reviews from T. Shimamoto, S. Nielsen and an anonymous reviewer are enormously appreciated.

2-7 References

Beardsmore, G.R., and Cull, J.P., 2001, Crustal heat flow: A guide to measurement and modelling: Cambridge, UK, Cambridge University Press, 336 p.

Byerlee, J., 1978, Friction of rocks: Pure and Applied Geophysics, v. 116, p. 615–626, doi:10.1007/BF00876528.

Carslaw, H.S., and Jaeger, J.C., 1959, Conduction of heat in solids: Oxford, UK, Clarendon Press, 51 p.

Chen, J., Yang, X., Duan, Q., Shimamoto, T., and Spiers, C.J., 2013, Importance of thermochemical pressurization in the dynamic weakening of the Longmenshan fault during the 2008 Wenchuan earthquake: Inferences from experiments and modeling: Journal of Geophysical Research, v. 118, p. 4145–4169, doi:10.1002/jgrb.50260.

Di Toro, G., Han, R., Hirose, T., De Paola, N., Nielsen, S., Mizoguchi, K., Ferri, F., Cocco, M., and Shimamoto, T., 2011, Fault lubrication during earthquakes: Nature, v. 471, p. 494–498, doi:10.1038/nature09838.

Fulton, P.M., et al., 2013, Low coseismic friction on the Tohoku-Oki fault determined from temperature measurements: Science, v. 342, p. 1214–1217, doi:10.1126/science.1243641.

Fulton, P.M., Harris, R.N., Saffer, D.M., and Brodsky, E.E., 2010, Does hydrologic circulation mask frictional heat on faults after large earthquakes?: Journal of Geophysical Research, v. 115, B09402, doi:10.1029/2009JB007103.

Harris, R.N., and Chapman, D.S., 2007, Stop-go temperature logging for precision applications: Geophysics, v. 72, p. E119–E123, doi:10.1190/1.2734382.

Kano, Y., Mori, M., Fujio, R., Ito, H., Yanagidani, T., Nakao, S., and Ma, K.-F., 2006, Heat signature on the Chelungpu fault associated with the 1999 Chi-Chi, Taiwan earthquake: Geophysical Research Letters, v. 33, L14306, doi:10.1029/2006GL026733.

Kuo, L.W., Li, H., Smith, S.A.F., Di Toro, G., Suppe, J., Song, S.-R., Nielsen, S., Sheu, H.-S., and Si, J., 2014, Gouge graphitization and dynamic fault weakening during the 2008 Mw 7.9 Wenchuan earthquake: Geology, v. 42, p. 47–50, doi:10.1130/G34862.1.

Li, H., et al., 2013, Characteristics of the fault-related rocks, fault zones and the principal slip zone in the Wenchuan Earthquake Fault Scientific Drilling Project Hole-1 (WFSD-1): Tectonophysics, v. 584, p. 23–42, doi:10.1016/j.tecto.2012.08.021.

Li, H., et al., 2014, Structural and physical properties characterization in the Wenchuan earthquake Fault Scientific Drilling project-hole 1 (WFSD-1): Tectonophysics, v. 619, p. 86–100, doi:10.1016/j.tecto.2013.08.022.

Si, J., Li, H., Kuo, L., Pei, J., Song, S., and Wang, H., 2014, Clay mineral anomalies in the Yingxiu-Beichuan fault zone from the WFSD-1 drilling core and its implication for the faulting mechanism during the 2008 Wenchuan earthquake (Mw 7.9): Tectonophysics, v. 619, p. 171–178, doi:10.1016/j.tecto.2013.09.022.

Tanaka, H., Chen, W.M., Wang, C.Y., Ma, K.F., Urata, N., Mori, J., and Ando, M., 2006, Frictional heat from faulting of the 1999 Chi-Chi, Taiwan earthquake: Geophysical Research Letters, v. 33, L16316, doi:10.1029/2006GL026673.

Tanaka, H., Chen, W.M., Kawabata, K., and Urata, N., 2007, Thermal properties across the Chelungpu fault zone and evaluations of positive thermal anomaly on the slip zones: Are these residuals of heat from faulting?: Geophysical Research Letters, v. 34, L01309, doi:10.1029/2006GL028153.

Tang, L., Luo, L., Lao, C., Wang, G., Wang, J., and Huang, Y., 2013, Real time fluid analysis during drilling of the Wenchuan Earthquake Fault Scientific Drilling Project and its responding features: Tectonophysics, v. 619, p. 70–78, doi:10.1016/j.tecto.2013.08.026.

Togo, T., Shimamoto, T., Ma, S., and Hirose, T., 2011a, High-velocity frictional behavior of Longmenshan fault gouge from Hongkou outcrop and its implications for dynamic weakening of fault during the 2008 Wenchuan earthquake: Earth Science, v. 24, p. 267–281, doi:10.1007/s11589-011-0790-6.

Togo, T., Shimamoto, T., Ma, S., Wen, X., and He, H., 2011b, Internal structure of Longmenshan fault zone at Hongkou outcrop, Sichuan, China, that caused the 2008 Wenchuan earthquake: Earth Science, v. 24, p. 249–265, doi:10.1007/s11589-011-0789-z.

Xue, L., et al., 2013, Continuous permeability measurements record healing inside the Wenchuan earthquake fault zone: Science, v. 340, p. 1555–1559, doi:10.1126/science.1237237.

Yao, L., Ma, S., Shimamoto, T., and Togo, T., 2013, Structures and high-velocity frictional properties of the Pingxi fault zone in the Longmenshan fault system, Sichuan, China, activated during the 2008 Wenchuan earthquake: Tectonophysics, v. 599, p. 135–156, doi:10.1016/j.tecto.2013.04.011.

Zhang, L., and He, C., 2013, Frictional properties of natural gouges from Longmenshan fault zone ruptured during the Wenchuan Mw7.9 earthquake: Tectonophysics, v. 594, p. 149–164, doi:10.1016/j.tecto.2013.03.030.

Appendix 2-A: Profile Alignment

The approximate depth of measurement was known from the pressure transducers on the logs and an independent measurement of water level in the well. Converting pressure to depth requires an estimate of the water density. Since the actual well water density is different from the pressure transducer manufacturer's default water density of 1.0281×10^3 kg/m^3, we made a correction for the water density by comparing the known winch vertical length and the record vertical depth of the pressure transducers of the three high-precision stop-go logs. The range of resulting densities is 1.0500-1.0533×10^3 kg/m^3, so we used the average value of 1.0515×10^3 kg/m^3 as the water density to correct the pressure transducer depths for all the profiles.

However, pressure accuracy (and occasional failure), uncertainty in water level and variations of well fluid density made an additional alignment procedure necessary. We therefore aligned the temperature profiles based on identifying short-wavelength features and gradient changes in the temperature profiles related to sharp contrasts in the gamma-ray logs and recovered cores (Figure 2-A1 and 2-A2). We initially aligned the profiles on the 394 m boundary and then checked the results by identifying features on the other known boundaries (Figure 2-A2). The consistency of the 589 m and 700 m features across the profiles is a useful check on the alignment procedure.

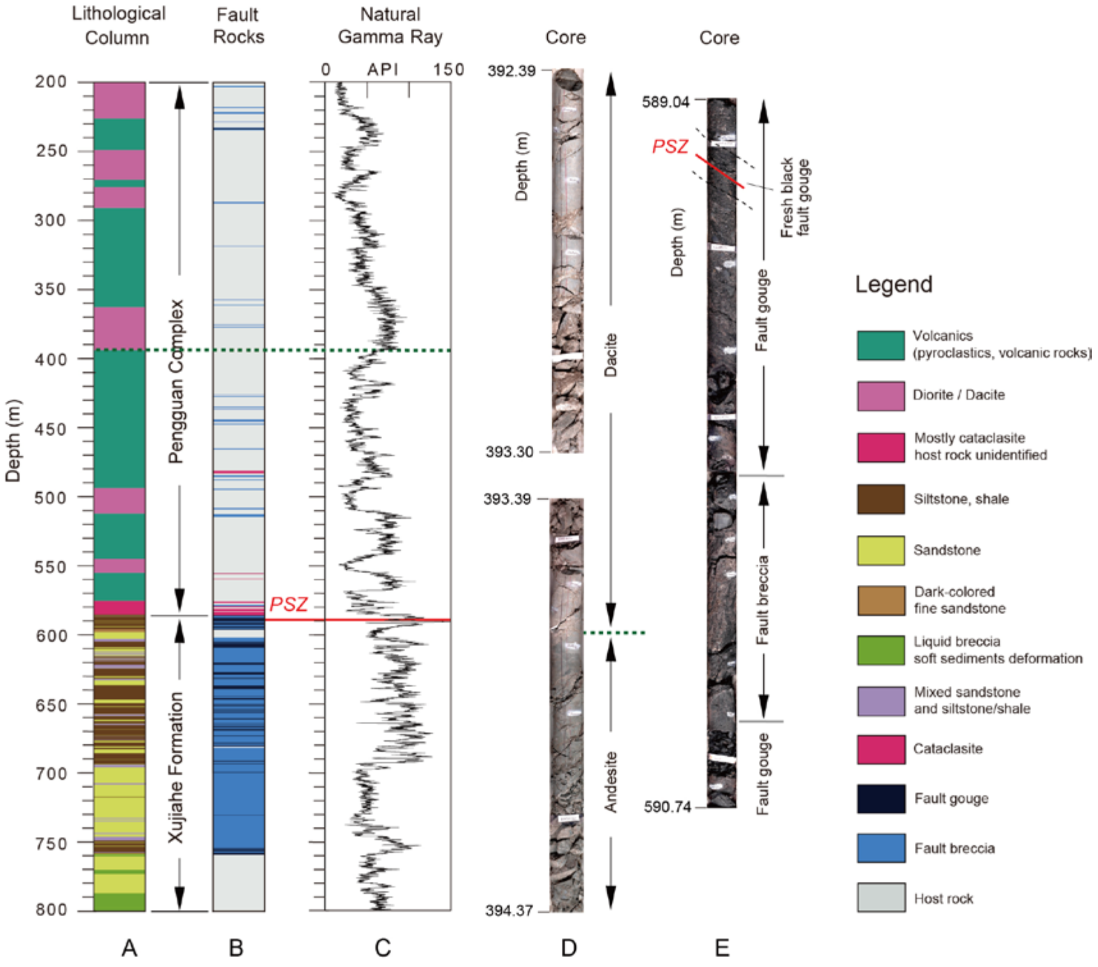

Figure 2-A1. Lithological column, logging and core images constraining two key contacts: the lithological contact between dacite and andesite at 394 m core depth, and the potential principal slip zone at 589 m core depth. The first contact 394 m is selected as one of the clearest sharp features in the logging and temperature data that is far from the fault zone. It therefore provides control on the alignment of the depth of the temperature logs.

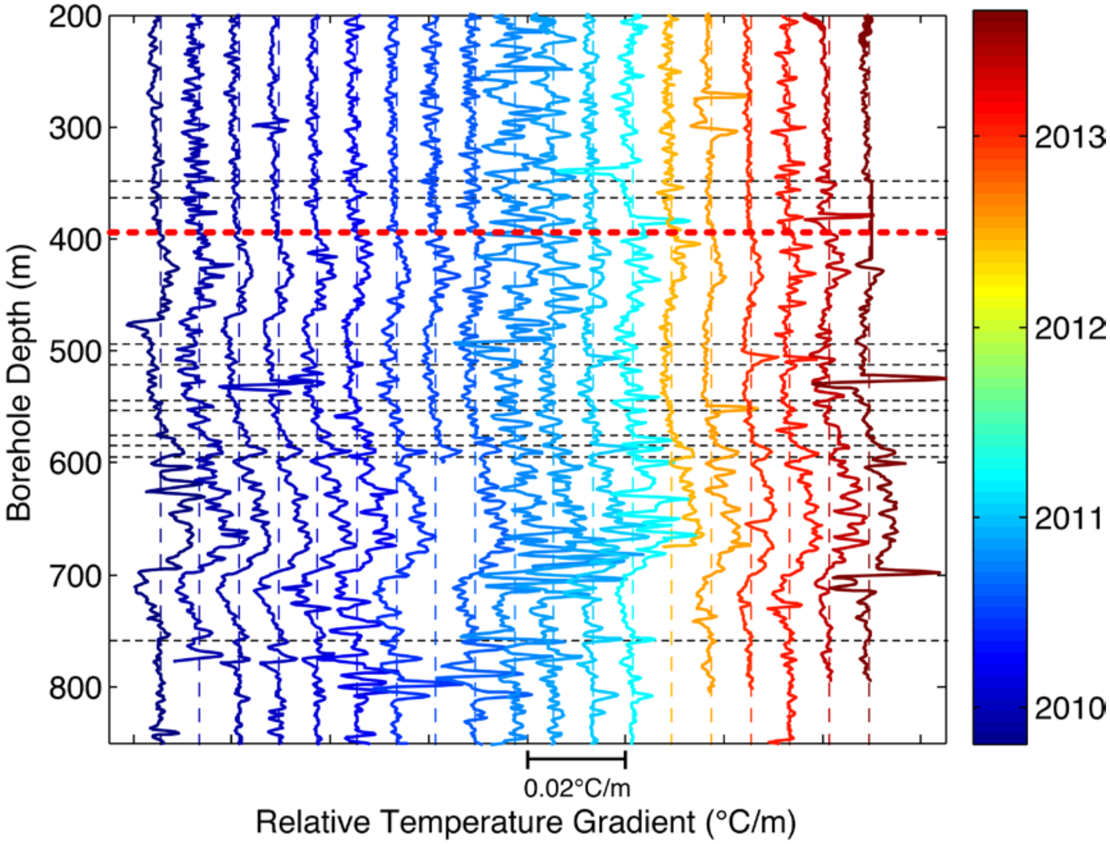

Figure 2-A2. Depth variation in temperature gradient for each temperature profile. Profiles are shifted along the x-axis to allow each profile to be seen individually. The high-frequency features are aligned on the known lithological boundary at 394 m using these differential temperature (gradient) profiles. Color scale indicates logging time and is identical to all other figures of the paper.

The individual profile temperature data is included as a matlab structure WFSD1TemperatureProfiles in the Appendix 2-A of this article. For each profile, the fields: raw vertical depth as measured by the pressure transducer (PressureTransducerDepth), vertical depth that includes corrections for water density and alignment (VerticalDepth), borehole depth that includes inclination correction (CorrectedDepth) and the starting date of the log (LoggingStartTime).

Appendix 2-B: Thermal Conductivity

Frictional heating on fault surfaces is manifested in temperature-depth profiles as small perturbations to the background thermal regime. Before interpreting perturbations as frictional heating it is important to remove other sources of perturbations. In borehole WFSD-1 a primary source of perturbations are caused by variations in thermal conductivity. The analysis that follows is a conservative approach in that we strive to minimize perturbations while honoring the data.

Thermal conductivity was measured on the WFSD-1 core at 121 locations by an optical scanning technique using an apparatus manufactured by Lippmann Geophysical Instruments [*Popov et al.*, 1999]. This apparatus has a reported accuracy of ±3% in the range between 0.2 and 25 W $m^{-1}K^{-1}$. This system uses a focused, continuous, and mobile heat source to heat the surface while an infrared temperature sensor lags behind at a constant interval and measures excess temperature. The determination of thermal conductivity values is based on the comparison of excess temperatures to that of reference samples with a known thermal conductivity [*Popov et al.*, 1999]. Sample preparation consisted of choosing samples that minimized surface roughness and painting that surface with a thin coat of nitrolacquer to counteract optical reflectivity. Within the fault zone where core surfaces were very rough samples were polished. Measurements were made under dry conditions with a scan rate of 5 mm/s. Thermal conductivity was measured at every 5 m between depths of 350 and 800m and was supplemented with denser, 1 m sampling between depths of 570 and 610 m (Figure 2-A3).

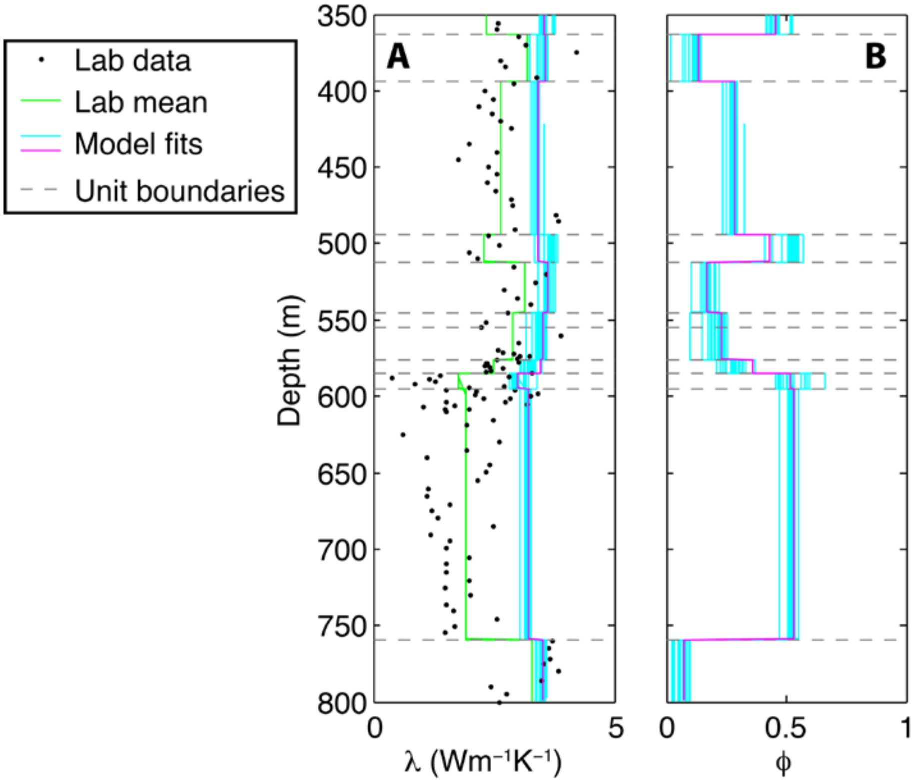

Figure 2-A3. Thermal conductivity (κ) and inferred porosity as a function of depth. (A) Dots indicate laboratory measurements of thermal conductivity on the recovered core. The lab mean is a thermal conductivity structure model that takes the mean of the lab measurements in each geological unit bounded by the dashed lines. For each profile, we invert a model fit conductivity structure (cyan lines) that is constrained to have a constant heat flow over all the units with the observed gradients while minimizing the difference between the model fit and the maximum of the thermal conductivity in each unit. Magenta line distinguishes one model fit so fine-structure can be examined. (Magenta is 30 December, 2012 stop-go profile). (B) Porosity computed with Eq. 2-B2 for the model fits in (A).

Measured dry values of thermal conductivity vary between approximately 1 and 4 $Wm^{-1}K^{-1}$ (Figure 2-A3) and have been have been sorted on the basis of their lithology [*Li et al.*, 2013]. These values generally agree with values reported in the literature [e.g., *Kappelmeyer and Haenal*, 1974]. Typical values of volcaniclastics and diorite are reported to be 2.2 and 3.5 W/m/K. The interbedded sandstones and dark fine sandstones show the largest variation with values between 1 and 4 W/m/K. The massive sandstones show relatively low values between 1.5 and 2.5 W/m/K, and the fault zone rocks also characterized as mixed sandstone. The low values of the sandstone likely reflect a systematic bias due to higher porosities because thermal conductivities were measured under dry conditions whereas the in-situ condition is saturated.

We derive an estimate of thermal conductivity values for saturated conditions as follows. We divide thermal conductivity values into lithological units by following Li *et al.* [2013] and note discontinuities in measured thermal conductivity values from laboratory analysis of the core. Maximum and mean core thermal conductivity values for each unit are reported in Table 2-A1 and Figure 2-A3. The maximum value for each unit is assumed to represent samples with the lowest porosity (i.e., closest to a matrix value) and therefore is closest to in-situ thermal conductivity. We then determine the value of heat flow over the interval 350 to 800 m that minimizes the difference between the maximum laboratory measurement of conductivity and the inferred value that linearizes the observed thermal gradient. This procedure ascribes differences between the mean and maximum value of thermal conductivity to the porosity while also minimizing the inferred porosity. Thermal gradients for each unit are estimated by fitting the top and bottom 5 temperature measurements for the unit instead of a least-squares fit of all the data. This procedure is better at preserving any internal temperature features within the unit as seen in the anomaly centered over ~700 m depth. The resultant values of heat flow for the different logs range from 69 to 72 mW/m^2, which is consistent with regional heat flow at this site on the margin of the Tibetan plateau and the Sichuan basin [*Xu et al.*, 2011]. Based on the inferred heat flow and the measured gradients, we solve for the conductivity in each unit (Figure 2-A3).

As a check on this procedure, we also calculate the porosity assuming that the current measurements are completely dry and the inferred in-situ values are saturated, i.e., if the bulk field thermal conductivity is

$$\sqrt{\lambda_B} = \phi\sqrt{\lambda_w} + (1-\phi)\sqrt{\lambda_m} \qquad \text{(2-B1),}$$

where λ_B is the bulk thermal conductivity, ϕ is the porosity, λ_w is the thermal conductivity of water and λ_m is the matrix thermal conductivity [*Beardsmore and Cull*, 2001].

In the laboratory measurements, the air-filled pore space has negligible thermal conductivity and therefore

$$\sqrt{\lambda_B} = \phi\sqrt{\lambda_w} + \frac{(1-\phi)}{1-\phi_{lab}}\sqrt{\lambda_{lab}} \qquad \text{(2-B2),}$$

where λ_{lab} is the measured thermal conductivity in the laboratory and ϕ_{lab} is the laboratory porosity. We assume that the change of porosity with confining pressure is sufficiently small that $\frac{1-\phi}{1-\phi_{lab}}$ is approximately 1. This approximation is adequate for the moderate effective pressures (<10 MPa) in this borehole. For instance, in compaction experiments of Chen *et al.* [2013] on Wenchuan fault zone gouge from an exposed outcrop, the predicted porosity changes at 10 MPa is <1%. We solve for the porosity ϕ for each profile by assuming λ_B is the fit value for the unit from the optimization procedure described above, λ_{lab} is the mean laboratory-derived value of the unit, and thermal conductivity of water is 0.6 $\mathrm{Wm^{-1}K^{-1}}$.

The inferred thermal conductivity structure and porosity is shown in Figure 2-A3 for each profile. As can be seen, the porosity is always positive, as required physically, and is highest in the sandstone units where high porosity is expected, and has generally reasonable values at all depths. The results are consistent across all profiles suggesting that the procedure is robust.

Once the conductivity structure is determined, we use the Bullard [1939] method to extract anomalous temperatures relative to the background conductive geotherm. In this method the predicted temperature *T(z)*, at depth, *z*, may be expressed as,

$$T(z) = T_0 + q_0 \sum_{i=1}^{N} \frac{\Delta Z_i}{k(z)_i} \tag{2-B3}$$

where $k(z)_i$ is the thermal conductivity measured over the i^{th} interval Δz_i, and the summation is performed over N intervals that span the depth of interest. The parameters q_o and T_o are estimated by plotting $T(z)$ against summed thermal resistance $\sum \Delta z_i / k(z)_i$ Anomalous temperatures are computed as the difference between the observed and predicted background temperatures.

Alternative unit layer structure

This procedure to identify thermal anomalies is sensitive to the layer boundaries inferred from the logging and core data. It is notable that the two largest anomalies in Figure 2-3 occur in areas where no lithological boundaries were inferred. We therefore repeated the analysis with an additional layer boundary in the middle of the largest anomaly to test the sensitivity of the results to the structure.

Figure 2-A4 and Figure 2-A5 are analogous to main text Figure 2-3 and Figure 2-A3 with an additional boundary at 693 m. This depth has a prominent change in the gamma ray log variability and individual fault gouges are closely spaced above this level. However, the host rock is the same on both side of 693 and the mean value of laboratory measurements of thermal conductivity does not show any strong discontinuity here therefore we did not include the boundary in our preferred model.

The anomalous temperature at 700 m is greatly reduced by the additional boundary for all profiles and therefore the maximum bound on the coseismic dissipated heat energy is lower for this model. In addition, a smaller, negative anomaly above the 693 boundary decays with time. The decay is consistent with the gradient increasing as the borehole re-equilibrates from the drilling perturbation. The inferred porosities for this model exceed 80% in the layer below 693 m, which is likely an unphysical value.

We infer that the fundamental conclusions of this paper are unchanged by the existence of a 693 m boundary. A conductively diffusing, positive heat anomaly is still not observed and the dissipated thermal energy is still significantly below the upper bound in the main text (29 MJ/m^2). We also infer that a thermal conductivity boundary at 693 m is unlikely based on the laboratory thermal conductivity measurements and the high requisite porosity.

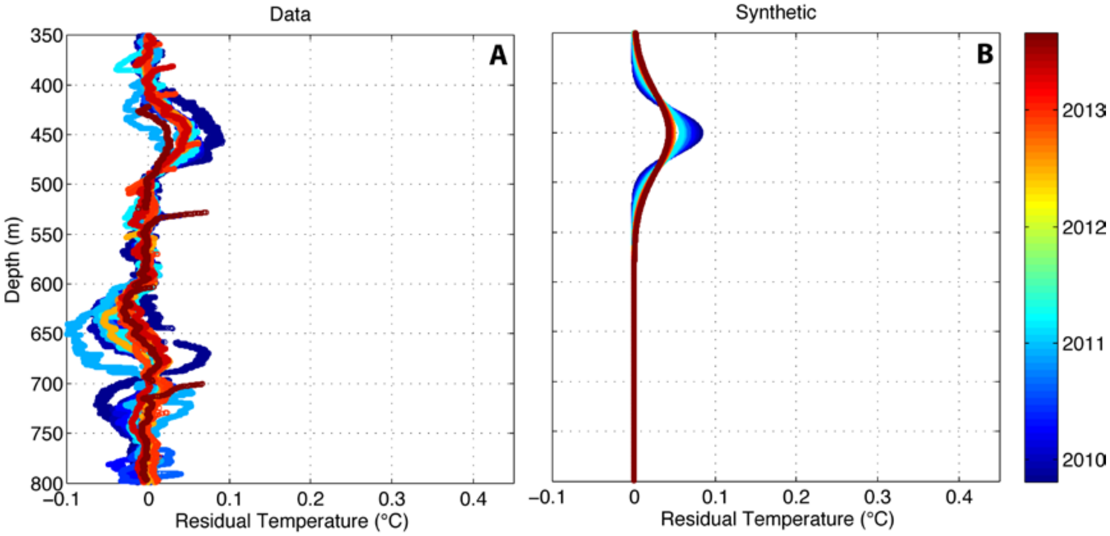

Figure 2-A4. Residual (anomalous) temperature after the conductive geotherm is removed for the alternative model with an extra unit boundary at 693 m depth (a) Observed residual temperature for each profile color-coded by date. The thermal conductivity is as in Figure 2-A5. (b) Modeled residual temperature for frictional dissipation on 450 m surfaces with the total dissipated energy constrained to be equal to the observed residual thermal energy (See Appendix text). The frictionally dissipated energy is transported from the fault zone by diffusion. For this alternative thermal model, no positive temperature anomaly is observed at 700 m depth, therefore no frictional heat was modeled there.

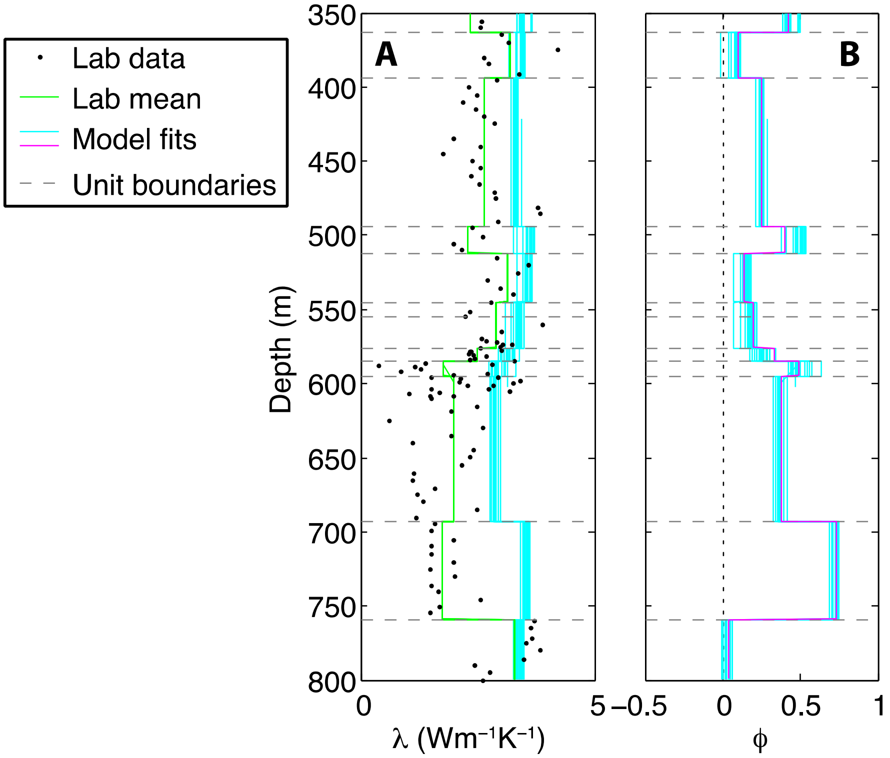

Figure 2-A5. Thermal conductivity (κ) and inferred porosity as a function of depth for the alternative model with an extra unit boundary at 693 m depth. (A) Dots indicate laboratory measurements of thermal conductivity on the recovered core. The lab mean is a thermal conductivity structure model that takes the mean of the lab measurements in each geological unit bounded by the dashed lines. For each profile, we invert a model fit conductivity structure (cyan lines) that is constrained to have a constant heat flow over all the units with the observed gradients while minimizing the difference between the model fit and the maximum of the thermal conductivity in each unit. Magenta line distinguishes one model fit so fine-structure can be examined. (Magenta is 30 December, 2012 stop-go profile). (B) Porosity computed with Eq. 2-B2 for the model fits in (A).

Appendix 2-C: Frictional Heat Model

We model the residual temperature due to the dissipation of frictional energy *S* on a plane as a plane source of heat diffusing into a layered medium with the conductivity structure as determined from the Bullard plot inversion (Figure 2-A3). We use a 1-D finite difference calculation to diffuse the heat from the fault plane into the surrounding layers, which are assumed to be parallel to the fault and inclined at an angle of 45^o to the borehole (The fault dips 55^o and the borehole is incline 10^o). The initial conditions of the calculation are set using the analytical solution in a homogeneous medium at time Δt after the earthquake where Δt is the timestep of the rest of the calculation. For the results presented here Δt=1250 s.

$$\Delta T_{EQ}(\hat{z},t) = \frac{S}{2\sqrt{\pi\alpha_0\Delta t}} e^{-(\hat{z}-\hat{z}_f)^2/4\alpha_0\Delta t} \tag{2-C1}$$

where S is the dissipated energy on the fault plane z_f, z is the coordinate direction normal to the plane, and α_0 is the thermal diffusivity closest to the fault. After the first time step, the full thermal conductivity structure as constrained by the constant heat flow inversion is employed. For simplicity, we select the thermal conductivity structure inverted from one of the best resolved profiles, which is from Dec. 30, 2012. As can be seen from Figure 2-A3, the inverted structure is substantially similar for all the profiles.

For the full suite of inverted profiles, S_{450}=5 +/- 2 MJ/m^2 and S_{690}=24+/-6 MJ/m^2. These two anomalies are superposed in Figure 2-3b.

Appendix 2-D: The Drilling Anomaly

The observed temperature gradient steepens with time (Figure 2-1). This steepening is expected for the recovery of the borehole from the drilling anomaly. Drilling itself significantly perturbs the geotherm. Standard drilling procedure is to circulate mud continuously in the borehole at a constant temperature at a rate of about 0.1 m^3/min. This constant circulation is designed to maintain borehole pressure, circulate out drill cuttings and advect away the frictional heat generated by the drill bit [*Lachenbruch and Brewer*, 1959]. Therefore, the drilling effect is well-modeled by an isothermal line source of duration equal to the drilling time [*Fulton et al.*, 2010; *Lachenbruch and Brewer*, 1959; *Bullard*, 1947; *Jaeger*, 1961; *Herzen and Scott*, 1991].

The drilling team did not record the mud temperature in WFSD-1, but the range of mud temperatures directly recorded in the nearby WFSD-2 is 21-26.6^o. (WFSD-2 is not suitable for fault zone temperature measurements because of its complex and prolonged drilling history). We assume that a similar range was used by in WFSD-1 and calculate the drilling anomaly at the 589 m fault where we are studying the smallest feature.

For a conductively cooling system, the line source imposes a cylindrical symmetry that results in a faster decay than the planar source of the fault heating anomaly. Specifically, the temperature anomaly from drilling at time t since the beginning of drilling at a particular depth is

$$T / T_0 = \log(1 + t_1 / (t - t_1)) / (\log(4\kappa t / a^2) - 0.577) \qquad \text{(2-D1)}$$

where T_0 is the difference between drilling mud temperature and the original temperature at a particular depth, κ is the thermal diffusivity, t_1 is the duration of drilling at that depth, and a is the wellbore radius [*Bullard*, 1947, Eq. I]. Eq. 2-D1 is used with the drilling history to calculate the positive temperature anomaly associated with the range of possible fluid temperatures. The range of positive drilling anomalies possible at the 589 fault is shown by the gray shaded area in Figure 2-A6.

In contrast, the conductive temperature decay of a planar fault is

$$T = (\mu \sigma_n d / c_p) / (2(\pi \kappa t)^{1/2}) \qquad \text{(2-D2)}$$

where, μ is the coefficient of friction, σ_n is the effective normal stress, d is the slip, c_p is the specific heat capacity and κ is the thermal diffusivity [*Carslaw and Jaeger*, 1959]. For typical values of these parameters, there is expected to be a cross-over time at which the fault heating dominates over the drilling anomaly (Figure 2-A6). Therefore, a fault zone heating signal can potentially be significant after the drilling anomaly decays.

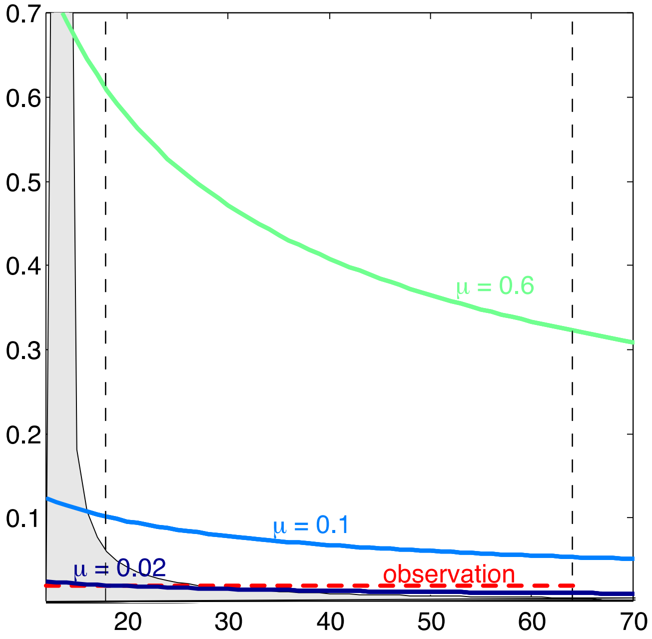

Figure 2-A6. Predicted maximum amplitude of the temperature anomaly for the fault in the WFSD-1 borehole with representative effective co-seismic coefficients of friction. Dashed lines show the first and last measurement time and the maximum temperature anomaly at the fault crossing is shown by the red dashed line. Temperature curves are computed from the planar fault model in Equation 2 of the main text with σn = 9 MPa, cp = 800 J/kg [Beardsmore and Cull, 2001], ρ=2500 kg/m3 (Li et al., 2014), d = 7 m, and κ=1.5 × 10 -6m2/s. A simplified model for the normal stress as equal to the lithostatic overburden less the hydrostatic pore pressure is used in lieu of independent constraints on the deviatoric stress on this reverse fault. Although this simplification introduces less error than the uncertainty on slip, it is important to bear in mind when comparing this apparent friction here to any other data set. Grey region shows the predicted drilling anomaly at 589 m depth for a range of drilling mud temperatures up to a 26.6oC. Flat top of this region indicates time drilling.

Appendix 2-E: Temperature Increase

The geologically significant 589 m depth fault has a subtle temperature increase. However, the width of a frictionally generated anomaly is predicted to be much greater than observed. For a homogeneous medium with a thermal diffusivity of 1.5 ×

10^{-6} m^2/s and heat generation at the time of the earthquake, the anomaly is expected to be ~100 m wide at the time of measurement, which is not observed (Figure 2-2B). Furthermore, the signal does not decay or widen (Figure 2-A7).

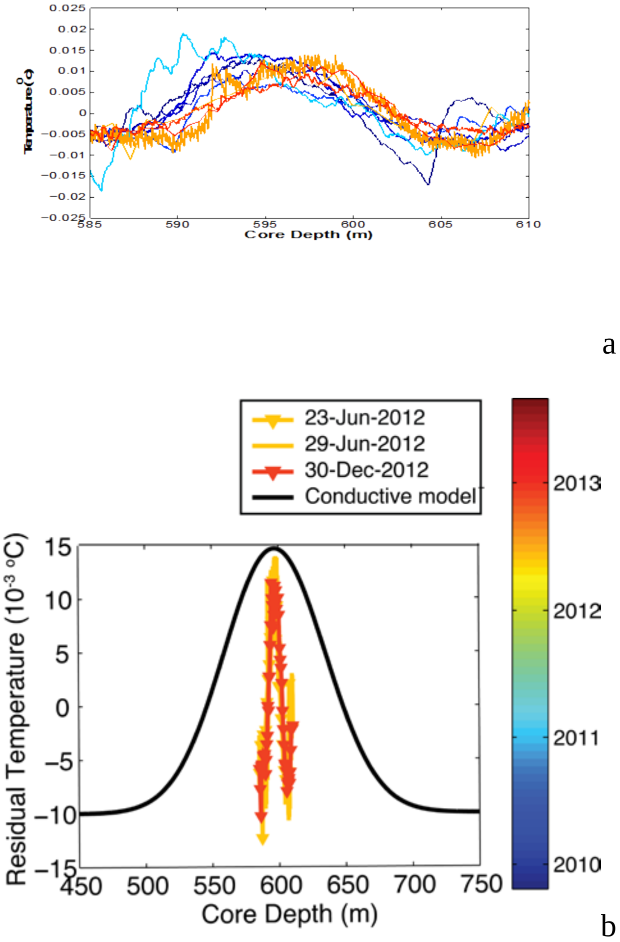

Figure 2-A7. View of the 590 m fault zone anomaly (a) Close-up of fault zone anomaly for the least noisy records. Colors correspond to dates as in the color bar in Figure 2-A2. (b) Comparison of anomaly and a calculated frictional anomaly with shear stress set to match observed amplitude and diffusion time equal to the time between the earthquake and the observation. Note that the calculated diffusive anomaly is wider than observed.

Table 2-A1. Thermal conductivity structure. Unit boundaries determined from *Li et al.*, [2013] and Li. *et al.* [2014]. The alternative interpretation in Figs. (2-A4)- (2-A5) has an additional boundary at 693 m depth that separates the highly faulted sandstone from the lower, more homogeneous unit. Model fit is the mean of the fits for all of the profiles for the given unit.

Lithology	**Top (m)**	**Bottom (m)**	**Mean λ_{lab} (W/m/k)**	**Max λ_{lab} (W/m/k)**	**Mean Fit λ_{lab}(W/m/k)**
Volcanic	349	363	2.34	2.58	3.5
Diorite	363	394	3.19	4.21	3.45
Volcanic	394	494	2.65	3.83	3.33
Diorite	494	512	2.29	2.62	3.57
Volcanic	512	545	3.14	3.58	3.58
Diorite	545	555	2.56	2.79	3.42
Volcanic	555	576	2.96	3.90	3.36
Cataclasite	576	585	2.50	3.02	3.18
Fault breccia	585	595	1.76	3.29	3.95
Siltstone	595	759	1.91	3.40	3.13
Sandstone	759	800	3.30	3.84	3.41

References

Beardsmore, G.R., and Cull, J.P., 2001, Crustal heat flow: a guide to measurement and modelling. Cambridge,UK: Cambridge Univ. Press.

Bullard, E. C., 1939, Heat Flow in South Africa. *Proceedings of the Royal Society a: Mathematical, Physical and Engineering Sciences,* 173(955), 474–502. doi:10.1098/rspa.1939.0159

Bullard, E., 1947, The time necessary for a bore hole to attain temperature equilibrium： Geophysical Journal International, v. 5, p. 127–130, doi:10.1111/j.1365-246X.1947.tb00348.x.

Carslaw, H. S., and Jaeger, J. C., 1959, Conduction of heat in solids. -1, (Oxford: Clarendon Press, 1959, 2nd ed., 1959).

Chen, J., Yang, X., Yao, L., Ma, S. & Shimamoto, T. Frictional and transport properties of the 2008 Wenchuan Earthquake fault zone: Implications for coseismic slip-weakening mechanisms. *Tectonophysics* **603,** 237–256 (2013)

Fulton, P. M., Harris, R. N., Saffer, D. M., and Brodsky, E. E., 2010, Does hydrologic circulation mask frictional heat on faults after large earthquakes? : Journal of Geophysical Research, v. 115, B09402, doi:10.1029/2009JB007103.

Herzen, von, R., and Scott, J., 1991, Thermal Modeling for Hole 735B1: Proceedings of the Ocean Drilling Program: Scientific Results, v. 118, p. 349–356.

Jaeger, J., 1961, The effect of the drilling fluid on temperatures measured in bore holes: Journal of Geophysical Research, v. 66, p. 563–569, doi: 10.1029/JZ066i002p00563.

Kappelmeyer, O. and R. Haenel, 1974, *Geothermics with special reference to application*, Berlin: Gebrueder Borntraeger (Geoexploration Monographs. Series 1, No. 4).

Lachenbruch, A., and Brewer, M., 1959, Dissipation of the temperature effect of drilling a well in Arctic Alaska: United States Geological Survey Bulletin, v. 1083, p. 73–109.

Li, H., and 11 others, 2013, Characteristics of the fault-related rocks, fault zones and the principal slip zone in the Wenchuan Earthquake Fault Scientific Drilling Project Hole-1 (WFSD-1): Tectonophysics, v. 584, p. 23-42, doi:10.1016/j.tecto.2012.08.021

Li, H., and 11 others, 2014, Structural and physical properties characterization in the Wenchuan earthquake Fault Scientific Drilling project-hole 1 (WFSD-1): Tectonophysics, v. 619, p. 86-100, doi:10.1016/j.tecto.2013.08.022.

Melosh, H. J., 1979, Acoustic Fluidization - New Geologic Process: Journal of Geophysical Research, v. 84, p. 7513–7520, doi:10.1029/JB084iB13p07513.

Popov, Y.A., Pribnow, D.F.C., Sass, J.H., Williams, C.F., and Burkhardt H., 1999, Characterization of rock thermal conductivity by high-resolution optical scanning, Geothermics, v. 28, p. 253–276.

Xu, M., Zhu, C.Q., Tian, Y.T., Song, Rao, S., and Hu, S.B., 2011, Borehole temperature logging and characteristics of subsurface temperature in the Sichuan Basin: Chinese Journal of Geophysics, v. 54, p. 224–233, doi:10.1002/cjg2.1604.

Chapter 3. Continuous Permeability Measurements Record Healing inside the Wenchuan Earthquake Fault Zone

Lian Xue[1,2*], Hai-Bing Li[2], Emily E. Brodsky[1], Zhi-Qing Xu[2], Yasuyuki Kano[3], Huan Wang[2], James J. Mori[3], Jia-Liang Si[2], Jun-Ling Pei[4], Wei Zhang[5,2], Guang Yang[2], Zhi-Ming Sun[4], Yao Huang[6]

[1]Dept. of Earth and Planetary Sciences, University of California, Santa Cruz, USA.

[2] State Key Laboratory of Continental Tectonic and Dynamics, Institute of Geology, Chinese Academy of Geological Sciences, Beijing, China.

[3]Disaster Prevention Research Institute, Kyoto University, Japan.

[4]Institute of Geomechanics, Chinese Academy of Geological Sciences, Beijing, China.

[5]Shandong Provincial Lunan Geo-engineering Exploration Institute, Yanzhou, Shandong, China.

[6]No.6 brigade of Jiangsu Geology & Mineral Resources Bureau, Lianyungang, Jiangsu, China.

*This paper is published as Xue, Lian, Hai-Bing Li, Emily E. Brodsky, Zhi-Qing Xu, Yasuyuki Kano, Huan Wang, James J. Mori et al. "Continuous permeability measurements record healing inside the Wenchuan earthquake fault zone." Science 340, no. 6140 (2013): 1555-1559.

Abstract:

Permeability controls fluid flow in fault zones and is a proxy for rock damage following an earthquake. We used the tidal response of water level in a deep borehole to track permeability for 18 months in the damage zone of the causative fault of the 2008 M_W 7.9 Wenchuan earthquake. The unusually high measured hydraulic diffusivity of 2.4×10^{-2} m^2/s implies a major role for water circulation in the fault zone. For most of the observation period, the permeability decreases rapidly as the fault heals. The trend is interrupted by abrupt permeability increases attributable to shaking from remote earthquakes. These direct measurements of the fault zone reveal a process of punctuated recovery as healing and damage interact in the aftermath of a major earthquake.

3-1 Introduction

The initiation and propagation of earthquakes depend critically on the hydrogeologic properties of the fault zone, including the fracture-dominated damage zone [*Andrews*, 2002; *Caine et al.*, 1996; *Hubbert and Rubey*, 1959; *Marone and Saffer*, 2007; *Rempel and Rice*, 2006; *Rice*, 2006]. Fault zone permeability serves as a proxy for fracturing and healing as the fault regains strength during one of the most unconstrained phases of the earthquake cycle [*Gratier*, 2011]. In addition, permeability and storage help govern the pore pressure and effective stress on a fault. Because earthquakes generate fractures in a damage zone around a fault, it is reasonable to expect that following a large earthquake, the fault zone permeability transiently increases. Over time, the permeability may decrease as a result of a combination of chemical and mechanical processes [*Gratier*, 2011]. However, measuring in situ fault zone hydrogeologic properties requires post-earthquake rapid response drilling, and appropriate data have not previously been recorded continuously immediately after a large earthquake.

The devastating M_W 7.9 Wenchuan earthquake occurred on May 12, 2008 and was the largest seismic event in China in the past 50 years. Shortly afterward, the Wenchuan earthquake Fault Science Drilling Program (WFSD) constructed a series of boreholes penetrating the main rupture zone. This study will investigate the healing process after the Wenchuan Earthquake by utilizing the continuously water level observations 1.5-3 yr after the major earthquake.

3-2 Hydrological Observations

The first borehole (WSFD-1) (31.1ºN, 103.7ºE) is 1201 m deep and nearly vertical, in a locale with 6 m of vertical displacement at the surface [*H Li et al.*, 2013]. The borehole that is open to fluid flow in the formation below 800 m (Figure 3-1), provides a unique opportunity to directly measure fault zone permeability over time. The borehole intersects the likely principal slip zone at a depth of 590 m, which is a major lithological boundary between the up-thrust Pre-Cambrian Pengguan granitic and volcanic complex and the underlying Triassic sediments [*H Li et al.*, 2013; *Xu et al.*, 2008]. The fault breccia extends to 760 m, and the fracture density remains high to the bottom of the borehole [*H Li et al.*, 2013]. Mature faults have damage zones extending at least ~100 m from the edge of the fault core [*Savage and Brodsky*, 2011]. Therefore, the damage zone of this site is expected to extend into the open interval beginning at 800 m.

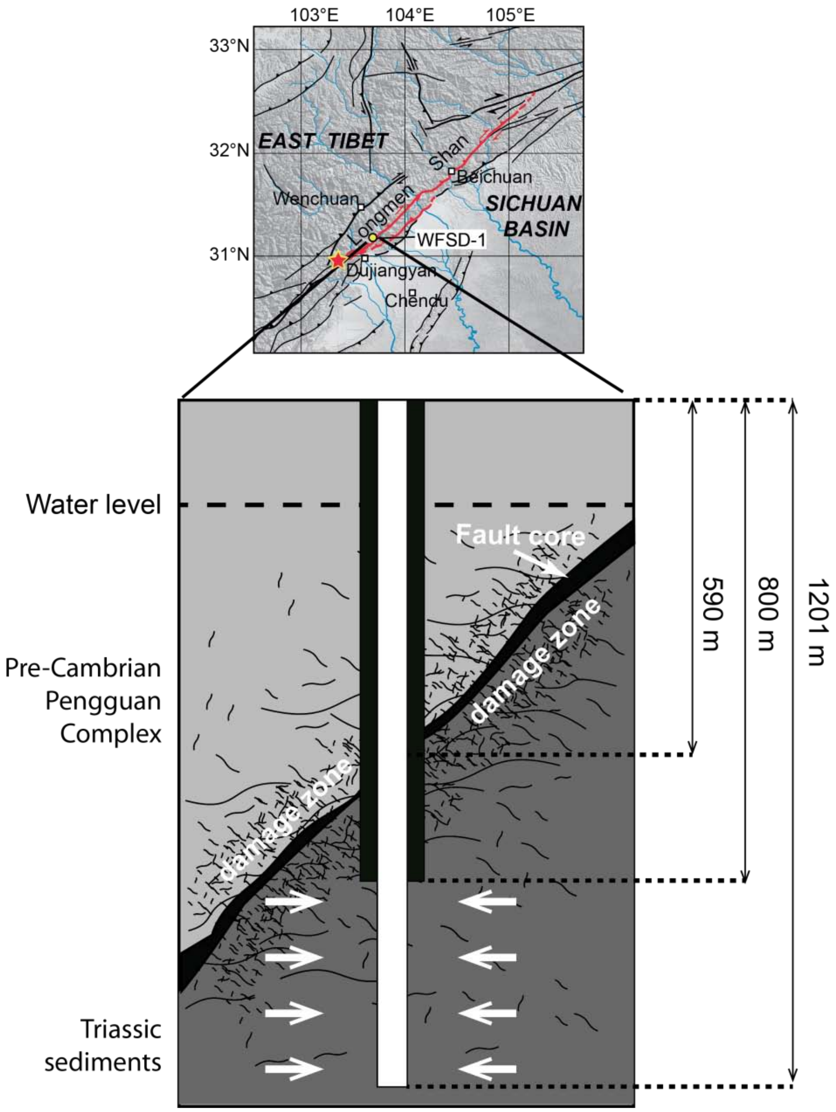

Figure 3-1. Location and sketch of the WFSD-1 site. Red lines in the inset indicate the main rupture zone, and the red star is the epicenter of the Wenchuan earthquake. In the sketch, the black line is the fault core which is surrounded by the damage zone. The borehole is 1201m deep and 800-1201m is the open interval where water can flow into the hole from the formation (white arrows). The fault that was most likely active during the Wenchuan earthquake is the major lithological boundary between the pre-Cambrian Pengguan complex and the Triassic sediments at 590 m.

We measured the water level response to tidal forcing in WFSD-1 to constrain the average hydrogeologic properties of the damage zone between 800 and 1200 m below the ground surface (~200-600 m below the principal slip zone [*H Li et al.*, 2013; *Xu et al.*, 2008]). We used these measurements to infer the hydraulic diffusivity and permeability variations inside the Wenchuan earthquake fault zone from Jan. 1, 2010 to Aug. 6, 2011. The WFSD-1 pressure transducer recorded data with a 2 minute sampling rate and 6 mm resolution (Figure 3-2). Data gaps occur every month or two as the instruments were removed from the well to retrieve the data and measure temperature profiles. The raw records show clear tidal oscillations superimposed on the long-term recharge trend (Figure 3-2).

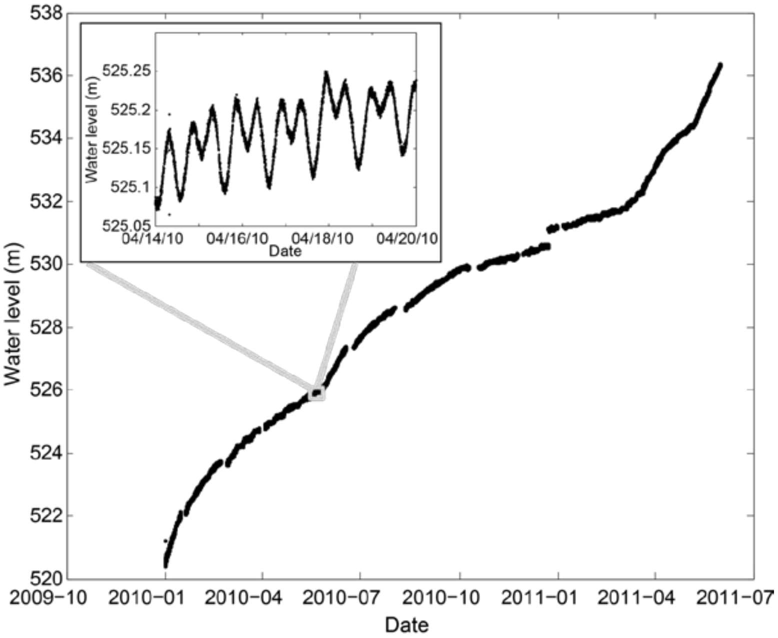

Figure 3-2. Water levels from WFSD-1 recorded from Jan. 1, 2010 to Aug. 6, 2011. The oscillations in the inset are generated by the Earth tides. The precision of the water level measurement is 6 mm. Water level is assumed to be continuous across the data gaps.

3-3 Method

The tidal oscillations serve as probes of the fault hydrogeologic properties. The tidal forcing imposes a dilatational strain on the surrounding rock formation that pumps water cyclically in and out of the well through the rock around the uncased portion of the borehole below 800 m depth. The clear oscillations indicate the aquifer is well-confined. The transmissivity and storage* coefficient determine the phase and amplitude response of the water level to the tidal loading [*Freeze and Cherry*, 1977]. Transmissivity is a measure of the rate of volumetric flow through a unit width of aquifer under a unit hydraulic gradient and is directly proportional to permeability. Storage coefficient is the volume of water released from storage per unit surface area of aquifer per unit imposed head. To a first order, phase lag is inversely related to transmissivity, and amplitude response is proportional to storage coefficient. Using the tidal response to measure hydrogeologic properties has two distinct advantages. Firstly, the tidal response is passive and records the in situ properties undisturbed by repeated pump tests or water injections. In addition, the tidal response provides a continuous record of temporal changes of hydrogeologic properties in the rocks below the main rupture zone.

3-3.1 Bayesian inversion analysis in the time domain

We use a Bayesian Monte Carlo Markov Chain inversion method [*Gill*, 2002] in the time domain to measure the phase and amplitude responses of water level for the largest semidiurnal Earth tide constituent M2, and the corresponding errors. As a check, we also calculate the Earth tidal responses directly from spectral division in the frequency domain [*Elkhoury et al.*, 2006]. The frequency domain results are identical to the maximum likelihood results of the Bayesian inversion.

In the time domain, the water level record is expressed as:

$$w(t_j) = \sum_{k=1}^{N} a_k \cos(\omega_k t_j + \zeta_k) + e_j \tag{3-1}$$

where t_j is the time of data point j, N is the number of tidal constituents used in the analysis, ω_k is the angular frequency of the kth tidal constituent, a_k is the amplitude of the kth constituent in the water level record, ς_k is the phase angle of the kth constituent in the water level records, and e_j is the residual of data point j in the water level records.

Similarly, the theoretical dilatation strain data imposed by tides, which includes both solid Earth tides and ocean tides, is expressed as:

$$\varepsilon_V(t_j) = \sum_{k=1}^{N} A_k \cos(\omega_k t_j + \theta_k) + E_j \tag{3-2}$$

where $\varepsilon_V(t_j)$ is the theoretical dilatation strain data at time t_j, and A_k, θ_k, and E_j take on analogous roles as a_k, ς_k and $e_{j.}$

First, we use a band-pass filter of 0.8 to 2.2 cycles/day to eliminate the long-term trend of the water level, and to reduce high frequency noise. The yielded records contain the semidiurnal and diurnal tidal components as well as the noise in this tidal band. We use four tidal constituents, O1, K1, M2 and S2, in the time domain analysis (Table 3-1 for angular frequencies). The synthetic dilatational strain data is generated by the theoretical tidal code SPOTL v.3.3.0 combined with ertid [*Agnew*, 2012]. These programs include both the solid Earth and ocean-loading tides. As a check, we used a local instrument to measure the tides at this site, and find there is no phase shift between theoretical tides and observed tides. The water level and dilatation records are each divided into 29.6-day segments with 80% overlap. The time window is long enough to discriminate semidiurnal S2, M2 constituents, and diurnal O1, K1 constituents. For segments which include data gaps, both the theoretical and observation data are set to zero during the data gap. This masking procedure ensures a consistent treatment of missing data. If the gap comprises more than 20% of the segment, no further analysis is attempted for the segment.

The Bayesian Markov chain Monte Carlo (MCMC) [Gill, 2002] inversion approach is applied to each segment for both water level and dilatation strain records to calculate the amplitude response and phase shift of water level relative to the theoretical tidal dilatation strain. For each segment, a 5×10^6 sample Markov chain is generated and then decimated by 120 (the correlation length) to generate a distribution of inverted phase and amplitude responses. The resulting 4×10^4 samples are used to estimate the mean value of the phase and amplitude response, and the corresponding 95% confidence interval. The mean range of the phase confidence interval is 0.3°, which corresponds to 0.7 minutes for the M2 tidal period. The precision is reasonable as the data has a 2 minute sampling interval and < 30s clock error.

3-3.2 Hydrogeologic properties estimation

Since the inclination [*Li et al.*, 2013] of WSFD-1 from vertical is small (~10°-13°), we model the WSFD-1 hole as a vertical borehole. The observable quantities are the amplitude response *A*, which is the ratio between the amplitude of Earth tidal dilatation strain and that of water level oscillations, and the phase response η, which is the phase shift of the water level oscillations relative to the imposed dilatation strain. Assuming a two-dimensional isotropic, homogenous and laterally extensive aquifer, for the long periods of tidal oscillations,

$$A = (E^2 + F^2)^{\frac{1}{2}} \tag{3-3}$$

and

$$\eta = -\tan^{-1}(F / E) \tag{3-4}$$

where $E \approx 1 - \frac{\omega r_c^2}{2T} Kei(\alpha), F \approx \frac{\omega r_c^2}{2T} Ker(\alpha), \alpha = (\frac{\omega S}{T})^{\frac{1}{2}} r_w$, T is the transmissivity, S is the storage coefficient, *Ker* and *Kei* is the zeroth-order Kelvin Functions, r_w is the radius of the well, r_c is the inner radius of the casing, and ω is the angle frequency of tides [*Hsieh et al.*, 1987]. In our study, the measured r_c is 0.08 m and the r_w is 0.09 m. Since A, η, ω, r_c and r_w are all measured values, T and S can be calculated by solving equations (3-3) and (3-4). The 95% confidence intervals of permeability are estimated by propagating the phase confidence intervals through the permeability inversion (Eqs. 3-3 and 3-4).

3-4 Results

3-4.1 Tidal Response

We translate the phase and amplitude responses to transmissivity and storage coefficient based on the analytical solution for a two-dimensional isotropic, homogenous and laterally extensive aquifer [*Hsieh et al.*, 1987]. The observed phase lag ranges from - 20º to - 30º, where negative signs indicate that the water level oscillations lag behind the imposed dilatational strain, and the amplitude response ranges from 5.5×10^{-7}- 6.3×10^{-7} m^{-1} (Figure 3-3).

3-4.2 Hydrogeologic Properties

The corresponding transmissivity T varies systematically over a range of 3.6×10^{-6} to 6.8×10^{-6} m^2/s with an average value of 5.1×10^{-6} m^2/s (Figure 3-4). In contrast, the storage S does not evolve systematically and has an average value of 2.2×10^{-4} with small fluctuations about this mean (standard deviation of the storage is 5.7×10^{-6}). The different behavior for storage and transmissivity is the result of the weak sensitivity of the solution to variations in storage coefficient [*Hsieh et al.*, 1987] and little real variation of the storage coefficient. Accordingly, we fix S to the average value to more robustly solve for T and find that the resulting values of transmissivity are unchanged from the original inversion (Figure 3-4). Because of the geometrical idealizations of the model, the absolute values are lower bounds (Appendix 3-B), although relative variations over time are more robust.

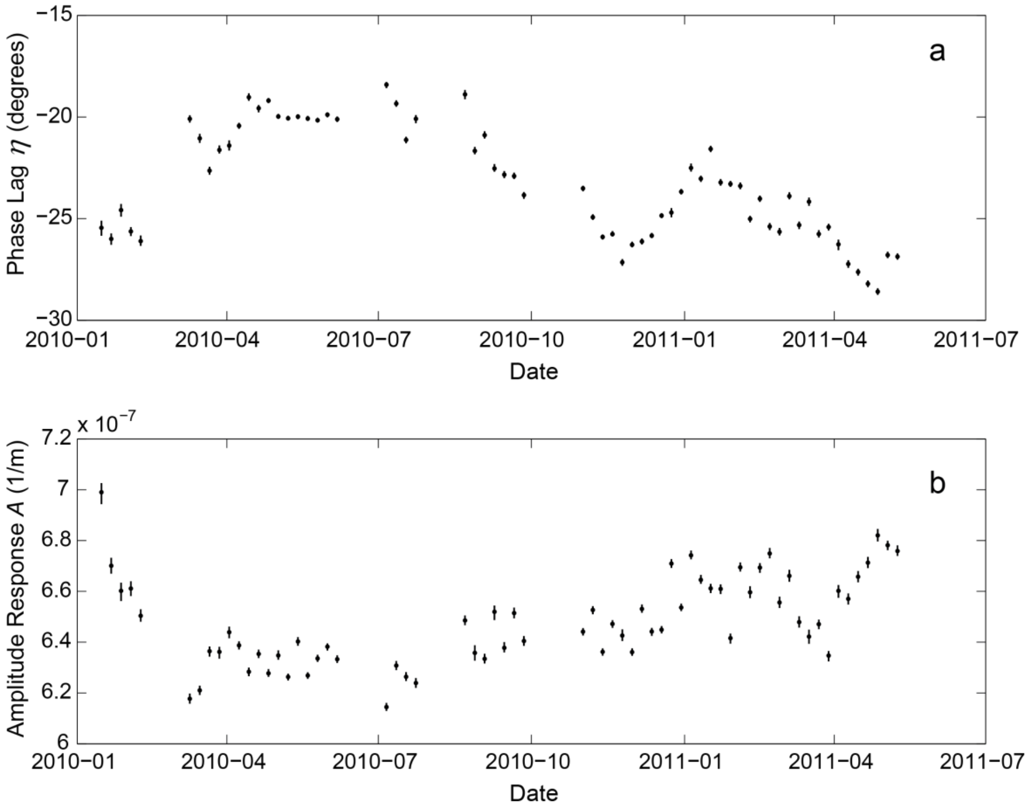

Figure 3-3. Water level response, relative to the semidiurnal tidal dilatation strain. Phase (a) and amplitude (b) response are calculated using a Bayesian Monte Carlo Markov Chain inversion method in the time domain. The inversion is applied by 29.6 day segments overlapping by 80% respectively. The error bars represent the 95% confidence interval.

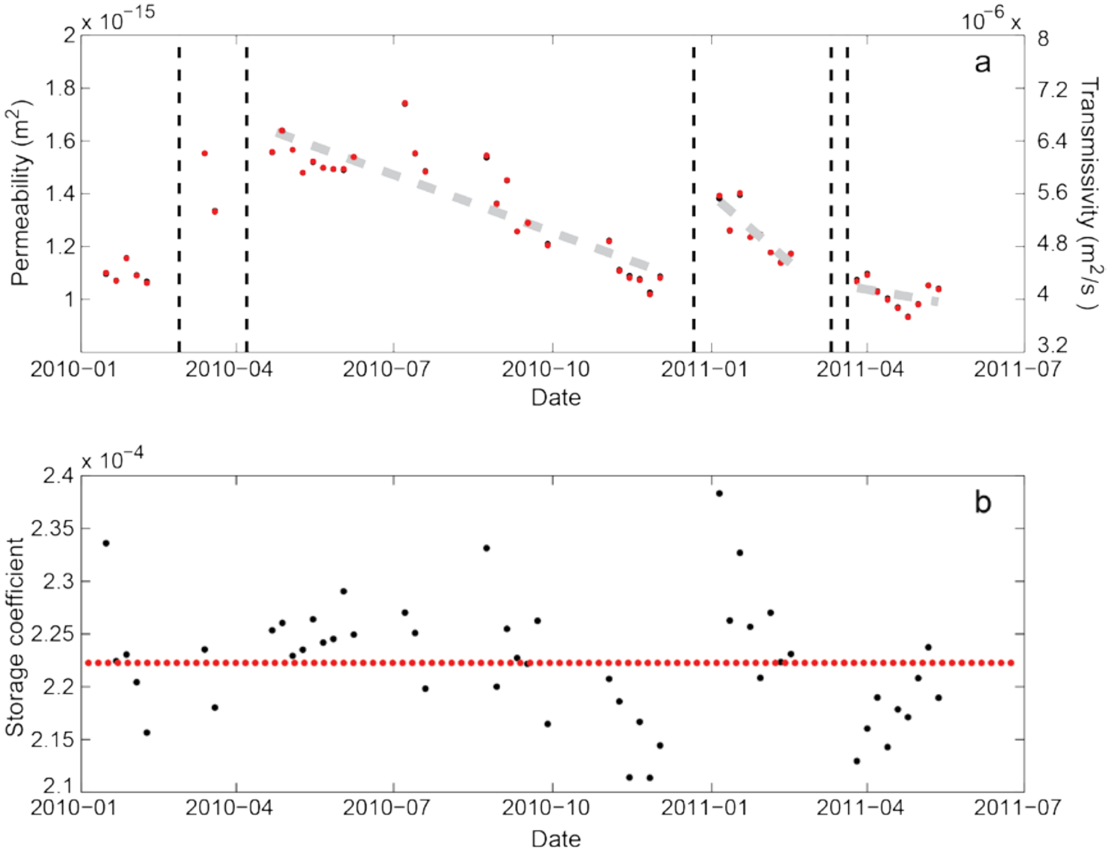

Figure 3-4. Hydrogeologic properties of the well-aquifer system over time. Permeability (a), transmissivity (a) and storage coefficient (b) are inverted from the phase and amplitude of each 29.6-day segment based on the analytical model (9). Segments that overlap the remote earthquakes (vertical dash lines) are not inverted (See Appendix 3-C for inversion results including these times). The black dots are for an unconstrained inversion; the red dots are the results of inversion with the storage coefficient fixed to a single value. Because the two separate inversions have identical results for transmissivity, the red dots cover the black dots in the upper panel (a). The vertical dash lines show the time of the selected teleseismic events, which correspond to sudden increases in permeability. The best-fit linear trends between each set of

permeability increases are shown with the light grey dashed lines. Permeability errors are estimated by propagating the range of phase errors.

For the average values of transmissivity T and storage coefficient S over the observation period, the average hydraulic diffusivity, $D=T/S$, is 2.4×10^{-2} m^2/s, which is a very high value. Based on this observed hydraulic diffusivity, the tidal observations sense a zone extending ~40 m from the well and thus are sensitive to mesoscale fractures (See Appendix 3-B). The most transmissive units in the damage zone control the tidally driven flow. The estimate of D is two orders of magnitude larger than that of the most directly comparable post-earthquake fault zone study ($7\text{x}10^{-5}$ m^2/s on the Chelungpu fault slip zone following the 1999 Chi-Chi earthquake from a cross-hole experiment [*Doan et al.*, 2006]). Our diffusivity value implies that as soon as the currently observed level of damage developed during the earthquake, co-seismic drainage was important. However, the diffusivity may be small enough that advective flow through the fault zone dose not have a major impact on the post-seismic temperature measurements that are another objective of post-earthquake studies [*Brodsky et al.*, 2010]. Previous modeling work has shown that hydraulic diffusivities comparable to the observed effective D could suppress the temperature anomaly by at most a factor of 2 relative to a conductively cooled model (See Appendix 3-D) [*P.M. Fulton et al.*, 2010], and therefore thermal anomalies in the fault zone could be observable if the fault friction is comparable to laboratory values.

The effective permeability k is related to transmissivity T by

$$k = \frac{\mu}{\rho g d} T, \qquad (3\text{-}5)$$

where μ is the fluid dynamic viscosity, d is the thickness of the open interval of the well and ρ is the density of fluid. Using $\mu=10^{-3}$ Pa s at 20°C, $\rho=10^{3}$ kg/m^{3}, g=9.8 m/s^{2}, and d=400 m, the average value of the effective permeability is 1.4×10^{-15} m^{2} (Figure 3-4). Permeability errors are estimated by propagating the range of phase errors. This approach is appropriate for measuring the precision of the inversion and these errors are useful for assessing time variability. The absolute value of the permeability is more strongly affected by the limitations of the flow model (See Appendix 3-B). The observation constrains the effective permeability averaged over the entire open interval and is therefore a lower bound for the effective permeability of the highly fractured regions.

3-5 Discussion

3-5.1 Hydrogeologic Permeability

Our observed fault zone permeability is much larger than core-scale laboratory measurements of permeability from active fault core samples [*Lockner et al.*, 1999], which range from 10^{-19} to 10^{-18} m^{2}, and the previously measured average permeability of 1.9×10^{-16} m^{2} for the intact upper Triassic rock near the Wenchuan drilling site [*Rukai et al.*, 2009]. The difference is likely due to mesoscale fractures and highlights the importance of damage in determining the field-scale behavior [*Caine et al.*, 1996].

There are also substantial temporal changes in transmissivity, which we interpret as permeability changes because the formation thickness and fluid properties are unlikely to vary during the observation period. During most of the study period, the permeability trends downward and is most easily interpreted as a reduction in fracture aperture and connectivity during the continuous evolution years after the original earthquake. Seismic studies in Wenchuan suggest that damage healed over a protracted time after the earthquake [*Y Li*, 2012], and permeability does not generally evolve in time in the absence of a disturbance [*Elkhoury et al.*, 2006]. The only candidate perturbation besides the earthquake is the drilling itself, which could potentially produce transient damage. However, drilling-induced factures are expected to extend at most a few borehole radii away from the hole [*Brudy and Zoback*, 1999], i.e.,<0.3 m, and cannot account for the phase change of the long-period tidal response that senses average properties up to ~40 m from the borehole.

3-5.2 Temporal Changes

This decreasing permeability may reflect the healing process of the fault zone after the Wenchuan earthquake due to a combination of fracture closure, sealing, precipitation, biogenic growth and pressure solution [*Gratier*, 2011]. The healing rates range from 4.1×10^{-16} m^2/yr to 2.1×10^{-17} m^2/yr using linear fits to each interval between perturbation events (Figure 3-4; SM text). Previous work [*Gratier et al.*, 2003; *Renard et al.*, 2000] modeled fault zone healing as an exponential recovery process with decay times on the order of decades or longer. However, our data are best fit with much shorter exponential decay times of 0.6-2.5 years indicating a much more rapid process than anticipated (Table 3-2). The short exponential decay times might indicate a fast healing process such as removal of props trapped in fractures or crack sealing with a strongly disequilibrated fluid to allow mass transfer with the observed characteristic times.

Fault zone healing has been documented in seismic velocity changes [*Brenguier et al.*, 2008; *Kitagawa et al.,* 2002] and suspected based on discrete repeated active formation tests [*Kitagawa et al.*, 2002]. Following the 1995 Kobe (Hyogoken-Nanbu) earthquake, water injection experiments in 1997 and 2000 tracked fluid flow in the hanging wall 50 m from the Nojima fault core and found that the permeability in 2000 had decreased to 50% of the value in 1997 [*Kitagawa et al.*, 2002]. Seismic studies document seismic velocity decreases around the fault after an earthquake continuing for years, which can also be interpreted as a consequence of fracture closure [*Brenguier et al.*, 2008; *Y-G Li et al.*, 1998; *Y Li*, 2012]. In Wenchuan, the repeated seismic velocity measurements made in the first year are consistent with such healing [*Y Li*, 2012]. As far as we are aware, healing has never before been continuously recorded in hydrogeology after a major earthquake.

The sudden increases in permeability result in an overall rate of decrease that is a factor of 1.5-7.5 more gradual than the short-term trends. Previous work suggests that permeability might be enhanced by remote or regional earthquakes [*Elkhoury et al.*, 2011; *Manga et al.*, 2012]. Plausible mechanisms include fracture unclogging due to the rapid, oscillatory flow driven by the seismic waves as they pass through the fault zone [*Elkhoury et al.*, 2011; *Manga et al.*, 2012]. The timing of the four permeability increases are correlated with the four teleseismic earthquakes that produced the largest integrated seismic shaking at the drilling site during the observation period (Table 3-2). However, like many hydrogeologic observations, the magnitudes of the perturbations are not simply proportional to that of the peak amplitude of the seismic wave [*Manga et al.*, 2012]. Most importantly, our observations imply that any physical modeling of precipitation, fracture closure or any other healing process of a fault zone needs to match the much more rapid healing rate which is only visible in the continuously recorded data.

3-6 Conclusions

An interplay between permeability evolution and fault strength has previously been suggested on geological and theoretical grounds [*Sibson*, 1992]. The Wenchuan Fault Scientific Drilling project captured the permeability evolution in the critical post-earthquake period as damage heals and the stage is set for the next earthquake. The unexpectedly high average hydraulic diffusivity (2.4×10^{-2} m^2/s) measured here also implies substantial fluid circulation in the evolving fault zone. If this value represents the hydrogeologic properties during the earthquake, fluid flow should take place during the earthquake rupture.

3-7 Acknowledgments

This work was supported by the "Wenchuan Earthquake Fault Scientific Drilling" of the National Science and Technology Planning Project in China (HL) and NSF grant EAR1220642 (EB). Seismic data from the Chinese National network is archived and distributed by Incorporated Research Institutions for Seismology (IRIS) Data Management System (DMS).

3-8 References

Agnew, D. C. (2012), SPOTL: Some Programs for Ocean-Tide Loading, edited.

Andrews, D. (2002), A fault constitutive relation accounting for thermal pressurization of pore fluid, *Journal of Geophysical Research: Solid Earth (1978–2012)*, *107*(B12), ESE 15-11-ESE 15-18.

Brenguier, F., M. Campillo, C. Hadziioannou, N. Shapiro, R. Nadeau, and E. Larose (2008), Postseismic relaxation along the San Andreas fault at Parkfield from continuous seismological observations, *Science*, *321*(5895), 1478.

Brodsky, E. E., J. Mori, and P. M. Fulton (2010), Drilling into faults quickly after earthquakes, *Eos, Transactions American Geophysical Union*, *91*(27), 237-238.

Brudy, M., and M. D. Zoback (1999), Drilling-induced tensile wall-fractures: implications for determination of in-situ stress orientation and magnitude, *International Journal of Rock Mechanics and Mining Sciences*, *36*(2), 191-215.

Caine, J. S., J. P. Evans, and C. B. Forster (1996), Fault zone architecture and permeability structure, *Geology*, *24*(11), 1025.

Doan, M., E. Brodsky, Y. Kano, and K. Ma (2006), In situ measurement of the hydraulic diffusivity of the active Chelungpu Fault, Taiwan, *Geophysical research letters*, *33*(16), 16317.

Elkhoury, J. E., E. E. Brodsky, and D. C. Agnew (2006), Seismic waves increase permeability, *Nature*, *441*(7097), 1135-1138.

Elkhoury, J. E., A. Niemeijer, E. E. Brodsky, and C. Marone (2011), Laboratory observations of permeability enhancement by fluid pressure oscillation of in situ fractured rock, *Journal of Geophysical Research*, *116*(B2), B02311.

Freeze, R. A., and J. A. Cherry (1977), *Groundwater*, Prentice-Hall.

Fulton, P. M., R. N. Harris, D. M. Saffer, and E. E. Brodsky (2010), Does hydrologic circulation mask frictional heat on faults after large earthquakes?

Fulton, P. M., R. N. Harris, D. M. Saffer, and E. E. Brodsky (2010), Does hydrologic circulation mask frictional heat on faults after large earthquakes?, *Journal of Geophysical Research: Solid Earth (1978–2012)*, *115*(B9).

Gill, J. (2002), *Bayesian methods: A social and behavioral sciences approach*, CRC press.

Gratier, J. P. (2011), Fault Permeability and Strength Evolution Related to Fracturing and Healing Episodic Processes (Years to Millennia): the Role of Pressure Solution, *Oil & Gas Science and Technology–Revue d'IFP Energies nouvelles*, *66*(3), 491-506.

Gratier, J. P., P. Favreau, and F. Renard (2003), Modeling fluid transfer along California faults when integrating pressure solution crack sealing and compaction processes, *Journal of Geophysical Research*, *108*(B2), 28-52.

Hsieh, P. A., J. D. Bredehoeft, and J. M. Farr (1987), Determination of aquifer transmissivity from earth tide analysis, *Water Resources Research*, *23*(10), 1824-1832.

Hubbert, K. M., and W. W. Rubey (1959), Role of fluid pressure in mechanics of overthrust faulting: I. Mechanics of fluid-filled porous solids and its application to overthrust faulting, *Bulletin of the Geological Society of America*, *70*(2), 115.

Kitagawa, Y., K. Fujimori, and N. Koizumi (2002), Temporal change in permeability of the rock estimated from repeated water injection experiments near the Nojima fault in Awaji Island, Japan, *Geophysical research letters*, *29*(10), 1483.

Li, H., et al. (2013), Characteristics of the fault-related rocks, fault zones and the principal slip zone in the Wenchuan Earthquake Fault Scientific Drilling Project Hole-1 (WFSD-1), *Tectonophysics*, *584*, 23-42.

Li, Y.-G., J. E. Vidale, K. Aki, F. Xu, and T. Burdette (1998), Evidence of shallow fault zone strengthening after the 1992 M7. 5 Landers, California, earthquake, *Science*, *279*(5348), 217.

Li, Y. (2012), Imaging, Modeling and Assimilation in Seismology (Beijing in China and Boston in US: China High Education Press), pp.151-198.

Lockner, D., H. Naka, H. Tanaka, H. Ito, and R. Ikeda (1999), Permeability and strength of core samples from the Nojima fault of the 1995 Kobe earthquake.

Manga, M., I. Beresnev, E. E. Brodsky, J. E. Elkhoury, D. Elsworth, S. Ingebritsen, D. C. Mays, and C. Y. Wang (2012), Changes in permeability caused by transient stresses: Field observations, experiments, and mechanisms, *Reviews of Geophysics*, *50*(2), RG2004.

Marone, C., and D. M. Saffer (2007), Fault friction and the upper transition from seismic to aseismic faulting, *The Seismogenic Zone of Subduction Thrust Faults*, (Columbia University Press, 2007), pp. 346-369.

Rempel, A. W., and J. R. Rice (2006), Thermal pressurization and onset of melting in fault zones, *J. geophys. Res*, *111*(10.1029).

Renard, F., J.-P. Gratier, and B. Jamtveit (2000), Kinetics of crack-sealing, intergranular pressure solution, and compaction around active faults, *Journal of Structural Geology*, *22*(10), 1395-1407.

Rice, J. R. (2006), Heating and weakening of faults during earthquake slip, *J. geophys. Res*, *111*(B5).

Rukai, Z., Z. Xia, L. Liuhong, W. Xuesong, Z. Nai, G. Hongli, and S. Lihong (2009), Depositional system and favorable reservoir distribution of Xujiahe Formation in Sichuan Basin, *Petroleum Exploration and Development*, *36*(1), 46-55.

Savage, H. M., and E. E. Brodsky (2011), Collateral damage: Evolution with displacement of fracture distribution and secondary fault strands in fault damage zones, *Journal of Geophysical Research: Solid Earth (1978–2012)*, *116*(B3).

Sibson, R. H. (1992), Implications of fault-valve behaviour for rupture nucleation and recurrence, *Tectonophysics*, *211*(1–4), 283-293.

Xu, Z., S. Ji, H. Li, L. Hou, X. Fu, and Z. Cai (2008), Uplift of the Longmen Shan range and the Wenchuan earthquake, *Episodes*, *31*(3), 291.

Appendix 3-A: Hydrologic context

The WFSD-1 is located on the hanging wall of the southern Yingxiu-Beichuan fault zone in Bajiamiao village [*H Li et al.*, 2013]. The borehole is at the western edge of the Sichuan basin and the local hydraulic gradient is affected by the steep local topography and the river ~ 100 m from the borehole. The water level in the borehole increased ~15 m during the observed period. The annual precipitation near the region is ~1400 mm, and usually the large rainfall occurs during July and September with ~250 mm precipitation [*Tang et al.*, 2009]. The clear tidal oscillations (Figure 3-2) indicate the aquifer is well-confined and separated from the surface water.

Appendix 3-B: The limitations of the flow model

Radius of Influence

The tidal forcing pumps water cyclically in and out of the well, and this induces a radially symmetric drawdown around the well. The width of the drawdown determines the length scale over which the hydraulic properties can be measured. Hsieh et al. (1987) provide an analytic solution of drawdown as a function of the distance to the well in a homogeneous, isotropic, confined aquifer [*Hsieh et al.*, 1987]. Using a transmissivity of 5.1×10^{-6} m^2/s and a storage coefficient of 2.2×10^{-4}, we compute the drawdown cone around the borehole (Figure 3-A1). The drawdown decays to 5% of its maximum value at a distance of 40 m from the well and the tidal response is most sensitive to variations within this region.

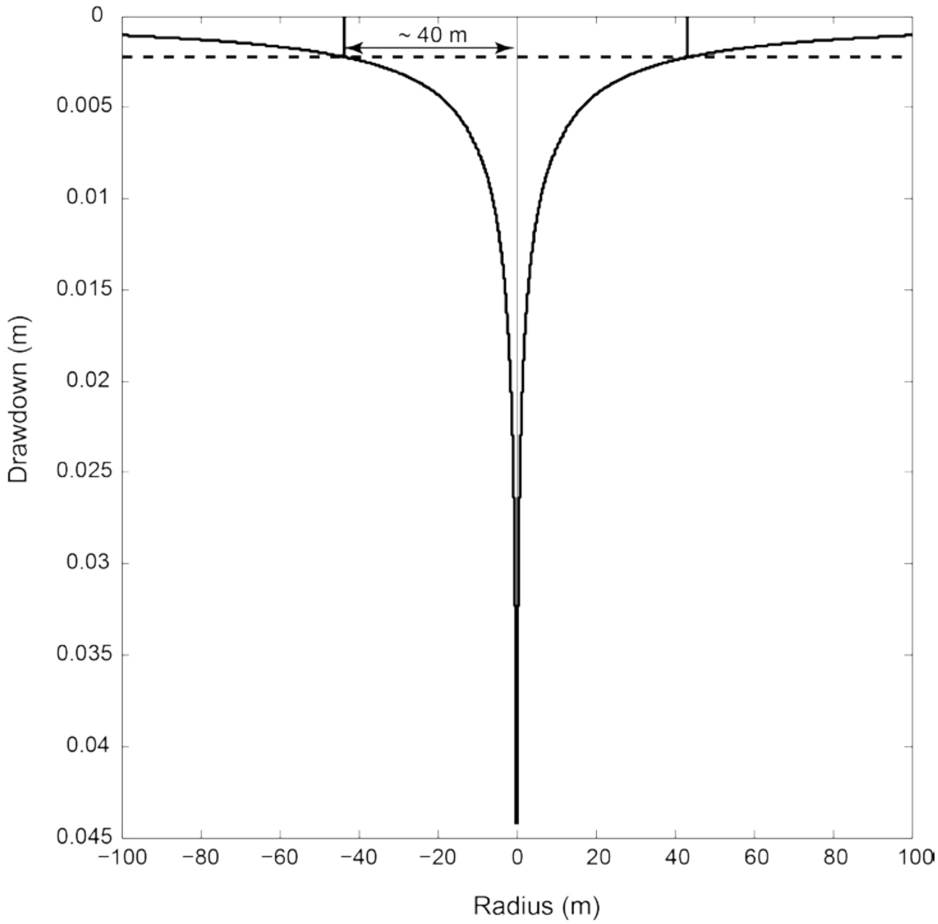

Figure 3-A1. Drawdown around the borehole. The black line is the piezometric surface. The effective length scale is ~40 m, where the drawdown decays to 5% of the maximum value. The dash line is the surface whose drawdown is 5% of the maximum value.

Axial Symmetry

The most important feature of the flow model is that the flow is radially symmetric around the well. This symmetry is naturally generated by the homogeneous, isotropic assumptions of the model and may be reproduced in nature even if there is significant heterogeneity. For a radial symmetric flow, Equations (3-3)-(3-4) form an appropriate model of the flow-averaged effective transmissivity and storage over a region extending ~40 m from the borehole (Figure 3-A1). The cylindrical geometry produces a highly focused flow that has the most sensitivity to the near-well region of any possible 2-D flow geometry, and the effective distance used to convert the observed delay (phase lag) to diffusivity is minimized. The axially symmetric solution used here therefore provides a lower bound for the transmissivity corresponding to a particular phase lag.

Depth Averaging

In our study, we inferred the depth-averaged effective permeability, transmissivity, storage and diffusivity over the entire open interval. A narrow, highly damaged layer could potentially have locally higher permeability and diffusivity. The observation constrains the effective permeability averaged over the entire open interval and is therefore a lower bound for the effective permeability for the highly fractured regions that dominate the flow. The relative magnitudes and changes in permeability are robust as the geometry is unlikely to change over time.

Appendix 3-C: Temporal changes in permeability

Using equation (3-3) and (3-4), we translate the phase responses (Figure 3-3) to permeability for all times, regardless of the timing of the teleseismic events (Figure 3-A2a). This approach is different from the results in Figure 3-4 of the main text that avoid overlapping the time of the teleseismic events events (Figure 3-4 is reproduced here as Figure 3-A2b to allow easy comparison). The consistent inversion in Figure 3-A2a has the advantage of not using an a priori information about the timing of peturbation events. The disadvantage of the appropach is that the overlapping time windows smear any step changes in permeability.

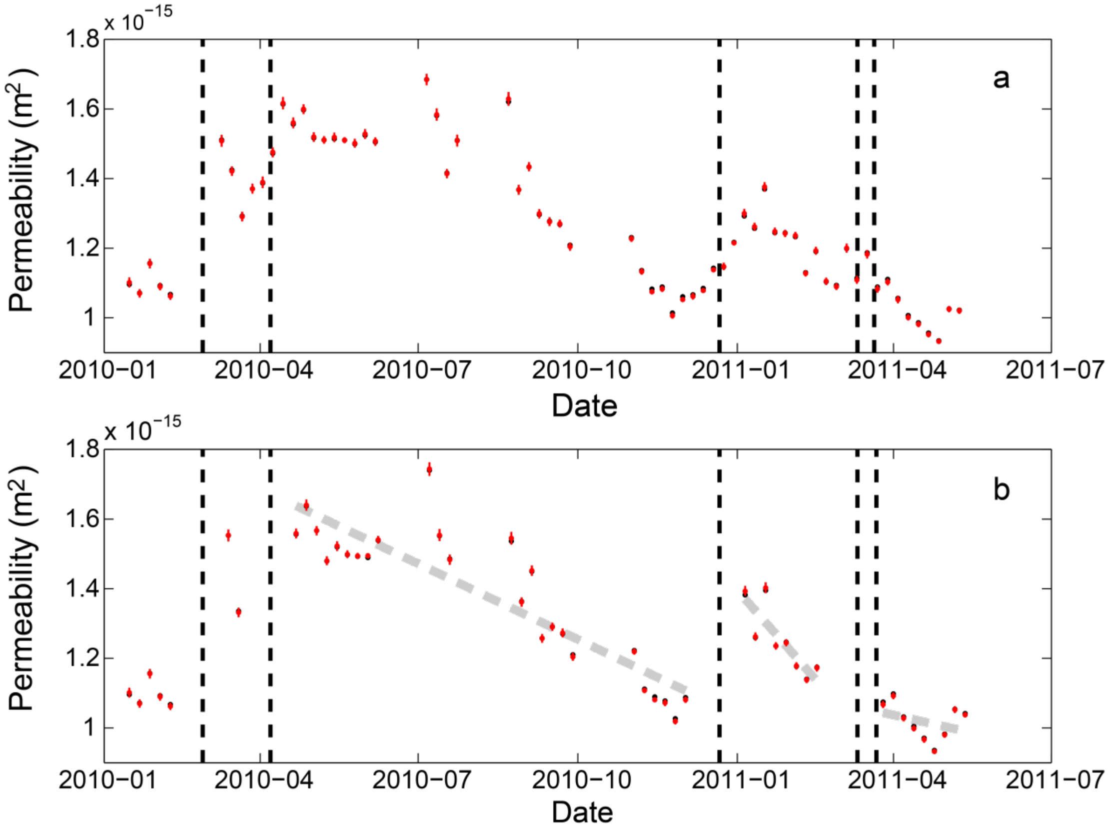

Figure 3-A2. Temporal evolution of the permeability with windows independent of teleseismic times. (a) Permeability from time windows that include the times of the selected teleseismic events. (b) Permeability from only the time windows that do not overlap the selected teleseismic events. Figure 3-A2b is identical to Figure 3-4 of the main text.

In both inversions, the time of the increased permeability is the same as the teleseismic events which have the highest integrated seismic wave energy at the borehole site. Since the time window for analysis is 29.6 days, it cannot resolve changes in phase and amplitude response occurring over time scales of several days.

Therefore, the earthquakes on Mar.11 2011 and Mar. 24 2011 are treated as one perturbation event for the purpose of analyzing the recovery intervals. Similarly, the earthquakes on Apr. 6 2011 and Apr. 13 2011 are treated as a single perturbation event. We then find the best-fit linear trend after each perturbation as well as over the full observation period. The permeability decreases 25% from January 2010 to April 2011, however within that same period, the instantaneous permeability rate change was often much higher than the overall trend (Table 3-2).

Appendix 3-D: Advective flow

Fulton et al. (2010) reported that advection could affect the observed temperature anomaly in a fault zone after an earthquake for a permeability of 10^{-14} m^2, but does not explicitly provide the corresponding hydraulic diffusivity [*Patrick M Fulton et al.*, 2010]. For the values of the study (porosity 10%, fluid compressibility of 10^{-9} Pa^{-1}, solid compressibility of 4×10^{-10} Pa^{-1}, and the fluid viscosity at 56°C of 4.8×10^{-4} Pa s), the corresponding specific storage is 4.9×10^{-6} /m and a hydraulic diffusivity is 4.1×10^{-2} m^2/s.

Table 3-A1: Periods and frequencies of the four tidal constituents used in the time domain analysis

Name of tidal continuities	Period (hour)	Frequency (cycle per day)
O1	25.819	0.9295
K1	23.934	1.0027
M2	12.421	1.9324
S2	12.000	2.0000

(Data from *Agnew*, 2007(*34*))

Table 3-A2: The six teleseismic earthquakes with the highest integrated elastic wave energy. The local elastic wave energy E is estimated from the integral of the recorded ground velocity $\dot{u}$ squared ($E = \int_0^T \dot{u}^2 dt$, where T is the duration of the seismic wave of the remote events) at the closest publically available site (station CD2, China National Seismic Network archived at IRIS Data Management Center), which is 89 km (0.8°) from the drill site. Permeability increases are measured at the time of selected earthquakes. The permeability increases are estimated by extrapolating the best-fit linear trends to the time of the remote earthquakes. There are only two permeability estimates between the Feb. 26 earthquake and Apr. 6 earthquake, so a line is not fit during this interval. The reported permeability increases at the time of these two earthquakes are the difference between the permeability before and after earthquakes. Permeability recovery rate and exponential decay time after earthquakes are based on best-fit linear and exponential trends to the data in each inter-earthquake interval.

*Notes: Perturbation from the Apr. 13, 2010 earthquake is indistinguishable from the Apr. 6, 2010 earthquake, and the perturbation from the Mar. 24, 2011 earthquake is also indistinguishable from the Mar. 11, 2011 earthquake.

Earthquake Date	**Magnitude (M_W)**	**Epicentral Distance (^{o})**	**Local Elastic Wave Energy ($10^{-3}m^2/s$)**	**Permeability Increase (10^{-16} m^2)**	**Permeability Recovery Rate (10^{-16} m^2/yr)**	**Exponential decay time (yr)**
2010-02-26	7.0	35.04	0.03	4.9	-	-
2010-04-06	7.8	29.39	0.09	2.3	8.6	1.5
2010-04-13	6.9	6.39	0.16	-*		
2010-12-21	7.4	35.04	0.03	3.5	21	0.6
2011-03-11	9.1	32.35	3.23	1.3	4.1	2.5
2011-03-24	6.8	10.98	0.032	-*		

References

Agnew, D. C. (2012), SPOTL: Some Programs for Ocean-Tide Loading, edited.

Andrews, D. (2002), A fault constitutive relation accounting for thermal pressurization of pore fluid, *Journal of Geophysical Research: Solid Earth (1978–2012)*, *107*(B12), ESE 15-11-ESE 15-18.

Elkhoury, J. E., E. E. Brodsky, and D. C. Agnew (2006), Seismic waves increase permeability, *Nature*, *441*(7097), 1135-1138.

Fulton, P. M., R. N. Harris, D. M. Saffer, and E. E. Brodsky (2010), Does hydrologic circulation mask frictional heat on faults after large earthquakes?, *Journal of Geophysical Research: Solid Earth (1978–2012)*, *115*(B9).

Hsieh, P. A., J. D. Bredehoeft, and J. M. Farr (1987), Determination of aquifer transmissivity from earth tide analysis, *Water Resources Research*, *23*(10), 1824-1832.

Li, H., et al. (2013), Characteristics of the fault-related rocks, fault zones and the principal slip zone in the Wenchuan Earthquake Fault Scientific Drilling Project Hole-1 (WFSD-1), *Tectonophysics*, *584*, 23-42.

Tang, C., J. Zhu, W. L. Li, and J. T. Liang (2009), Rainfall-triggered debris flows following the Wenchuan earthquake, *Bull Eng Geol Environ*, *68*(2), 187-194.

Chapter 4. Numerical Tidal Response of Water Level in Anisotropic Homogeneous Media

Lian Xue, Emily E. Brodsky, Patrick M. Fulton

Department of Earth and Planetary Sciences, University of California, Santa Cruz, CA 95064, USA.

Abstract

The response of water level to Earth tides provides a useful probe to determine the in-situ aquifer transmissivity. The water level in an open well tapping an aquifer responds to the Earth tidal forcing with a phase lag. The phase lag between the water level oscillation and the imposed tidal forcing is due to the finite time needed for pore pressure to readjust and drive water to flow into and out of the well. The phase lag is a direct observation, and a key parameter to determine the transmissivity of the aquifer. This study provides a partial analytical solution of the tidal response of water level under a horizontal anisotropic media. Since the partial analytical solution is not easily solvable, we explore the anisotropic effects using the finite element software *Comsol*. The numerical results suggest the estimated effective transmissivity is the geometric mean of the transmissivities in the two principal directions for weak anisotropy and is a lower bound of the transmissivity in the fast direction for strong anisotropy. For strong anisotropy where the timescale of pressure diffusion in the slow direction is limited by the borehole radius, for a given observed phase, there is

also a maximum bound on the transmissivity in the fast direction. Therefore, a given tidal response in an anisotropic medium results in a finite range of parameters.

4-1 Introduction

The aquifer response to the Earth tidal forcing can be probed by the water level in an open well [*Bredehoeft*, 1967; *Hsieh et al.*, 1987]. The imposed dilatation strain on the formation surrounding the well can pump the water in and out of the well cyclically. The water level oscillates at the same frequency as the imposed dilatation strain with a phase lag which is due to the finite time needed for pore pressure to readjust and drive water into and out of the well. This phase lag provides direct information about the in-situ hydraulic transmissivity of the aquifer. Hsieh *et al*. [1987] provided an analytical solution for the tidal response of water in a confined aquifer which is isotropic, homogeneous, infinite lateral extent and of uniform thickness. It has been successfully applied to measure the in-situ hydraulic properties of the aquifer [*Elkhoury et al.*, 2006; *Hsieh et al.*, 1987; *Xue et al.*, 2013]. Because the continuous nature of the tidal forcing allows monitoring of the evolution of permeability over time, and the passive recording avoids disturbing the in-situ hydraulic potential, this method is particularly useful for measuring the hydraulic properties of fault zones [e.g. *Elkhoury et al.*, 2006; *Xue et al.*, 2013]. However, fault zones are strongly horizontally anisotropic systems, the inferred hydraulic properties using Hsieh’s solution can be biased due to the assumptions of isotropic media. Although there are several studies about the solutions of a transient flow in a horizontally anisotropic aquifer [*Bear and Dagan*, 1965; *Fitts*, 2006; *Kucuk and Brigham*, 1979; *Mathias and*

Butler, 2007], there is no literature on the water tidal response in an anisotropic aquifer. This present study provides a partial analytical solution of the water tidal response in a horizontal anisotropic media and explores the anisotropic effect on the water level tidal response using the finite element software *Comsol*. The results are applicable to fault zones and other aquifers that may have strongly anisotropic horizontal permeability.

4-2 Governing Equations

Assuming an aquifer is deformed by a tidal forcing, the governing equation for a 2D horizontal flow is

$$T_x \frac{\partial^2 h}{\partial x^2} + T_y \frac{\partial^2 h}{\partial y^2} - S\frac{\partial h}{\partial t} - \frac{SB}{\rho g}\frac{\partial \sigma}{\partial t} = 0 \qquad (4\text{-}1)$$

where, h is the water head, T_x and T_y are the transmissivity in x and y direction separately, S is the storativity, ρ is the water density, g is the gravity acceleration constant, B is the Skempton's coefficient, and $\sigma = (\sigma_1 + \sigma_2 + \sigma_3)/3$ which is the mean stress of the imposed forcing. We assume the x and y directions are the horizontal principal directions. Since the water head in the aquifer is disturbed by the imposed tidal forcing $\sigma = \sigma_0 e^{i\omega t}$, the water level oscillations will have the same frequency with a different phase and amplitude, such that the head h can be presented as $h(x,y,t) = h_0(x,y)e^{i\omega t}$. Equation (4-1) therefore can be expressed as

$$T_x \frac{\partial^2 h_0}{\partial x^2} + T_y \frac{\partial^2 h_0}{\partial y^2} - Si\omega h_0 - \frac{SB}{\rho g} i\omega\sigma_0 = 0 \qquad (4\text{-}2)$$

At the far field boundary, it satisfies an undrained boundary condition under which the pore pressure is $p = B\sigma$. Since head is related to pore pressure p by a factor of $\frac{1}{\rho g}$, the head at the far field boundary therefore can be expressed as

$$h_0 \to \frac{B}{\rho g}\sigma \qquad r \to \infty \tag{4-3}$$

The water flux flowing into the well equals the change of the water volume inside the well over time. The boundary condition at the well wall therefore satisfies:

$$2\pi r_w \left(T_x \frac{\partial h_0}{\partial x} + T_y \frac{\partial h_0}{\partial y}\right)\Big|_{r=r_w} = \pi r_c^2 \frac{\partial h_w}{\partial t} \tag{4-4}$$

where, h_w is the water head in the well, the left hand term defines the water flux into the well, and the right hand side tern describes the time variation of the water level in the well. Inside the well, it satisfies the boundary condition $h_{w=}h_0$. We can observe in a well the complex response $R(\square) = |h_{w0}/h_{f0}|e^{i\square\square\square\square\ S,T\square}$ as a function of angular frequency $\square$ storativity S and transmissivity T, where h_{w0} is the amplitude of the head inside the water well, h_{f0} is the amplitude of the head at the far field, and ϕ is the phase lag between the water level oscillation and the imposed tidal forcing. Because earth tides are well understand, the amplitude response of water level and the time lag between the water level response and imposing tidal forcing are usually most robustly constrained. Since the phase $\square(\square\square\square\square S)$ has better constraints on hydraulic properties [*Hsieh et al.*, 1987], we usually use it to infer a suite of consistent hydraulic properties characterizing the surrounding aquifer using Eqs. (4-2)-(4-4).

Although a complete analytical solution is not possible, we can gain some insight to this problem by converting the anisotropic problem to an equivalent isotropic one with a rescaled coordinate system [*Bear*, 1972; *Bear and Dagan*, 1965]. We do this by setting $X = (\frac{T_y}{T_x})^{\frac{1}{4}} x, Y = (\frac{T_x}{T_y})^{\frac{1}{4}} y$, and then substituting into equation (4-2), giving

$$\frac{\partial^2 h_0}{\partial X^2} + \frac{\partial^2 h_0}{\partial Y^2} - \frac{Si\omega h_0}{T_g} - \frac{SB}{T_g \rho g} i\omega\sigma_0 = 0 \qquad (4\text{-}5)$$

The corresponding boundary conditions are:

$$2\pi r_w (\frac{\partial h_0}{\partial X} + \frac{\partial h_0}{\partial Y})|_{r=r_w} = \frac{\pi r_c^2}{T_g} \frac{\partial h_w}{\partial t} \qquad (4\text{-}6)$$

$$h_0 \to \frac{B}{\rho g}\sigma \qquad r \to \infty \qquad (4\text{-}7)$$

$$where,\ T_g = \sqrt{T_x T_y}\ ;\ r_w = \sqrt{x^2 + y^2} = \sqrt{(\frac{T_y}{T_x})^{\frac{1}{2}} X^2 + (\frac{T_x}{T_y})^{\frac{1}{2}} Y^2} = \sqrt{\frac{T_y}{T_g} X^2 + \frac{T_x}{T_g} Y^2}$$

Eqs. (4-5)-(4-7) show that the geometric mean of the anisotropic transmissivity ($T_g = \sqrt{T_x T_y}$) controls the governing equations in the medium and forms the effective transmissivity of an equivalent isotropic flow. Therefore, we might expect that the tidal response constrains the geometric mean transmissivity.

However, the boundary condition in Eq. 4-6 introduces a second effect of the anisotropy. The well boundary is a circle under *x, y* coordinates, while it becomes an ellipse boundary in X, Y coordinates. We will see below that for strong anisotropy, the elliptical boundary condition has a major effect on the solution beyond that captured by T_g, the geometric mean transmissivity.

4-3 Solutions

We provide a partial analytical solution of the water level tidal response under an anisotropic system (see Appendix). However, the analytical problem involves an expansion of Mathieu functions that does not have a closed form solution; therefore we pursue a numerical solution using the finite element software *Comsol* to explore the anisotropic effects on the water tidal response.

We implemented equation (4-2)-(4-4) into the partial differential equation module of *Comsol* to solve the water level response in an anisotropic system. Since we only consider the horizontal anisotropic flow, we built a 2-D model (Figure 4-1). The aquifer is modeled as a circle with two domains. One domain presents the aquifer formation and the other domain presents the water well filled with water. The aquifer is assigned aquifer transmissivity and the well domain is assigned a very large transmissivity to simulate free water movement inside the well. We choose the x and y direction as the principal directions of the transmissivity with the transmissivity in the x direction faster than that in the y direction. Parameter ranges are presented in Table 1. The imposed parameters correspond to diffusivities in the range from $5\times10^{-3}\ \mathrm{m^2/s}$ to $5\ \times10^{0}\ \mathrm{m^2/s}$, so the corresponding characteristic diffusion length is at ~15-480 m. Since the size of an efficient mesh depends on the domain size, we built models whose sizes vary with the input T_x. We utilize a circular geometry whose radius is 5 times of the characteristic diffusion length of T_x, and the results are independent of the domain size (see appendix Figure 4-A1). This allows a good approximation for infinite horizontal extension and proper mesh size to resolve the flow over small length scales. The amplitude and phase responses of the water level to tides for different given transmissivities are shown in Figure 4-2.

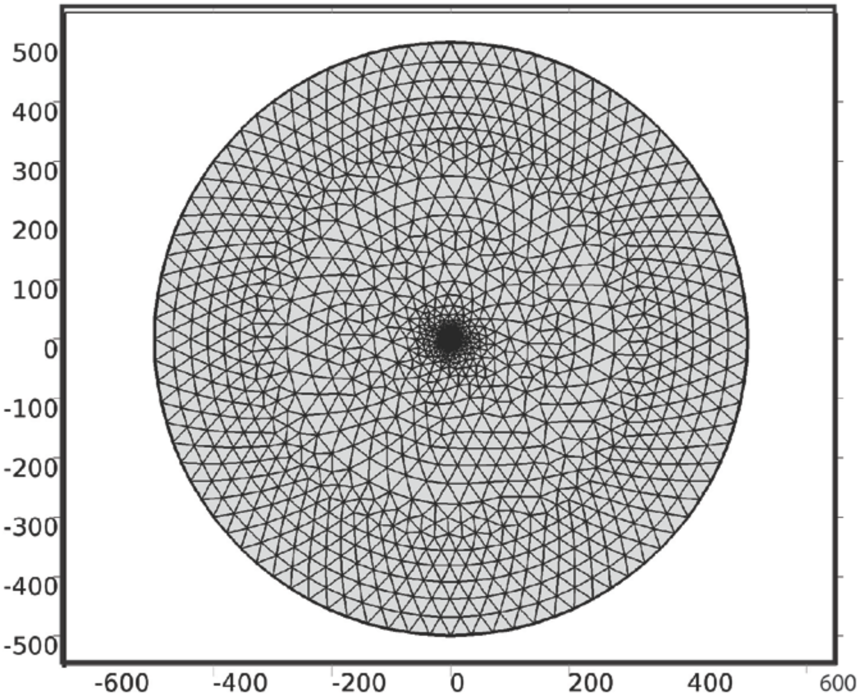

Figure 4-1. Illustration of the numerical model setup. The aquifer is a 2D circle which approximates an infinite far field boundary well. The *x* axis and *y* axis indicates the principal *x* and *y* directions of permeability.

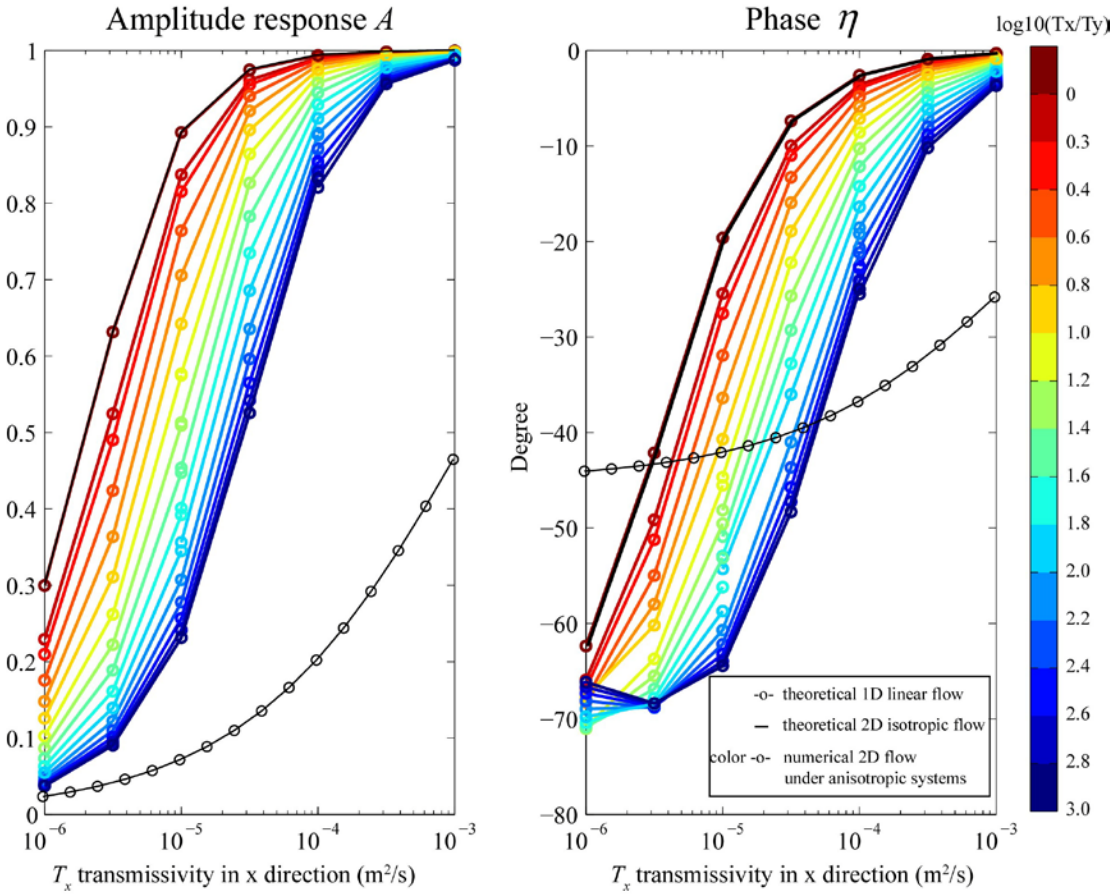

Figure 4-2. The amplitude and phase response of the water level relative to the imposed tidal forcing for given transmissivities. The color lines with circle markers are the numerical results, and the black line with the circle markers is the theoretical 1D linear flow. The solid black line is the theoretical 2D isotropic flow.

For isotropic flow T_x/T_y=1 the numerical responses are the same as the theoretical response, as expected (Figure 4-2). As the anisotropy increases, the amplitude response becomes smaller and the phase lag becomes bigger for a fixed value of the transmissivity in the fast direction (T_x). This is expected if the flow is governed by the geometric mean of the transmissivities, which decreases with decreasing T_y for a fixed

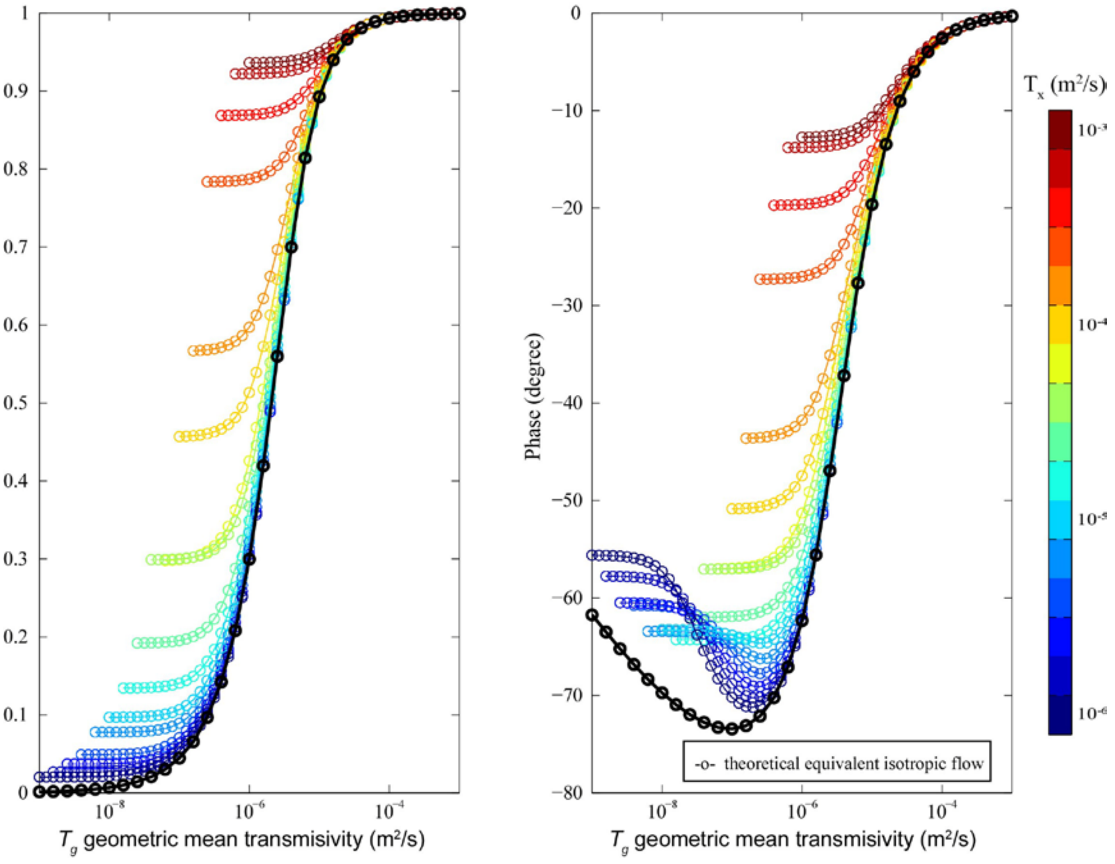

Figure 4-3. Tidal response as a function of geometric mean of transmissivities. (a) Amplitude response; (b) Phase response. Each line with circle markers is the set of responses for a fixed transmissivity in *x* direction. The warm color lines indicate large transmissivities in *x* direction, and cold color lines indicate small transmissivities in *x* direction. The black line is the result of the equivalent isotropic flow.

value of T_x. This is shown in Figure 4-3 which plots the response as a function of geometric mean transmissivity. Each colored line with circle markers indicates the set of tidal response for a fixed T_x. The amplitude response decreases and phase lag increases when the geometric mean transmissivity decreases. We discuss the flattening pattern at relatively small geometric transmissivity of each fixed T_x in the Section 4 discussion. For very high values of T_x, the solution approaches the limit of the fully drained response where the dampening effect on the amplitude response is negligible. At very low values of T_x, the response approaches the fully undrained response and the effects of anisotropy are negligible.

For strong anisotropy, the elliptical boundary becomes significant. Previous work suggests that T_x/T_y>25 is sufficient anisotropy for this effect [*Matthias and Butler*, 2007]. We also see a departure from T_g-controlled response around $T_x/T_y = 25$. For reference, we provide the solution to the 1-D linear flow problem (Fig 2, and See Supplementary). Note that the anisotropic problem is qualitatively different than a strict 1-D problem due to the inherent 2-D flow imposed by the borehole. Therefore, the 1-D solution is actually not the appropriate limit for strong anisotropy.

4-4 Case Study

The phase response between earth tides and water level is usually the direct observation, therefore we want to explore the range of corresponding solutions of transmissivity for a given phase. We have been monitoring the water level in a 1200 m deep borehole which is screened in the 2008 Wenchuan Earthquake fault zone (see Chapter 3). The water level tidal response measured from 2010 to 2011.6 gives the average phase response at 23°. We use all the numerical responses for the given transmissivities (Figure 4-2), and interpolated all the results to the corresponding transmissivity with the phase response at 23°. All the corresponding transmissivity value is shown in Figure 4-4. We define the effective transmissivity as the inferred transmissivity of an isotropic system for a fixed phase. As shown by Figure 4-4, the

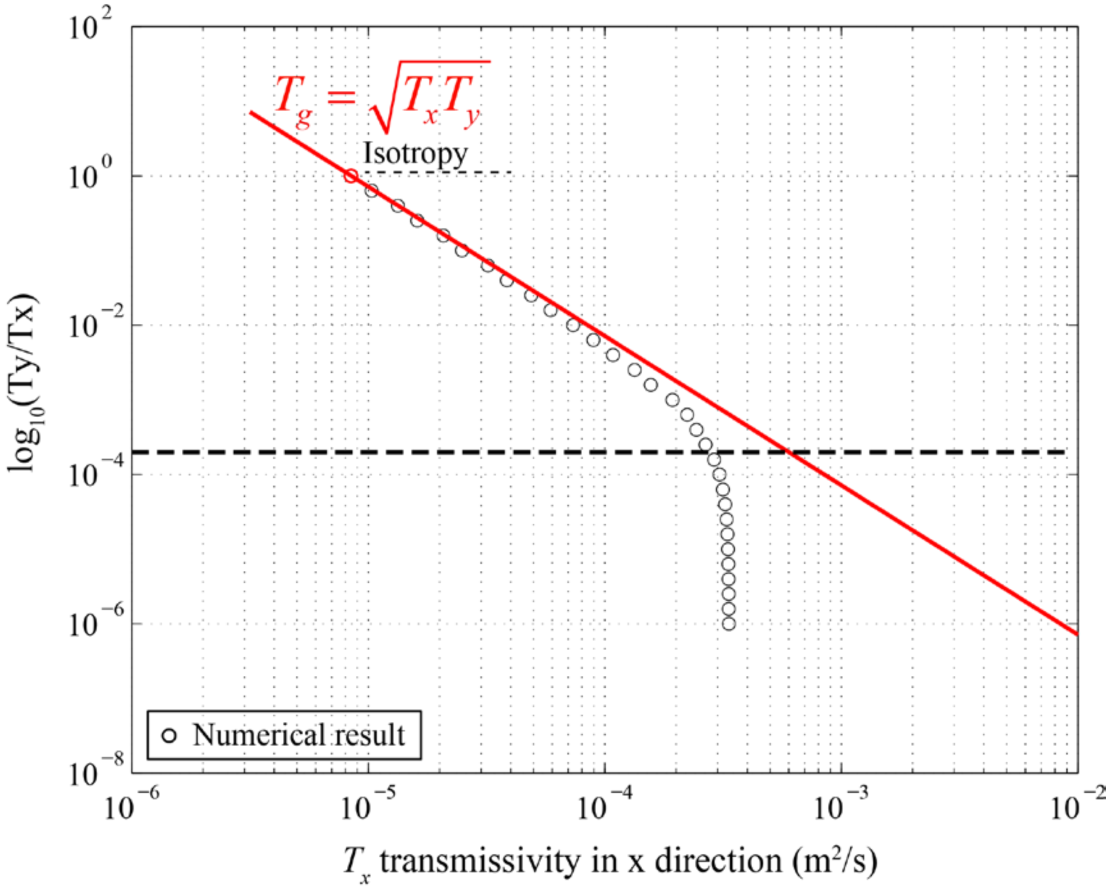

Figure 4-4. The corresponding transmissivities for the case study in the Wenchuan Earthquake fault zone. The black circles are the interpolated numerical results for the given phase at 23°, and the red circle indicates the result of the isotropic 2D flow. The red line is the effective transmissivity using the geometric mean of the two principal transmissivity. The black dash line indicates the limit of resolved transmissivity in the slow direction in the numerical modeling.

effective transmissivity is the geometric mean of the transmissivities in the two principal directions for the weak anisotropy, and it is the lower bound of the transmissivity in the fast direction for strong anisotropy. The corresponding transmissivity is divergent from the geometric mean of the two principal directions as the anisotropic effect grows stronger (Figure 4-4). In conclusion, for the phase response at 23°, the corresponding effective transmissivity is 8.5×10^{-6} m^2/s. The corresponding maximum value of the transmissivity in the fast direction is 2.9×10^{-4} m^2/s. Therefore, the range of permissible fast direction transmissivities is surprisingly limited.

4-5 Discussion

As our example illustrates the corresponding transmissivity increases very slowly as the increase of the ratio between T_x and T_y for an example observation of phase at 23° (Figure 4-4). This subtle increase of T_x at the very strong anisotropy suggests there is an upper limit of the corresponding transmissivity in the fast direction for a given phase. This means the flow is dominate by T_x when the T_y is very small. This behavior is also shown in Figure 4-3. The water tidal response is presented as a function of geometric mean transmissivity in Figure 4-3. The dark black line represents the theoretical response of the equivalent isotropic flow whose transmissivity is the geometric mean transmissivity, and each color line represents the set of response for fixed transmissivity in *x* direction. When the anisotropic effect is small (the results with larger geometric mean transmissivity for each color line), the response follows the theoretical results of the equivalent isotropic flow. This suggests the flow is controlled by geometric mean transmissivity under weak anisotropy. When the anisotropic effect is strong, the set of responses for each fixed T_x are flat (the small geometric mean transmissivity for each color line). This flattening pattern suggests the response is dominated by T_x at strong anisotropy and gives the information of T_x directly. This behavior is due to the finite radius of the well as the partial analytical solution suggests. The partial analytical solution is a function of a lumped parameter $k = \frac{\lambda S r_w^2}{4}(\frac{1}{T_y} - \frac{1}{T_x})$ which indicates T_y will dominate at very small T_y for a fixed T_x. The term $\frac{r_w^2}{T_y / \lambda S}$ is the square of the ratio between the well radius and the characteristic diffusion length in y direction ($T_y / \lambda S$). This term controls the flow regime where the 2D flow will approximate 1D flow at very small T_y for fixed $T_{x,}$. Moreover it indicates the 2D flow will not equal the 1D flow even in strong anisotropy, because the solution cannot ignore the effect of T_y even when it is very small. To explore the value of $\frac{\lambda S r_w^2}{T_y}$ at which the 2D flow starts to approximate 1D flow, we did the same numerical modeling for a large well whose radius is 10 times of the original one. We choose the responses of both models for the fixed T_x=10^3 m^2/s (Figure 4-5). As decrease of T_y, the response becomes flat (Figure 4-5). The turning-in point of the flattening pattern of the response indicates the changes of flow regime for a fixed T_x. It shows the 2D flow will approximate 1D flow, when $\frac{r_w^2}{T_y / \lambda S} > 10^2$.

At very small values of T_g, the phase response appears to reverse direction in Figure 4-2 due to phase wrapping. This regime is not observationally useful because the amplitude response for such small values of T_g is too small to observe a tidal response in the well.

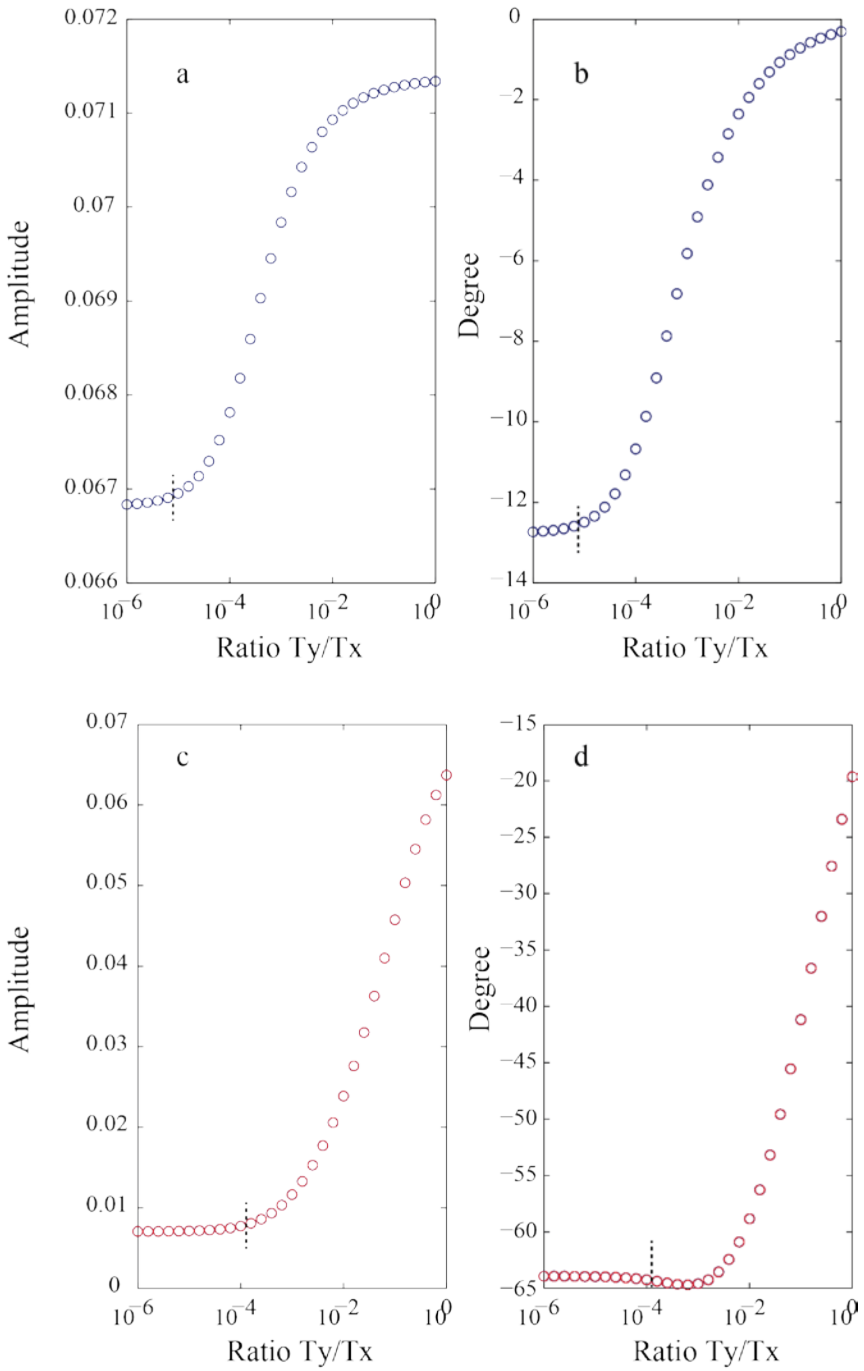

Figure 4-5. Illustration of the effect of wellbore radius. (a) and (b) are the amplitude and phase response separately as a function of ratio between T_y and T_x for small well radius of 0.1 m when T_x=10^{-3} m^2/s; (c) and (d) are the amplitude and phase response separately as a function of ratio between T_y and T_x for big well radius of 1 m when T_x=10^{-3} m^2/s. The dash lines indicate the turning-in points of the responses.

4-6 Conclusions

We provide a partial analytical solution of the water level tidal response in an anisotropic media which is not easily solvable. It does however provide insight into the governing controls and suggest that the geometric mean transmissivity is representative of the effective transmissivity. This is confirmed by the numerical models that the effective transmissivity for weak anisotropy is the geometric mean of the two principal transmissivities, and is a lower bound of the transmissivity in the fast direction for strong anisotropy. There is also an upper bound of the transmissivity in the fast direction, because the radius of the water well limits the pressure diffusion in the slow direction. Therefore, a given tidal response in an anisotropic medium results in a finite range of permissible transmissivity values. This suggests the inferred transmissivity can provide valuable information on the formation.

4.7 Acknowledgments

This project is supported by NSF grant EAR1220642. The numerical models are built using the commercial software *COMSOL*. The water level data recorded at the borehole across the Wenchuan Earthquake Fault zone can be accessed at http://www.sciencemag.org/content/340/6140/1555/suppl/DC1.

Table 4-1 The imposed parameters for the numerical models

Transmissivity T_x [m^2/s]	Anisotropy T_x/T_y	+Frequency f [s^{-1}]	*Storativity S
10^{-6}-10^{-3}	10^{0}-10^{6}	2.24×10^{-5}	2×10^{-4}

+ The chosen frequency is the frequency of the M2 tide.

*This fixed S is based on the measured storativity of the Wenchuan Earthquake fault zone [*Xue et al.*, 2013].

Table 4-2. Table of Symbols

B Skempton's coefficient [-]

g gravity acceleration constant [m^2/s]

h water head [m]

h_0 amplitude of head [m]

h_f head at far field [m]

h_{f0} amplitude of the head at far field [m]

h_w head inside the well [m]

h_{w0} amplitude of the head inside the well [m]

ω angular frequency of fluctuation [rad/s]

r	radial distance from the well [m]
r_w	radius of the well [m]
r_c	radius of the casing well [m]
S	hydraulic storativity [-]
Tx	hydraulic transmissivity in x direction which is faster than that in y direction [m^2/s]
T_y	hydraulic transmissivity in y direction [m^2/s]
T	hydraulic transmissivity [m^2/s]
T_g	geometric mean transmissivity [m^2/s]
Q	flux entering into the well [m^3/s]
Q_0	amplitude of flux inside the well [m^3/s]
σ	mean stress of the imposing forcing [Pa]
ϕ	phase lag between water level oscillation and the imposed tidal forcing [degree]

4.7 References

Bear, J. (1972), Dynamics of fluids in porous media, *Eisevier, New York*, *764p*.

Bear, J., and G. Dagan (1965), The relationship between solutions of flow problems in isotropic and anisotropic soils, *Journal of Hydrology*, *3*(2), 88-96.

Bredehoeft, J. D. (1967), Response of well-aquifer systems to Earth tides, *Journal of Geophysical Research*, *72*(12), 3075-3087.

Elkhoury, J. E., E. E. Brodsky, and D. C. Agnew (2006), Seismic waves increase permeability, *Nature*, *441*(7097), 1135-1138.

Fitts, C. R. (2006), Exact Solution for Two-Dimensional Flow to a Well in an Anisotropic Domain, *Ground Water*, *44*(1), 99-101.

Hsieh, P. A., J. D. Bredehoeft, and J. M. Farr (1987), Determination of aquifer transmissivity from earth tide analysis, *Water Resources Research*, *23*(10), 1824-1832.

Kucuk, F., and W. E. Brigham (1979), Transient flow in elliptical systems, *Society of Petroleum Engineers Journal*, *19*(06), 401-410.

Mathias, S. A., and A. P. Butler (2007), Flow to a finite diameter well in a horizontally anisotropic aquifer with wellbore storage, *Water Resources Research*, *43*(7), W07501.

Xue, L., H.-B. Li, E. E. Brodsky, Z.-Q. Xu, Y. Kano, H. Wang, J. J. Mori, J.-L. Si, J.-L. Pei, and W. Zhang (2013), Continuous permeability measurements record healing inside the Wenchuan earthquake fault zone, *Science*, *340*(6140), 1555-1559.

Appendix 4-A: Analytical solutions of a horizontally anisotropic flow

A.1 Governing Equation

Since the drawdown s can be expressed as $s = \frac{B\sigma}{\rho g} - h$, then the governing equation (4-1) in the main text for a horizontal flow in a confined, homogeneous, anisotropic, infinite lateral extended aquifer can be simplified as

$$T_x \frac{\partial^2 s}{\partial x^2} + T_y \frac{\partial^2 s}{\partial y^2} - S \frac{\partial s}{\partial t} = 0 \qquad \text{(4-a1)}$$

Where the boundary condition is

$$s|_{r=r_w} = s_{w0} \exp(i\omega t) \qquad \text{(4-a2)}$$

$$q_w\big|_{r=r_w} = \pi ab \frac{dh_w}{dt} \qquad \text{(4-a3)}$$

$$s \to 0 \qquad r \to \infty \qquad \text{(4-a4)}$$

where T_x and T_y are the transmissivity in x, y direction separately, S is storativity, q_w is the flow flux at the wall of the well, the h_w is the water head inside the well, and a, b are the major and minor axis of the elliptical inner boundary separately. Numerical values used of all of the parameters are presented in the parameter table.

A.2 An equivalent isotropic equation

The anisotropic domain can be transformed into an equivalent isotropic domain by rescaling the coordinates [*Bear*, 1972; *Bear and Dagan*, 1965] as follows:

Set $X = (\frac{T_y}{T_x})^{\frac{1}{4}} x, Y = (\frac{T_x}{T_y})^{\frac{1}{4}} y$, then substitute into equation (4-a1).

$$\frac{\partial^2 s}{\partial X^2} + \frac{\partial^2 s}{\partial Y^2} - \frac{S}{T_g}\frac{\partial s}{\partial t} = 0 \qquad \text{(4-a5)}$$

$$s|_{r=r_w} = s_{w0}\exp(i\omega t) \qquad \text{(4-a6)}$$

$$q_w\big|_{r=r_w} = \pi ab\frac{dh_w}{dt} \qquad \text{(4-a7)}$$

$$s \to 0 \qquad r \to \infty \qquad \text{(4-a8)}$$

where, $T_g = \sqrt{T_x T_y}$, $r_w = \sqrt{\frac{T_y}{T_g}X^2 + \frac{T_x}{T_g}Y^2}$

The well boundary is a circle under *x*, *y* coordinates and is transformed to an ellipse boundary in *X*, *Y* coordinates. From equation (a5), it shows the equivalent effective transmissivity is the geometric mean of the transmissivity in the two principal directions. This is only valid when the anisotropic effect is weak such as $T_y/T_x < 25$ [*Mathias and Butler*, 2007], because the elliptical boundary effect introduces a second effect of the strong anisotropy.

A.3 Analytical solutions under the elliptical coordinates

We apply an elliptical transform [*McLachlan*, 1947] to the equation (a5) as follows:

Set $\begin{array}{l} Y = L\sinh\xi\sin\eta \\ X = L\cosh\xi\cos\eta, \end{array}$

where, $L = ae = r_w(\frac{T_x}{T_y})^{\frac{1}{4}}(1-\frac{T_y}{T_x})^{\frac{1}{2}} = r_w(\frac{(T_x-T_y)^2}{T_yT_x})^{\frac{1}{4}}$, e is the eccentricities of ellipse, and ξ, η are the parameters for the elliptical coordinates.

The Laplace operator under elliptical coordinates can be expressed as

$$\frac{\partial^2}{\partial X^2}+\frac{\partial^2}{\partial Y^2}=\frac{2}{L^2(\cosh 2\xi-\cos 2\eta)}(\frac{\partial^2}{\partial\xi^2}+\frac{\partial^2}{\partial\eta^2}) \qquad \text{(4-a9)}$$

Then the equation (a5) is transformed to

$$(\frac{\partial^2 s}{\partial\xi^2}+\frac{\partial^2 s}{\partial\eta^2})-\frac{L^2}{2}[(\cosh 2\xi-\cos 2\eta)]\frac{S}{T_g}\frac{\partial s}{\partial t}=0 \qquad \text{(4-a10)}$$

Subject to

$$s=(h_f-h_w), \qquad \xi=\xi_w, 0\le\eta<2\pi, t>0 \qquad \text{(4-a11)}$$

$$q_w=\pi ab\frac{dh_w}{dt}, \qquad \xi=\xi_w, 0\le\eta<2\pi, t>0 \qquad \text{(4-a12)}$$

$$s\to 0 \qquad \xi\to\infty \qquad \text{(4-a13)}$$

where $\xi_w = \cosh^{-1}((\frac{T_y}{T_x - T_y})^{\frac{1}{2}})$ (4-a14)

We applied Laplace transform to solve the equations (4-a10)-(4-a13). The Laplace transformations of the equation (4-a10)-(4-a13) can be presented by:

$$(\frac{\partial^2 \overline{s}}{\partial \xi^2} + \frac{\partial^2 \overline{s}}{\partial \eta^2}) - \frac{L^2}{2}[(\cosh 2\xi - \cos 2\eta)]\frac{S}{T_g}\lambda \overline{s} = 0 \qquad (4\text{-a15})$$

$$\overline{s} = \overline{h}_f - \overline{h}_w, \qquad \xi = \xi_w, 0 \le \eta < 2\pi, t > 0 \qquad (4\text{-a16})$$

$$\overline{q}_w = \pi ab\lambda \overline{h}_w, \qquad \xi = \xi_w, 0 \le \eta < 2\pi, t > 0 \qquad (4\text{-a17})$$

$$\overline{s} \to 0 \qquad \xi \to \infty \qquad (4\text{-a18})$$

where λ is the constant of Laplace transformation, and $\overline{s}, \overline{h}_f, \overline{h}_w, \overline{q}_w$ are the Laplace transforms of the s, h_f, h_w, q_w separately.

Assuming a solution in the form of

$$\overline{s} = E(\xi)F(\eta) \qquad (4\text{-a19})$$

Plug in to equation (4-a15) yields

$$\frac{1}{E}\frac{\partial^2 E}{\partial \xi^2} - \frac{L^2\lambda}{2}\frac{S}{T_g}\cosh 2\xi E = -\frac{1}{F}\frac{\partial^2 F}{\partial \eta^2} - \frac{L^2\lambda}{2}\frac{S}{T_g}\cos 2\eta F \qquad (4\text{-a20})$$

Set each side equals to a constant C

$$\frac{\partial^2 E}{\partial \xi^2} - (C + 2k\cosh 2\xi)E = 0 \tag{4-a21}$$

$$\frac{\partial^2 F}{\partial \eta^2} + (C + 2k\cos 2\eta)F = 0 \tag{4-a22}$$

$$\text{where, } k = \frac{L^2\lambda}{4}\frac{S}{T_g} = \frac{\lambda S r_w^2}{4}\left(\frac{1}{T_y} - \frac{1}{T_x}\right) \tag{4-a23}$$

Eqs. (4-a21)-(4-a22) are the modified Mathieu functions. The desired solution $\overline{s}$ is symmetrical about the η axis and converges at infinite ξ then the general solution of (4-a20) is

$$\overline{s} = \sum_{n=0}^{\infty} c_{2n} Fek_{2n}(\xi, -k) ce_{2n}(\eta, -k) \tag{4-a24}$$

This solution satisfies the far field boundary condition (4-a18). Plug this equation into the constant head boundary condition (4-a16), and use the orthogonality of the Mathieu function:

$$\begin{aligned} &\sum_{n=0}^{\infty} c_{2n} Fek_{2n}(\xi_w, -k) ce_{2n}(\eta, -k) = \overline{h}_f - \overline{h}_w \\ &c_{2n} = (-1)^n \frac{2(\overline{h}_f - \overline{h}_w)A_0^{2n}}{Fek_{2n}(\xi_w, -k)} \end{aligned} \tag{4-a25}$$

Plug equation (4-a25) into equation (4-a24)

Then

$$\bar{s} = \sum_{n=0}^{\infty} (-1)^{\mathrm{n}} \frac{2(\bar{h}_f - \bar{h}_w)\,\mathrm{A}_0^{2n}\, Fek_{2n}(\xi,-k)}{Fek_{2n}(\xi_w,-k)} ce_{2n}(\eta,-k) \tag{4-a26}$$

This is the solution for the drawdown of a horizontal anisotropic flow. This is the same as the solution of the transient flow in elliptical system [*Kucuk and Brigham*, 1979].

To find $\bar{h}_w$ inside the well. We will use the boundary condition (4-a17). The flow flux entering the internal boundary from the reservoir is

$$\begin{aligned} \bar{q}_w &= -T_g \int_0^{2\pi} \left.\frac{\partial \bar{s}}{\partial \xi}\right|_{\xi=\xi_w} d\eta \\ q_w &= -4\pi T_g \sum_{n=0}^{\infty} \frac{(\bar{h}_f - \bar{h}_w)(\mathrm{A}_0^{(2n)})^2 Fek'_{2n}(\xi_w,-k)}{Fek_{2n}(\xi_w,-k)} \end{aligned} \tag{4-a27}$$

Using equation (a17) and (a27) to solve $\bar{h}_w$,

$$-4\pi T_g \sum_{n=0}^{\infty} \frac{(\bar{h}_f - \bar{h}_w)(\mathrm{A}_0^{(2n)})^2 Fek'_{2n}(\xi_w,-k)}{Fek_{2n}(\xi_w,-k)} = \pi ab\lambda \bar{h}_w \tag{4-a28}$$

Then we can apply inverse Laplace transformation to equation (4-a26) to solve the drawdown inside the well. However, it is not straightforward to solve this equation. Probably it can be simplified by using finite terms of the left side of this equation as an approximation.

A.4 Degeneration to a radial flow

For an isotropic aquifer with $T_y = T_x$, then

$$L \to 0\,, k = \frac{L^2\lambda}{4}\frac{S}{T_g} \to 0 \tag{4-a29}$$

$$Fek_0(\xi_w, -k) \to \frac{1}{2\pi} K_0((\lambda\frac{S}{T_g})^{1/2} r_w) \tag{4-a30}$$

$$Fek_0^{'}(\xi_w, -k) \to \frac{r_w(\lambda\frac{S}{T_g})^{1/2}}{2\pi} K_0^{'}((\lambda\frac{S}{T_g})^{1/2} r_w) = -\frac{r_w(\lambda\frac{S}{T_g})^{1/2}}{2\pi} K_1((\lambda\frac{S}{T_g})^{1/2} r_w) \tag{4-a31}$$

$$A_0^0 \to 2^{-1/2} \tag{4-a32}$$

Then the equation (a27) is degenerated as:

$$\bar{q}_w = 2\pi T_g \frac{(\bar{h}_f - \bar{h}_w) r_w (\lambda\frac{S}{T_g})^{1/2} K_1((\lambda\frac{S}{T_g})^{1/2} r_w)}{K_0((\lambda\frac{S}{T_g})^{1/2} r_w)} \tag{4-a33}$$

Using equation (4-a17)

$$\bar{h}_w = \frac{\bar{h}_f}{1 + \frac{r_c^2}{r_w^2} \frac{r_w \lambda}{2T_g(\lambda\frac{S}{T_g})^{1/2}} \frac{K_0((\lambda\frac{S}{T_g})^{1/2} r_w)}{K_1((\lambda\frac{S}{T_g})^{1/2} r_w)}} \tag{4-a34}$$

Since $\bar{h}_f = h_{f_0}\delta(i\omega - \lambda)$

Inverse Laplace transfer of $\bar{h}_w$ is

$$h_w = \frac{h_{f_0} e^{i\omega t}}{1 + \frac{r_c^2}{r_w^2} \frac{r_w (i\omega S / T_g)^{1/2}}{2S} \frac{K_0((i\omega \frac{S}{T_g})^{1/2} r_w)}{K_1((i\omega \frac{S}{T_g})^{1/2} r_w)}} \qquad \text{(4-a35)}$$

This is exact as the solution of *Hsieh et al.*, [1987].

Appendix 4-B: Analytical solution of a 1D linear flow

The governing equation for the 1D linear flow can be expressed as:

$$T \frac{\partial^2 s}{\partial x^2} - S \frac{\partial s}{\partial t} = 0 \qquad \text{(4-b1)}$$

$$s \to 0, \text{when } x \to \infty \qquad \text{(4-b2)}$$

$$2\pi r_w T \frac{\partial s}{\partial x} |_{x=r_w} = -Q e^{i\omega t} \qquad \text{(4-b3)}$$

where *s* is the drawdown, *T* is transmissivity, *S* is the storativity, r_w is the radius of the water well, and *Q* is the volumetric flux.

The general solution for equation (4-b1) with boundary condition (4-b2) is

$$s = A e^{-\sqrt{\frac{Si\omega}{T}} x} e^{i\omega t} \qquad \text{(4-b4)}$$

where *A* is a constant.

The boundary condition at the well also satisfies $\pi r_c^2 \frac{\partial h_w}{\partial t}|_{x=r_w} = Qe^{i\omega t}$. Then the constant A is $A = \frac{r_c^2 i\omega h_{w_0}}{2r_w\sqrt{TSi\omega}} e^{\sqrt{\frac{Si\omega}{T}}r_w}$ (4-b5)

where h_{w0} is the amplitude of the water head inside the well, and h_w is the water head inside the well. The amplitude of the water head inside the well can be expressed as

$$h_{w_0} = h_0 - \frac{r_c^2 i\omega h_{w_0}}{2r_w\sqrt{TSi\omega}},$$

then the response of the 1D linear flow inside the well can be expressed as

$$\frac{h_{w_0}}{h_0} = (1+\frac{r_c^2}{2r_w}\sqrt{\frac{i\omega}{TS}})^{-1} \qquad (4\text{-b6})$$

Appendix 4-C: Independence of domain size in numerical models

The numerical models of circular aquifers have radiuses which are 5 times of the characteristic diffusion length of T_x. The domain size is big enough to approximate the infinite horizontal extension well. To demonstrate our results are independent of the domain size, the radiuses are increased to 10 times of the characteristic diffusion length of T_x with the same mesh sizes. First, we compared the numerical results with the analytical solution for an isotropic flow (Figure 4-A1(a)(b)). The difference between the numerical results and the theoretical results are small, and the subtle difference does not change with the domain size. Second, we compared the numerical results of a flow under an anisotropic system with the equivalent analytical isotropic flow (Figure 4-A1(c)(d)). When T_x/T_y=10, the difference between the numerical results and the theoretical results are relative larger than that of the isotropic flow (T_x/T_y=1), but the results of the models with different domain size have the almost same pattern. The analytical solution of the equivalent theoretical isotropic flow is an approximation for the anisotropic flow, so it results in a relatively larger difference between the numerical results and the analytical solutions. This comparison shows our numerical results are independent of the domain size.

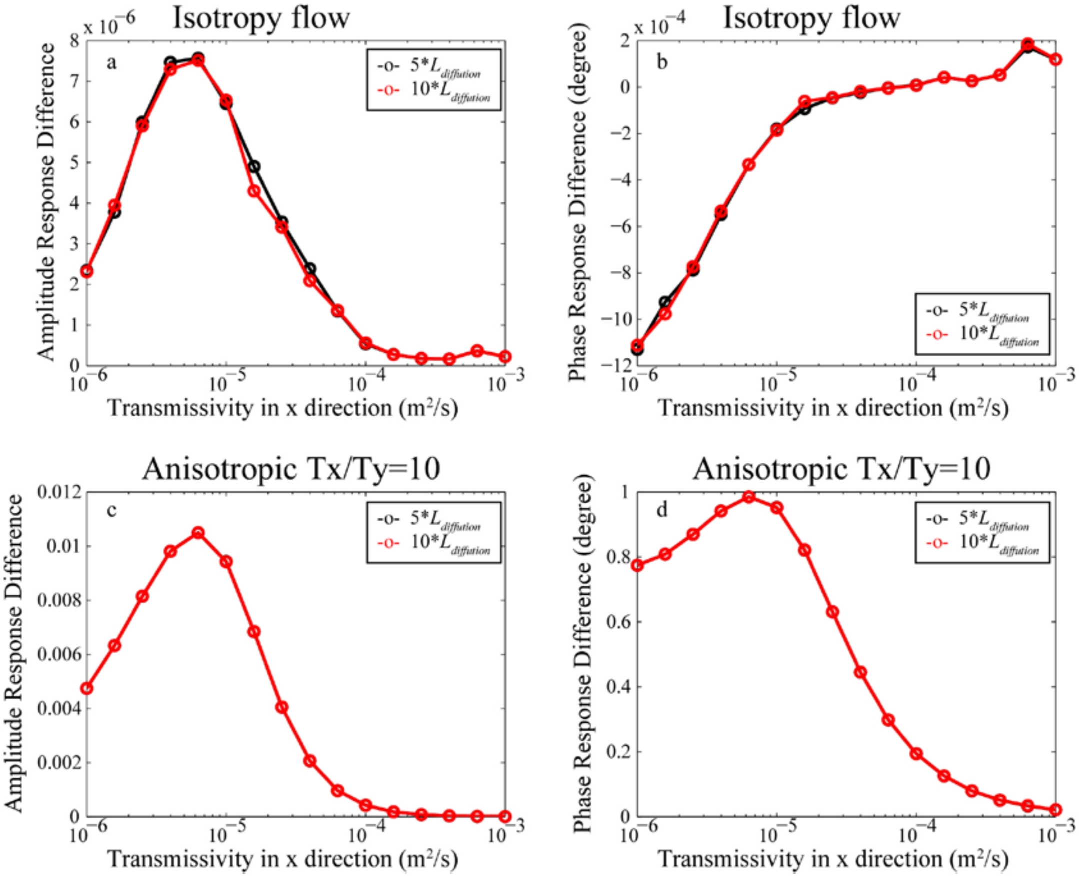

Figure 4-A1. (a) and (b) the difference between numerical models and the analytical results for an isotropic flow. (c) and (d) the difference between numerical models and the analytical results under an anisotropic system when T_x/T_y=10. The black circles are the differences between the results of the model with a domain size of 5 times of the characteristic diffusion length in the *x* direction and the analytical models. The red circles are the differences between the results of the model with a domain size of 10 times of the characteristic diffusion length in the *x* direction and the analytical models.

Appendix 4-Tables:

Table of parameters

s	drawdown due to the imposed tidal forcing [m]
s_0	amplitude of the drawdown [m]
r	radial distance from the well [m]
r_w	radius of the well [m]
r_c	radius of the casing well [m]
S	hydraulic storativity [-]
T	hydraulic transmissivity [m^2/s]
T_g	geometric mean transmissivity [m^2/s]
Q	flux in the well [m^3/s]
Q_0	amplitude of flux inside the well [m^3/s]
h_f	head at far field [m]
h_{f0}	amplitude of the head at far field [m]
h_w	head inside the well [m]
h_{w0}	amplitude of the head inside the well [m]
ω	angular frequency of fluctuation [rad/s]

λ constant of Laplace transformation

$Fek_{2n}(\xi,-k),\ ce_{2n}(\eta,-k)$ Mathieu functions

$K_1(z),\ K_0(z)$ the modified Bessel functions of the second kind

References

Bear, J. (1972), Dynamics of fluids in porous media, *Elsevier, New York, 764p*.

Bear, J., and G. Dagan (1965), The relationship between solutions of flow problems in isotropic and anisotropic soils, *Journal of Hydrology*, *3*(2), 88-96.

Hsieh, P. A., J. D. Bredehoeft, and J. M. Farr (1987), Determination of aquifer transmissivity from earth tide analysis, *Water Resources Research*, *23*(10), 1824-1832.

Kucuk, F., and W. E. Brigham (1979), Transient flow in elliptical systems, *Society of Petroleum Engineers Journal*, *19*(06), 401-410.

Mathias, S. A., and A. P. Butler (2007), Flow to a finite diameter well in a horizontally anisotropic aquifer with wellbore storage, *Water Resources Research*, *43*(7), W07501.

McLachlan, N. W. (1947), Theory and application of Mathieu functions, Oxford University Press, New York.

Chapter 5. Hydrogeologic Architecture of the San Andreas Fault near the Logan Quarry

Lian Xue[1], Emily Brodsky[1], Jon Erskine[2], Patrick Fulton[1], Reed Carter[2]

1. Department of Earth and Planetary Sciences, University of California, Santa Cruz, CA 95064, USA.
2. Graniterock , Watsonville, CA,USA

Abstract

Hydrogeologic properties of fault zones are critical to the faulting processes; however, they are not well understood and difficult to measure in situ. Recording the tidal response of water level is a useful method to measure the in-situ properties. We utilize an array of wells near the San Andreas Fault zone in the Logan Quarry to study the fault zone hydrogeologic architecture by measuring the water tidal response. The specific storage and permeability inferred from the tidal response suggest that there is a difference in properties at different distances to the fault. The sites closer to the fault have higher specific storage and higher permeability. This difference of properties might be related to the fault zone fracture distribution. Surprisingly, the difference in specific storage is the clear signal. The inferred compliance contrast is consistent with prior estimates of elastic moduli in the near-fault environment, but the hydrogeologic effects of differences in the compliance have rarely been measured on a major active

fault. In addition, the measured diffusivity is about 10^{-2} m^2/s, which is comparable to the post-earthquake hydraulic diffusivity measured on the Wenchuan Earthquake Fault. Beacause of the competing effect of permeability and specific storage, the resulting diffusivity is uniform inside the fault zone. This uniform diffusivity structure might suggest that the accumulated pore pressure during the interseismic period distributes over a broad region.

5-1 Introduction

Increasing pore pressure weakens fault zones by reducing the effective stress [*Hubbert and Rubey*, 1959]. During fault slip, the pore pressure evolution depends on the hydrogeologic properties of a fault zone [*Andrews*, 2002; *Byerlee*, 1993; *Segall and Rice*, 1995]. During the interseismic period, the hydrogeologic properties of the fault damage zone determine the development of pore pressure inside the fault zone which may affect the failure of the fault [*Rice*, 1992]. In addition, the hydrogeologic properties of the fault zone can also serve as an indicator of fracture density, therefore the hydrogeologic structures of fault zones can reflect the deformation conditions within fault zones [*Caine et al.*, 1996]. However, the hydrogeologic properties of a fault zone are hard to measure and less well understood. Continuous water level responses to tidal forcing enable us to probe the in situ hydrogeologic properties of fault zone [*Elkhoury et al.*, 2011; *Hsieh et al.*, 1987; *Xue et al.*, 2013]. This study utilizes an array of water wells with different distances to the fault and uses water level tidal response to study the hydrogeologic architecture of the San Andreas Fault in the Logan Quarry.

5-2 Tectonic background

The A.R. Wilson Quarry is owned by Graniterock and located on the southwestern side of the San Andreas Fault in Aromas, California (Figure 5-1A). The facility was historically known as the Logan Quarry and we use the older name here to be consistent with the existing geological literature on the site. The quarry is exploiting the exposed sliver of quartz gabbro which is unconformably overlain by Eocene to Miocene sedimentary and volcanic rocks. The high fracture density inside the fault damage zone makes the quarry an economic source of construction material and the quarry has been active for over 100 years. The quartz gabbro at this site is correlated with the quartz gabbro at Gold Hill about 180 km to the southeast which indicates the long-term average slip rate of the San Andreas fault is 25-35 mm/yr [*Ross*, 1970]. This site is near the edge of the locked portion of the San Andreas Fault. Historic seismic slip was documented by a rail road located between the Chittenden and the Pajaro Bridges near the Quarry that was bent in the 1906 San Andreas earthquake [*Lawson and Reid*, 1908] (Figure 5-1A). The most prominent strand of the San Andreas Fault inside the quarry is a lithology boundary with quartz gabbro on the southwest side and shale on the northeast side (Figure 5-1A). This major boundary is clearly the locus of the largest displacement, although other strands of the fault may be active at the present time. We will therefore refer to the lithologic boundary as the San Andreas Fault.

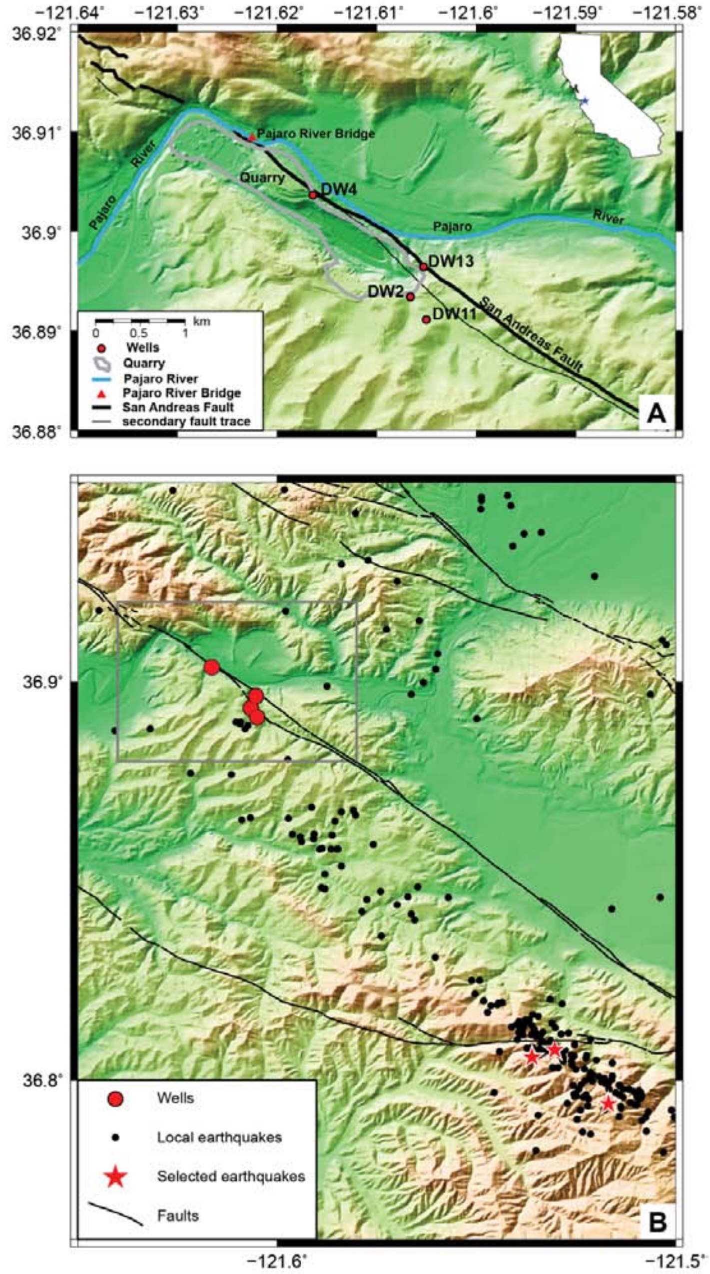

Figure 5-1. (A) Map of Logan Quarry. The red dots show the location of the wells. The black lines show the local faults. The San Andreas fault is the major fault which is indentified from a lithology boundary. The red triangle shows the bent rail road in the 1906 San Andreas Earthquake. The blue line shows the Pajaro River in Chittenden. The background shows the topography. The blue star in the inset map shows the location of the quarry in the California. (B) The location of earthquakes. The black dots are the local earthquakes occurred in 30 km to the Quarry during our

observation time. The red stars show the locations of the selected earthquakes which caused the permeability change in the Quarry. The gray rectangle identifies the location of Quarry which is enlarged in the map in panel A.

5-3 Observations

We utilize four wells (DW4, DW11, DW 13 and DW 2) at various distances to the San Andreas Fault to observe the water level tidal response (Figure 5-1A). All of the chosen wells are on the southwest sides of the San Andreas Fault within the gabbro formation, and their screened intervals are in the fractured gabbro.

Pressure sensors measured the height of the column of water above the sensor in each of the 4 wells as detailed in Table 1 and shown in Figure 5-2. The water levels have been observed from April 2014 through July 2015 with 10 minute sample intervals. Originally all of the wells used a HOBO pressure transducer (model U20-001-01-Ti with depth range of 100 ft) with a resolution of 0.46 cm. The well DW4 has a small signal of water tidal response near the resolution of the HOBO logger, so we changed the pressure sensor inside the DW4 to an RBR (model SoloD with depth range of 20 m) which has a better resolution ~0.03 cm on May 18, 2015. To evaluate the affects of the barometric pressure, we also deployed a pressure transducer in the air inside well DW4. The logger of DW13 was jammed on the well wall, so there was no recorded water level oscillation during Aug.-Nov. 2014. Otherwise, the time series are uninterrupted for the 15 month period (Figure 5-3). The water levels were not disturbed by data retrievals (Figure 5-3). The biggest step change of water level occurred at April 12, 2015 which was observed at all the wells except DW4. This water level jump is not related to any local earthquakes or quarry blast events. The cause of this step change is not clear. The long term trend of the observed water levels inside each wells are not related to the trend in the height of the Pajaro River (Figure 5-3), so the connection between the river and the wells are not significant.

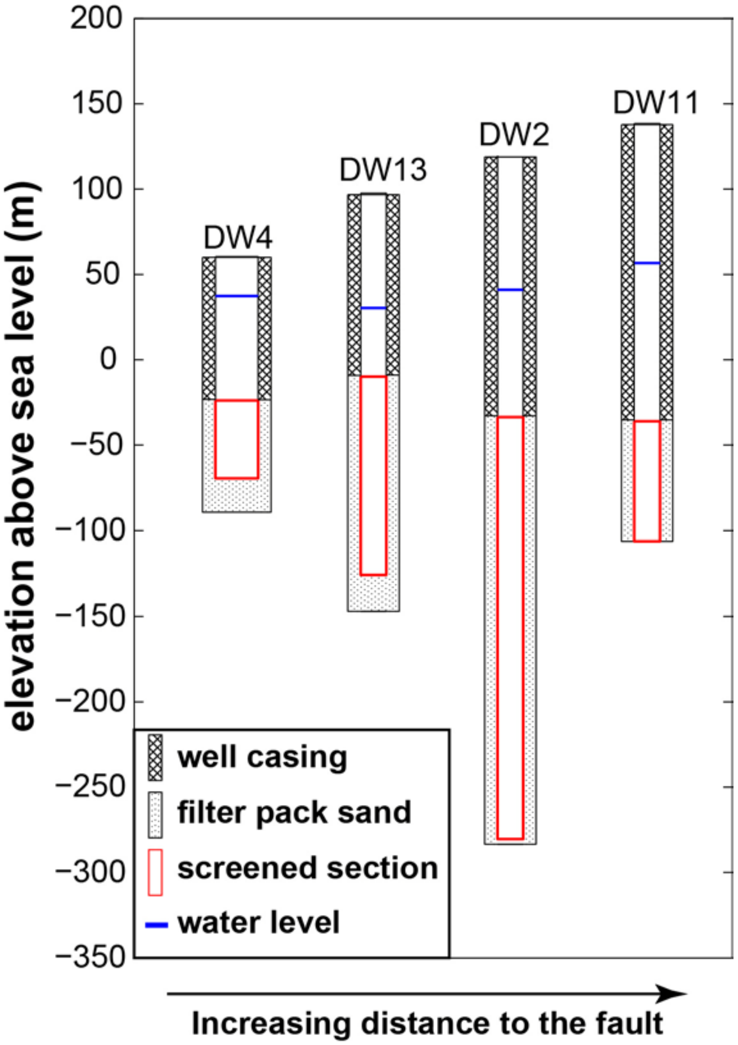

Figure 5-2. Construction of Wells. The blue line is the water level inside each well. The red rectangular indicates the screened section which allows water flow into the well. The cross rectangular indicates the casing section. The dotted rectangular is the filter pack sand.

Tidal responses are sensitive to a cylindrical volume around the well with radius proportional to $(D/\omega)^{1/2}$, where D is hydraulic diffusivity [m^2/s], and ω is frequency [1/s]. As will be shown below, the estimated scale of sensitivity for the four wells is much less than the distances between the wells, so each well provides an independent, local measure of the hydrogeologic properties. As the wells are distributed at different distances to the San Andreas Fault, the inferred hydrogeologic property of the formation surrounding each well gives the hydrogeologic properties at 4 different distances to the major fault zone.

5-4 Methods

5-4.1 Tidal response

Two different tidal response models are used in this study for different flow geometries. DW13 is close to the fault which could be a barrier for the horizontal flow. Moreover, an artesian well close to DW13 showed a vertical flow. The observed positive phase lag of DW13 cannot be caused by a horizontal flow. Overall, the flow inside DW13 is in vertical direction. We will apply a vertical flow model to calculate the equivalent hydrogeologic properties of the formation surrounding DW13, and apply a horizontal flow to calculate the equivalent hydrogeologic properties for the rest of the wells.

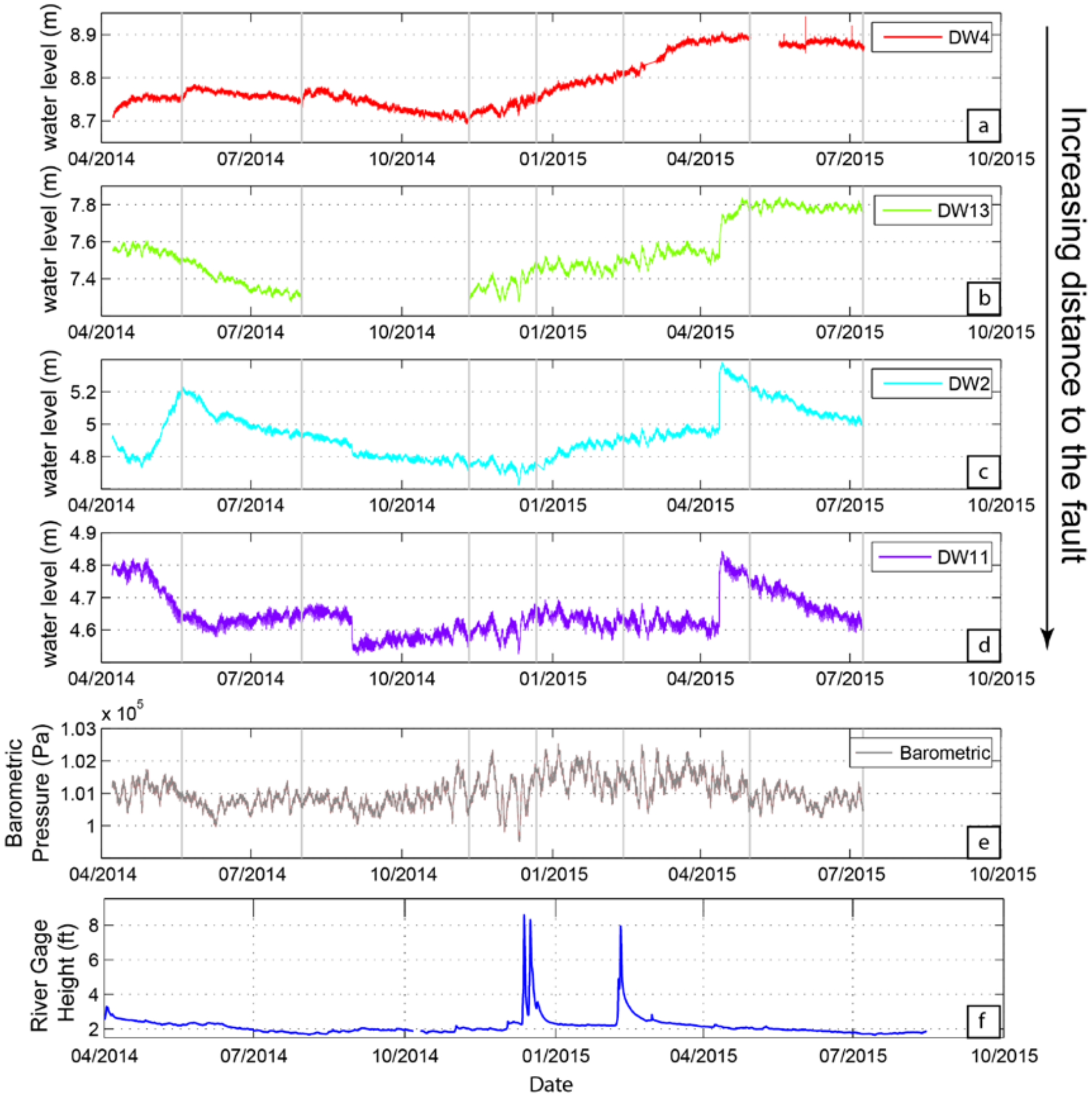

Figure 5-3. The observed water levels (a-d), barometric pressures (e), and river height of the Pajaro River at Chittenden (f). The water level records are plot in the order of distance to the fault. Well DW4 are the one closest to the fault and DW11 is furthest away. The river height of the Pajaro River at Chittenden is obtained from USGS.

5-4.1.1 Horizontal flow model

In a well-aquifer system, Earth tidal forcing generates dilatation strain in the aquifer formation to cause the water head disturbances, which pumps water in and out of the well cyclically [*Hsieh et al.*, 1987]. Finite time is needed for pore pressure to diffuse through the porous media, so the water level inside the well oscillates at the same frequency as the imposed dilatation, but with a phase lag. Permeability is a parameter controlling how easily water can travel through porous media, and storage is proportional to the formation compressibility [*Freeze and Cherry*, 1977]. Permeability and storage therefore determine the phase and amplitude of water level response to tidal forcing. At the far field of the well-aquifer system, the water head responds to the imposed dilatation strain simultaneously, so the far field head response is the pore pressure response under undrained condition which can be expressed as [*Hsieh et al.*, 1988]:

$$S_s\,|_{undrained} = \frac{\varepsilon}{h} = \frac{\varepsilon}{x}\frac{x}{h} \qquad \text{(5-1)}$$

where, $S_s\,|_{undrained}$ is the specific storage under undrained condition which is proportional to the media compressibility [1/m], ε is the tidal dilatation strain, h is the far field water head [m] and x is the water head inside water well [m]. The Hsieh *et al.* [1987] solution combining (1) with the assumptions that the aquifer is confined and laterally extends, and the aquifer media is homogenous and isotropic to compute the response of the water in an open well. Then the response of water level inside the well to the far field head perturbation can be expressed as:

$$A = \left| \frac{x_0}{\varepsilon_0} \right| = \frac{1}{S_s |_{undrain}} (E^2 + F^2)^{-1/2} \qquad (5\text{-}2)$$

$$\eta = \arg(\frac{x_0}{\varepsilon_0}) = -\tan^{-1}(F / E) \qquad (5\text{-}3)$$

where E and F are defined as,

$$E = 1 - \frac{\omega r_c^2}{2T} [\Psi Ker(\alpha_w) + \Phi Kei(\alpha_w)] \qquad (5\text{-}4)$$

$$F = \frac{\omega r_c^2}{2T} [\Phi Ker(\alpha_w) - \Psi Kei(\alpha_w)] \qquad (5\text{-}5)$$

where

$$\Psi = \frac{-[Ker_1(\alpha_w) - Kei_1(\alpha_w)]}{2^{1/2} \alpha_w [Ker_1^2(\alpha_w) + Kei_1^2(\alpha_w)]}$$

$$\Phi = \frac{-[Ker_1(\alpha_w) + Kei_1(\alpha_w)]}{2^{1/2} \alpha_w [Ker_1^2(\alpha_w) + Kei_1^2(\alpha_w)]}$$

$$\alpha_w = (\frac{\omega S}{T})^{1/2} r_w$$

$$S = bS_s |_{undrained}$$

where A is the amplitude response which is the ratio of amplitude of water level oscillation x_0 inside well to the imposed tidal dilatation strain ε_0, S is the storativity of aquifer which equals to the multiplication of the specific storage Ss [1/m] and the well open interval b [m], T is the transmissivity of aquifer [m^2/s], r_w is the radius of well [m], and ω is the angular frequency of the oscillation [rad/s]. *Ker* and *Kei* is Kelvin functions of order zero, and *Ker_1* and *Kei_1* is Kelvin functions of order one [*Hsieh et al.*, 1987]. The transmissivity *T* and storativity *S* can be inverted from the observed amplitude and phase response using Eqs. (5-1)-(5-2) by minimizing the misfit between the observed and predicted response.

To measure the amplitude and phase response of water level response to tidal forcing, we analyze the response in the time domain [*Xue et al.*, 2013]. The four largest tidal constituents, O1, K1, M2 and S2 are used to do the least-squares fit for both water level oscillation and the synthetic tidal dilatation strain. The synthetic dilatational strain data is generated by the theoretical tidal code which includes both the solid Earth and ocean-loading tides [*Agnew*, 2012]. The method and parameters of the tidal response analysis are the same as the process in Xue *et al.* [2013]. Thus we do not present the details of the processing here and refer the reader to Xue *et al.*, [2013] or Chapter 3.

5-4.1.2 Vertical flow model

When the water head gradient is vertical, the water tidal response can be simulated by periodic loading applied at the surface of a half space [Wang, 2000]. The boundary condition at the surface is drained, and at infinite depth the boundary condition is undrained. The response of water level to the tidal forcing under these conditions is:

$$A = \left| \frac{x_0}{\varepsilon_0} \right| = \frac{1}{S_s \big|_{undrain}} [1 - 2\exp(-\frac{z}{\delta})\cos\frac{z}{\delta} + \exp(-\frac{2z}{\delta})]^{1/2} \qquad (5-6)$$

$$\eta = \arg(\frac{x_0}{\varepsilon_0}) = -\tan^{-1}\left\{ \frac{\exp(-\frac{z}{\delta})\sin\frac{z}{\delta}}{1 - \exp(-\frac{z}{\delta})\cos\frac{z}{\delta}} \right\} \qquad (5-7)$$

where, $\delta = \sqrt{\frac{2c}{\omega}}$, and z is the depth from surface. c is the hydraulic diffusivity [m^2/s] which equals the division of transmissivity T and storativity S. The other terms are defined as the same in the section 5-4.1.1.

5-4.2 Error Estimation

To access how reliable the range of the estimated phase and amplitude response are, we estimate the model covariance matrix by using the data covariance matrix. The least-square linear inversion problem in this study can be expressed as:

$$\mathbf{Gm} = \mathbf{d} + \mathbf{e} \qquad (5-8)$$

and

$$\mathbf{G} = \begin{bmatrix} \sin\omega_1 t_1 & \cos\omega_1 t_1 & \ldots & \sin\omega_i t_1 & \cos\omega_i t_1 \\ \vdots & \vdots & \vdots & \vdots & \vdots \\ \sin\omega_1 t_j & \cos\omega_1 t_j & \ldots & \sin\omega_i t_j & \cos\omega_i t_j \end{bmatrix} \qquad (5-9)$$

where, ***G*** is the operation matrix, ω_i is the angular frequency of the *i*-th chosen tidal constituent, and t_j is the time, ***m*** is the model parameter matrix which is the coefficient for the combination of sine and cosine function, $\boldsymbol{d}$ is the water level oscillations, and $\boldsymbol{e}$ is the error vector of the water level data. It is a vector of $[\sigma_1^2 \quad ... \quad \sigma_i^2]$, where σ_i is the linear misfit of the *i*-th recorded data point, and the data covariance matrix is $diag\{\sigma_1^2 \quad ... \quad \sigma_i^2\}$. Then the model covariance matrix is

$$\mathrm{cov}(\mathbf{m}) = \mathbf{G}'\mathrm{cov}(\mathbf{d})\mathbf{G} \qquad (5\text{-}10)$$

The model errors determine the errors of phase and amplitude response by using error propagation. The resulted phase resolution is about 0.5° except DW4, and amplitude response resolution is 1.8×10^4 m/strain. The recorded water level of DW4 using HOBO is near the resolution of HOBO, so the resulting error, which is about 1°, is larger than for the rest of the observations. After the logger of DW4 was changed to the RBR pressure senor with 0.03 cm resolution, the estimated phase error is about 0.7°.

The errors of the equivalent T and S are constrained by the residual of forward modeling of the observed phase and amplitude response using Eqs. (5-2)-(5-3) when the flow is horizontal or using Eqs. (5-6)-(5-7) when the flow is vertical. The fitting residual of the phase is allowed to be changed by 0.25°. This number corresponds to the phase of the sampling time resolution at M2 frequency. The fitting residual of the amplitude response is allowed to vary within the error of the resolution of pressure transducer. The upper and lower bounds of the equivalent hydrogeologic properties are determined by propagating the upper and lower bounds of the phase and amplitude response to the inversion of the equivalent hydrogeologic properties.

5-5 Results

5-5.1 Spectrum of water level oscillations

To evaluate whether water level inside each water well responds to the imposed tidal forcing, we computed spectra of both water level data and barometric pressure data (Figure 5-4). The spectra of all the wells show clear tidal constituents at O1, K1, S2, and M2 (Table 2), which indicates excellent response to tidal forcing. However, the spectrum of the observed barometric data shows clear constituents at O1 and S2 which contaminate the water tidal response at these two frequencies. Therefore, we focus on the water tidal response at the frequency of M2, which has the strongest component with little contamination from the barometric loading, to infer the hydraulic storage (S) and transmissivity (T). All of the wells other than DW4 have larger spectral amplitude at M2 than S2, so the tidal response analyses of the M2 constituent of these three wells are reliable. The interpretation of the tidal response of DW4 at M2 requires more caution because of the low signal to noise ratio of M2.

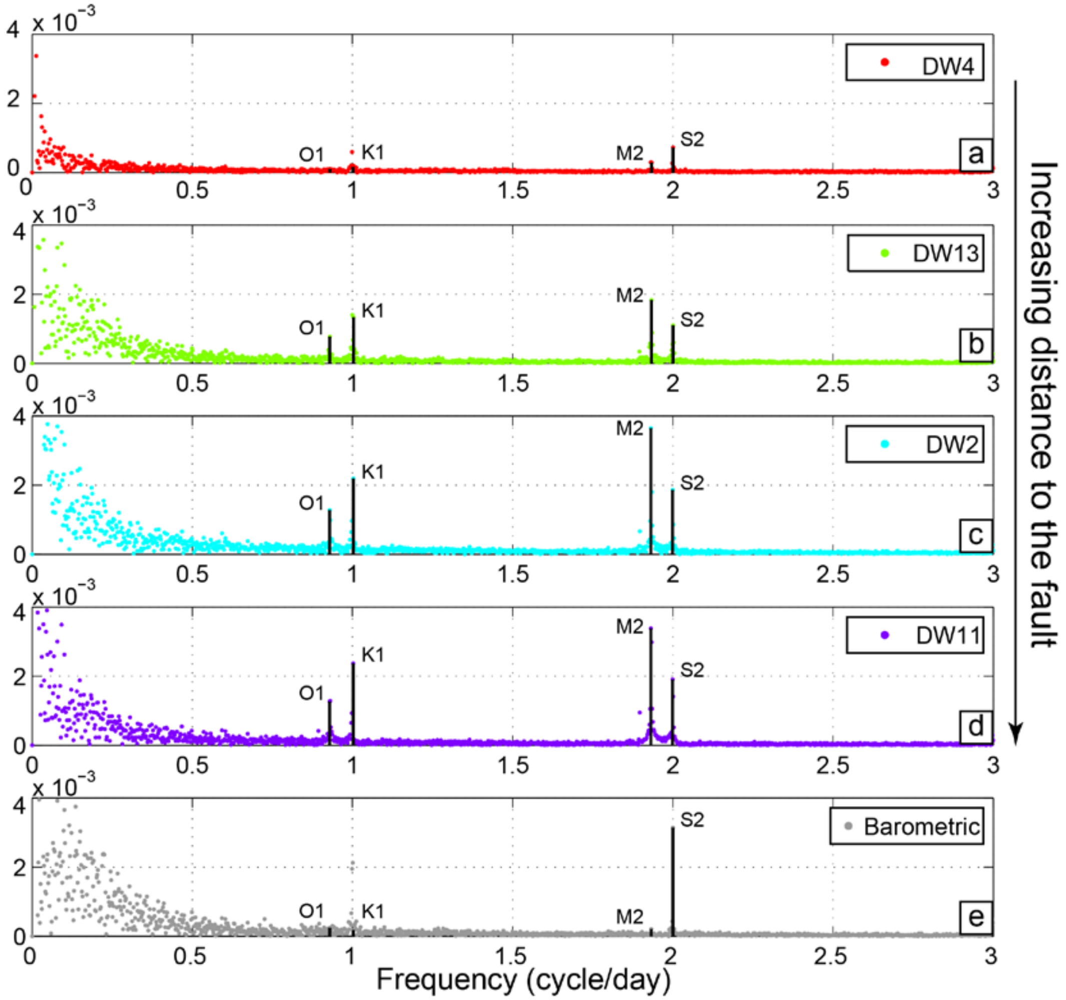

Figure 5-4. The spectrum of water level oscillations (a-d) and barometric data (e). The vertical black lines indicate the K1, O1, M2 and S2 tidal constituents.

5-5.2 Tidal response

The phase responses are at the range of -17^o to 3^o. The phase responses show an increasing phase lag (increasing absolute number) trend as the well is far away from the fault zone except DW4. The phase response of DW4 is highly variable. This scatter is due to the strong effect of the barometric pressure of the S2 component in this site as discussed earlier and the limitation of the logger resolution. Even though the amplitude of water level oscillation inside DW4 is close to the resolution of the HOBO, and therefore it to resolve the phase information accurately for this data. The phase response of DW4 measured by the HOBO therefore will not be interpreted, and we prefer to use the phase response of DW4 measured by RBR to constrain the hydrogeologic properties of the formation surrounding DW4. The phase response of DW4 measured by RBR is about -15° (Figure 5-5, the dots after May, 2015). The small positive phase lag of DW13 might be due to the effects of a vertical flow [*Roeloffs*, 1996], so we will use the vertical flow model to calculate the equivent hydrogeologic properties of DW13 in the later section. The magnitude of the observed water level oscillations are < 1cm, so the corresponding ratio between the measured water level and the theoretical tidal dilatation strain are of the order of magnitude of 10^4 m/strain.

5-5.3 Hydrogeologic Properties

The hydraulic transmissivity (*T*) and storativity (*S*) determine the phase and amplitude responses, the in-situ *T* and *S* therefore can be inferred from the measured phase and amplitude response. The positive phase lag of DW13 and a vertical flow inside an artesian well close to DW13 site indicate a vertical flow inside DW13, so we use the vertical flow model to calculate the equivalent hydrogeologic properties of the formation surrounding DW13. When the phase is close to zero degree, the vertical flow model can only give the upper bound of the equivalent hydraulic properties, so we only consider the best-fit results of hydrogeologic properties when the phase is about zero for the DW13.

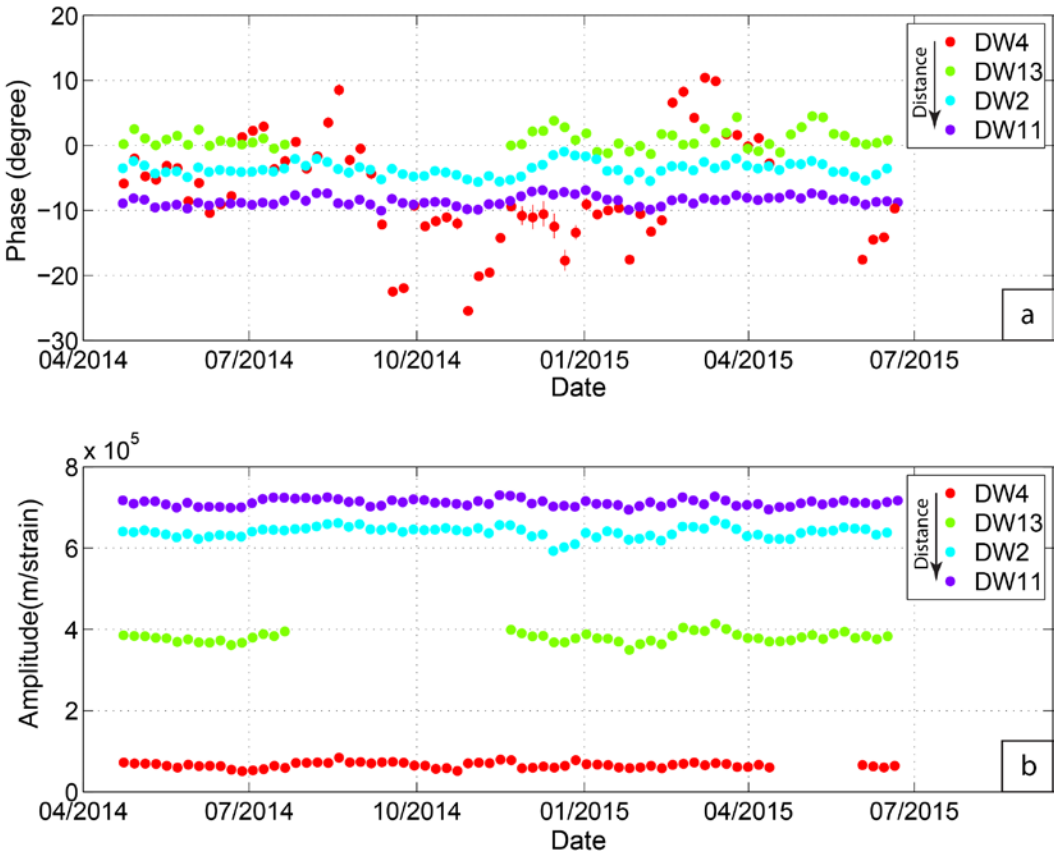

Figure 5-5. (a) Phase response and (b) amplitude response. The error bars are difficult to see because of the small scale. The scale of phase error is about 0.5°-1°, and the scale of amplitude response is about 10^5 m/strain. Different colors show the response for different wells, and the legend is in the order of increasing distance to fault zone.

The inverted transmissivity and storativity depend on both the thickness of the well open interval and the hydrogeologic properties of the formation. To avoid the effect of different well completions (Figure 5-2), T and S are converted to permeability (k) and specific storage (S_s) by:

$$k = \frac{\mu}{\rho g d} T \qquad (5\text{-}11)$$

$$S_s = S / d \qquad (5\text{-}12)$$

where μ is the fluid dynamic viscosity, d is the thickness of the open interval of the well and ρ is the density of fluid [*Freeze and Cherry*, 1977]. Using $\mu=10^{-3}$ Pa s at 20°C, $\rho=10^3$ kg/m^3, g=9.8 m/s^2, the calculated hydrogeologic properties of the formation surrounding these four wells are shown in Table 5-3. The permeability of DW4 and DW13 is larger than that of DW2 and DW11 at a factor of ~10. The inferred specific storage shows DW4 and DW13 have statistically larger specific storage than that of well DW13 and DW2. The specific storage of DW4 is larger than that of DW2 and DW11 at a factor of ~10, and the specific storage of DW13 is larger than that of DW2 and DW11 at a factor of 2. The measured diffusivity is about 10^{-2} m^2/s for all of the wells. In combination, the data suggests that there is heterogeneity in hydrogeologic properties in the rocks surrounding these four wells. The apparent trend in permeability and storativity with distance to the fault may indicate the influence of fracturing associated with the fault zone.

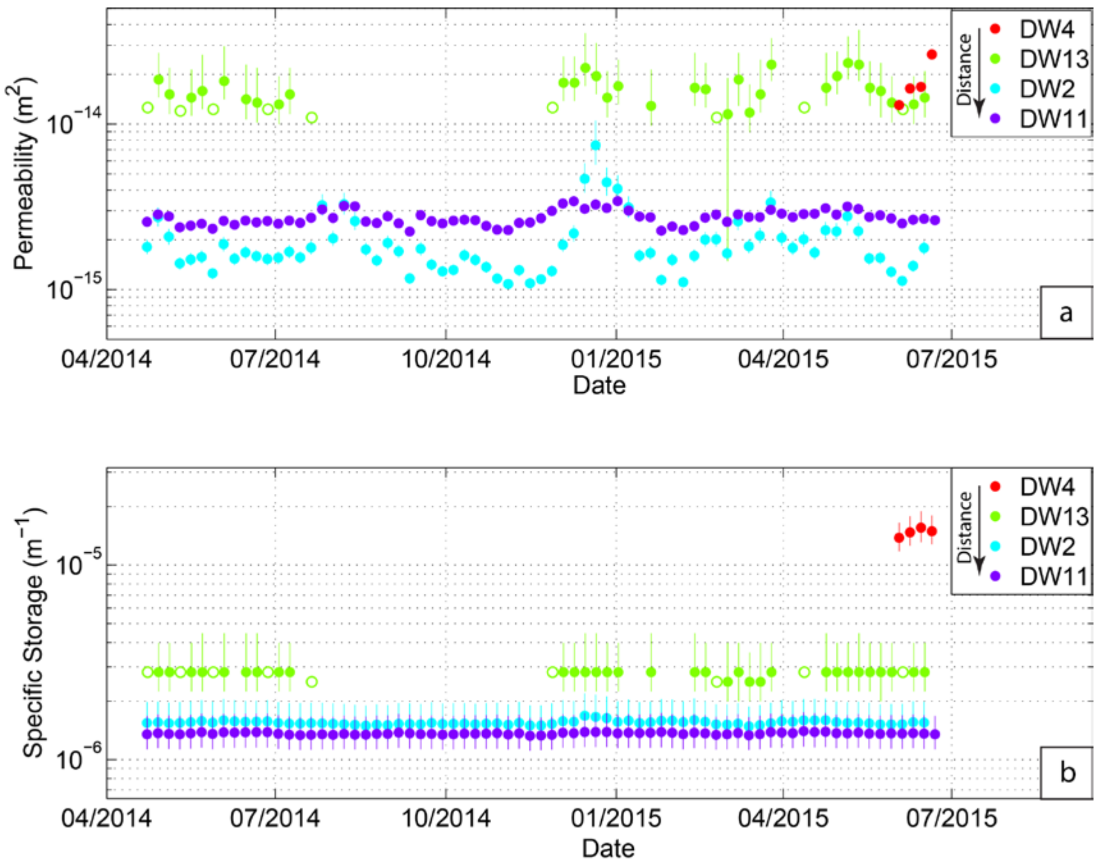

Figure 5-6. The measured permeability (a) and specific storage (b). Different colors show the response for different wells, and the legend is in the order of increasing distance to the fault. The open circles for DW13 are the data with phase lag <0.25°, which are the best fit of observed response. Those open circles indicate the upper bound of the permeability.

5-5.4 Response to Earthquakes

A sequence of local earthquakes with magnitudes as large as 4.2 occurred within 30 km of the quarry between 20 November and 6 December 2014 (Figure 5-1B). It is hard to separate the response to individual earthquakes in the sequence, because the time window of the phase response analysis is ~29.5 days. The continuous phase response of all wells except DW4 have subtle increases in that interval. As previously discussed, the temporal phase response change of DW4 is not reliable in this time interval.

To clearly separate the properties before and after the earthquakes, we invert the data omitting the segment overlap from Oct. 20 to Dec.6 (Figure 5-7). The phase response had a slight increase right after the M3.9 earthquake on Dec. 6, and recovered the background level within 2 months. The change of phase lag is measured by the difference between the first data point after the earthquake and the averaged phase value before the earthquake. The change of phase for DW13 and DW2 is 2.7° and 3.0° separately, and the change of phase for DW11 is 1.7°. The amplitude changes are too subtle, so we will not interpret them (Figure 5-6). The change of the equivalent permeability is calculated from the changes of phase response. After the sequence of earthquakes, the permeability of DW13 is increased by 38%. The permeability change of DW2 is 1.6 times as big as the transmissivity before the earthquakes. The permeability of DW11after the sequence of earthquake is increased by 19% of the value before the earthquakes.

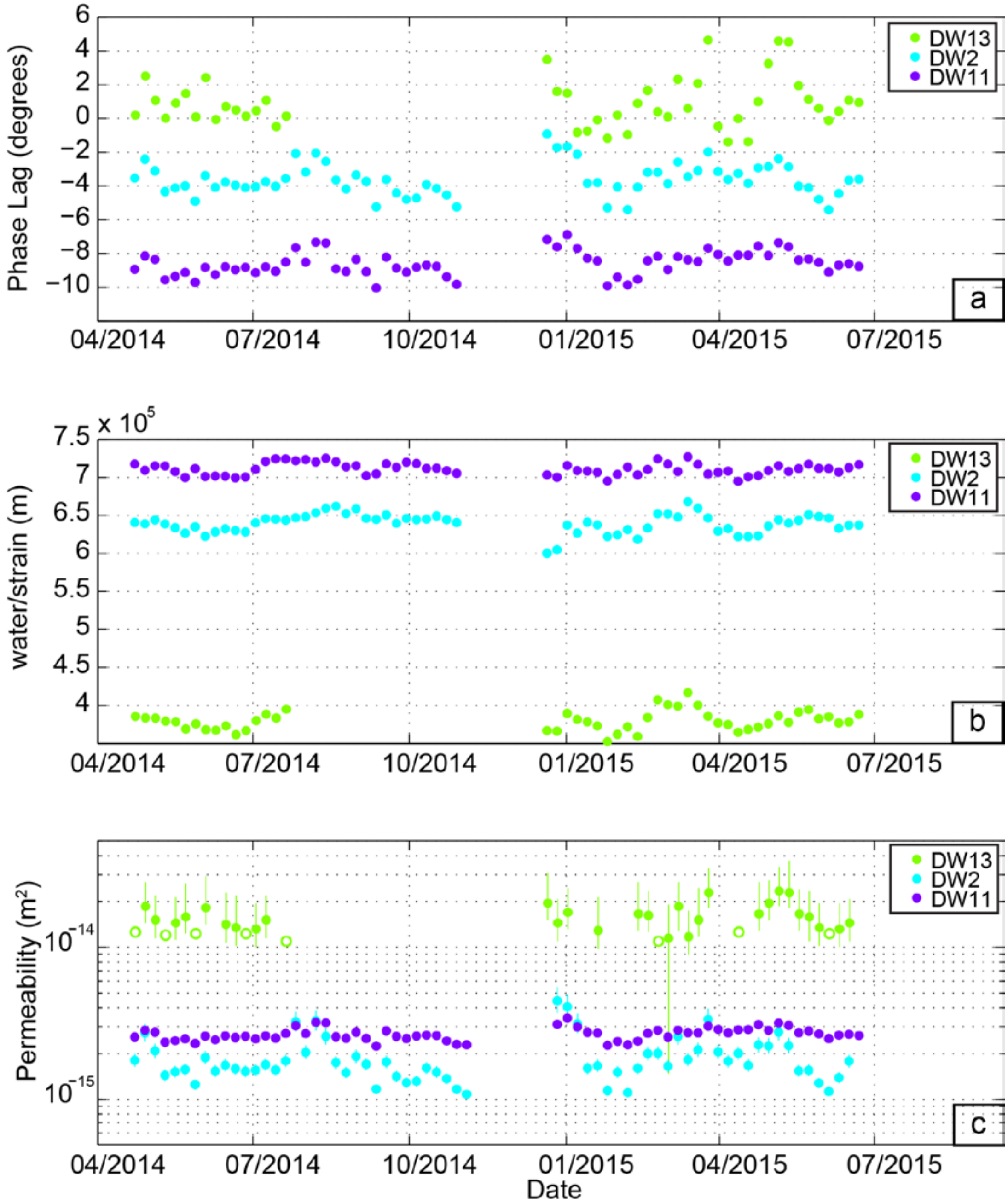

Figure 5-7. Response to earthquakes: (a) phase response;(b) amplitude response and (c) the corresponding permeability change. The data before 20 November and that after 6 December are analyzed separately to avoid the overlapping of the data before and after the local earthquakes. The open circles of DW13 are the data with phase lag <0.25°.

5-6 Discussion

5-6.1 Hydrogeologic Properties

We have estimated the permeability of rock near the San Andreas Fault to be about 10^{-14} m^2 which is a relative high number compared to the permeability of other fault zones. The permeability from the isotropic model gives the lower bounds on the highest permeability of the system and therefore is a conservative estimate [*Xue et al.*, 2013]. The laboratory measured permeability from core samples of the Nojima fault zone indicates the fault core permeability is 10^{-19} to 10^{-18} m^2, and damage zone permeability is 10^{-17} and 10^{-16} m^2 [*Lockner et al.*, 2000]. The in-situ measured permeability of Wenchuan rupture zone is about 10^{-16} m^2 [*Xue et al.*, 2013]. The laboratory measured permeability of granite at a range of 10^{-16}-10^{-21} m^2 [*Brace*, 1980]. Our measured permeability is at the high end of the laboratory values. This indicates our measured media is dominated by mesoscale fractures. The measured hydrogeologic diffusivity of this site is about ~ 10^{-2} m^2/s, which is similar to the value of 2.4×10^{-2} m^2/s inferred from the Wenchuan fault [*Xue et al.*, 2013].

5-6.2 Hydrogeologic Architecture

The observed amplitude response decreases as the wells move farther away from the fault zone, and the observed phase lag increases (absolute number increases) when the wells are far away from the fault zone except DW4. To first order, the amplitude response is controlled by the storage S and the phase lag is controlled by the transmissivity T. Therefore, a naive interpretation of the data might be that both storage and transmissivity increase close to the fault. However, the storage S can contributes to phase lag and the transmissivity T can also affects the amplitude response. Increasing transmissivity can also increase the amplitude response as the well drains more easily during each oscillation, and larger storage can also reduce the phase lag as the aquifer releases more water during each oscillation. Therefore, we need to assess whether the observed tidal response patterns could potentially be explained by varying only S_s or T without a contribution from the other factor. To do so, we fix one of S_s and T and invert for the other parameter, then compare the resulting response to the data.

For fixed specific storage for all the wells, the decreasing phase lag closer to the fault except DW4 suggests an increasing transmissivity T closer to the fault. The increasing transmissivity T would result in an increasing amplitude of water level oscillations. This is opposite to the observed trend of the amplitude response. Overall, both the trend of the amplitude and phase response cannot be caused by the change of transmissivity only.

The alternative case of specific storage varying requires more calculation. We calculate the responses for a fixed transmissivity with only specific storage varying (Figure 5-8). We invert for the corresponding storativity for the observed phase lag, then compare the synthetic amplitude response calculated the inverted storativity and the fixed transmissivity to the observed amplitude response. Even though the variation of storage only can result the same trend as the observed trend of amplitude response, the absolute number of the synthetic amplitude response is too large to be close to reality. Over all, the comparison indicates the observed systematic changes of phase and amplitude response has to be the results of the combination of the changes of *S* and *T*.

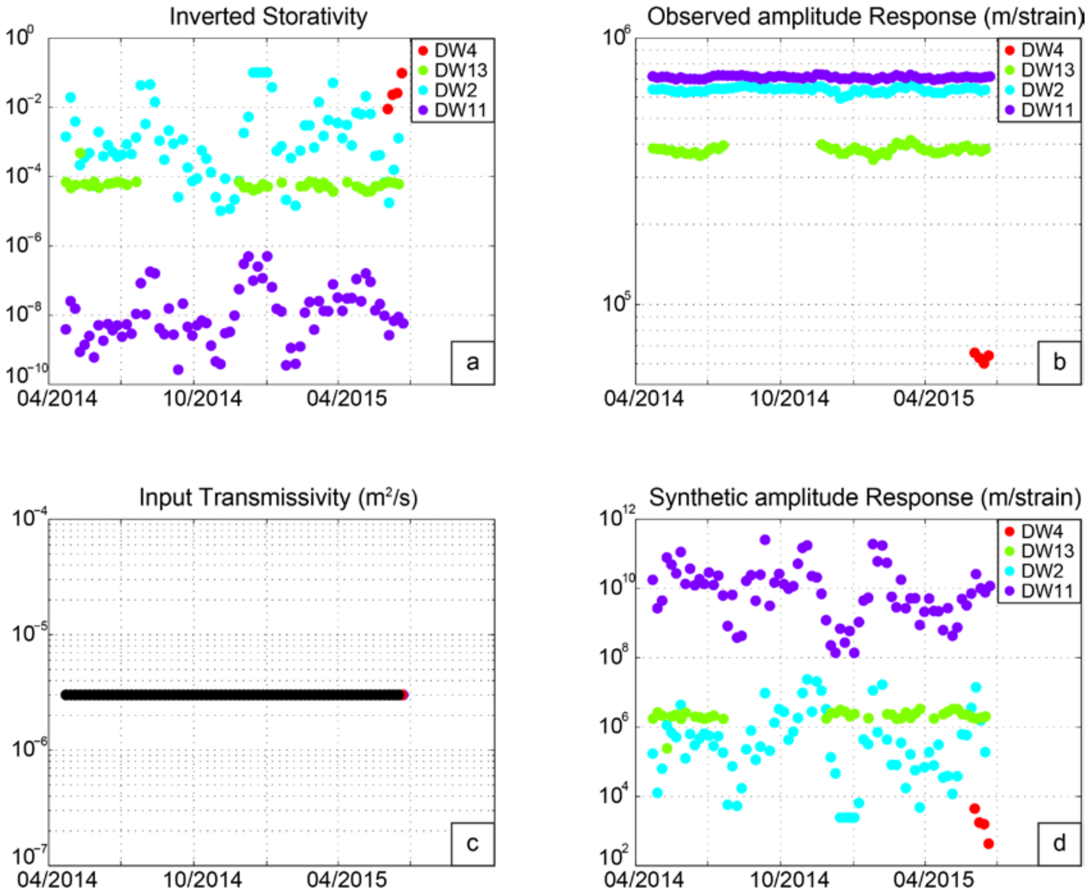

Figure 5-8. Evaluation of fixed transmissivity. (a) The inverted storativity by using phase response and the fixed transmissivity; (b) the observed amplitude response; (c) the input fixed transmissivity which is the average transmissivity of all the wells; (d) the synthetic amplitude response by using the fixed transmissivity and the inverted storativity.

The measured *k* indicates sites far away from the fault have slightly smaller *k* than the places which are closer to the fault. The measured S_s surprisingly shows a clear decreasing trend outward from the fault (Figure 5-6) which indicates the formation has higher compliance when it is closer to fault zone. Based on the inferred diffusivity of the formation surrounding each well, the length scale surrounding each well over which the tidal response samples is several tens of meters (details see table 3). The distances between any two wells are about several hundreds to thousands of meters. The length scale of each well over which the tidal response is sampled is much smaller than the distances between wells, therefore the radius of the influence zone of each well are non-overlapping regions. There is no trend in the sampled depth of wells (Figure 5-2), so the observed trend of hydrogeologic properties is unlikely caused by the heterogeneity of the depth to the surface. A zone close sampled within 40 m of the fault has different hydrogeologic properties from the formation with distance >400 m to the fault. The different hydrogeologic properties of this localized zone might be related to the fault zone fracture density distribution which decays with the distance to the fault [*Savage and Brodsky*, 2011].

The contrast in specific storage of fault zone affects response to applied stress. The rigidity contrast of a fault zone results in the fault zone with higher compliance having a larger elastic response than the surrounding formation. Similar compliance contrasts have been observed in the nearby faults of the 1999 Hector Mine earthquake [*Fialko et al.*, 2002]. The observed induced deformation over kilometers wide zone on the nearby faults of the Hector Mine earthquake could be caused by a rigidity contrast of 0.4-0.6. Guided seismic waves also show the Landers Fault zone has a 100-300 m wide weaker zone extending tens of kilometers deep with seismic wave velocities reduced up to 30%–50% [*Li et al.*, 1994; *Li et al.*, 1998]. This velocity reduction suggests a corresponding modulus contrast of a factor of 0.5-0.7 assuming there is no change of rock density. Our observed hydrogeologic specific storage contrast indicates a bulk modulus contrast of a factor of 0.1-0.5 which is comparable to the results of the mentioned geodetic and seismic observations. There is also an observation showing a systematic reduction of pore pressure response near the San Jacino Fault [Barbour, 2012]. All of these observations together indicate the fault zone is mechanically weaker than the surrounding rocks.

The contrast in specific storage may also cause a pressure gradient to drive flow though the fault zone and surrounding rock when seismic waves pass [*Brodsky and Prejean*, 2005]. This resultant flow can cause permeability enhancement as shown in laboratory oscillation experiments [*Candela et al.*, 2015]. To assess whether the flow driven by seismic waves can cause permeability enhancement based on our observed in-situ specific storage contrast, we utilize the same model as shown in the study of Brodsky and Prejean, [2005] of two abutting media with distinct storages. This model calculates the induced hydraulic heads in faults and the surrounding rocks with different storages caused by dilatational seismic strain. Based on this model, the flow rate can be calculated by:

$$q = -\lambda K\left(\frac{1}{S_s^f}\frac{\frac{\sqrt{i\omega\kappa_r}}{b} + i\omega}{\frac{\sqrt{i\omega\kappa_r}}{b}\frac{S_s^r}{S_s^f}} - \frac{\theta_\infty}{S_s^r}\right)\exp(-\lambda x) \tag{5-13}$$

$$\text{wher, } \lambda = \sqrt{\frac{i\omega}{\kappa_r}}$$

where, q is the flow rate [m/s], K is hydraulic conductivity [m/s], S_s^f and S_s^r is the specific storage for fault zone and surrounding rock separately [m^{-1}], ω is angular frequency of the imposed strain [rad/s], θ_∞ is the imposed strain, and κ_r is the diffusivity of the rock [m^2/s] and b is the fault zone width [m] [*Brodsky and Prejean*, 2005].

Assuming the fault zone has a 40 m wide weak zone with a specific storage of 1.47×10^{-5} m^{-1}, and the surrounding rock has a smaller specific storage of 1.36×10^{-5} m^{-1} and a permeability of 10^{-15} m^2, the resulting maximum flow rate from 10 s wave with strain amplitude of 1.2×10^{-6} which was the largest recorded seismic strain, is 9×10^{-8} m/s near the edge of the fault zone. The flow in this model is extremely local and decays to a negligible level within 10 diffusion lengths (~0.1 m) of the boundary for the high frequency seismic waves. Permeability enhancement was observed in laboratory experiments for flow velocities as low as 5×10^{-6} m/s [*Candela et al.*, 2014]. The flow rate inferred by the observed storage architecture is lower than the experimental range resolvable in the laboratory experiments, which indicates that further experiments are needed to investigate the potential effects of lower flow rates.

The measured diffusivity is 10^{-2} m/s which is the same order of magnitude of that of the Wenchuan Earthquake fault zone. It is interesting that the high diffusivity at the location inside the fault zone is the same as the place outside, even though the permeability and specific storage have larger contrasts. This indicates the diffusivity structure of fault zone is unexpectedly uniform due to the competing effect of permeability and specific storage. This might suggest the accumulated pore pressure during inter-seismic period distributes a broad zone rather than a narrow range.

5-6.3 Response to earthquakes

The most significant response to earthquakes was after 6 December 2014. All of them have a phase change of 1.7°-3.0° degree except DW4. The one which is closer to the fault zone has a larger permeability change. This different response might be due to the fracture density of the fault zone. The laboratory experiments show the enhanced permeability for the same loading is larger when the rock has more fracture [*Candela et al.*, 2014]. The behavior of the response to different earthquakes is not clear in our study. During our observations, the shaking of the local earthquakes are larger than Napa based on the local seismometers, and there is no significant response to the Napa earthquake. Since the response cannot distinguish the earthquakes occurred between 20 November 2014 and 6 December 2014, there is no well resolved response to different earthquakes.

5-7 Conclusions

The observed hydrogeologic architecture of the San Andreas Fault Zone in the Logan Quarry indicates a localized region near the fault zone which differs from the surrounding rock. Sites within ~40 m of the fault zone have a larger specific storage and a larger permeability than those are more than 400 m away. This hydrogeologic property structure could be related to the fracture density distribution of the fault zone.

The measured specific storage structure is novel and has consequences for fault mechanics. It indicates the place near fault zone has a different mechanical property. The competing effect of the permeability and specific storage changes results a relatively uniform, high value of diffusivity of 10^{-2} m^2/s. This uniform diffusivity structure suggests that the accumulated pore pressure during interseismic period is distributed over a broad region. Our study shows the utility of the water tidal response for measuring the fault zone hydrogeologic architecture in situ and studying the response behavior of fault zone hydrogeologic properties to earthquakes.

Table 5-1

Well Name	Radius ($\times 10^{-2}$ m)	Length of open interval (m)	Water level depth (m)	Top of the open interval to the water table (m)	Distance to the fault (m)
DW4	7.62	45.72	37.41	46.4	30.5
DW13	2.54	115.82	32.72	73.8	36.6
DW2	2.54	246.9	41.03	111.3	426.7
DW11	2.54	70.1	56.70	117	548.6

Table 5-2

Name of tidal constituents	Period (hour)	Frequency (cycle per day)
O1	25.819	0.9295
K1	23.934	1.0027
M2	12.421	1.9324
S2	12.000	2.0000

(Data from Agnew, 2007[*Agnew*, 2007])

Table 5-3

Well Name	R* (m)	k (m^2)	S_s (1/m)	D ($\times 10^{-2}$ m^2/s)	L* (m)
DW4	21.7	1.6×10^{-14}	1.5×10^{-5}	1.1	30.5
DW13	49.4	1.6×10^{-14}	2.8×10^{-6}	5.5	36.6
DW2	21.3	1.6×10^{-15}	1.5×10^{-6}	1.0	426.7
DW11	26.8	2.2×10^{-15}	1.4×10^{-6}	1.6	548.6

*****R is diffusion length which controls the radius of influence and L is the distance to the fault zone.

5-8 Acknowledgements

This project is supported by NSF grant EAR1220642. We would like to thank the people help me on the Logan Quarry Logan: Patrick Fulton, Vincent Allègre, Thibault Candela, Reed Carter, Barbara E. John and Han Yue. We also thank Jon Erskin and Graniterock for their generous collaboration.

5-9 References

Agnew, D. C. (2007), Earth tides, *New York: Elsevier*, 163-195.

Agnew, D. C. (2012), SPOTL: Some Programs for Ocean-Tide Loading, edited.

Andrews, D. (2002), A fault constitutive relation accounting for thermal pressurization of pore fluid, *Journal of Geophysical Research: Solid Earth (1978–2012)*, *107*(B12), ESE 15-11-ESE 15-18.

Barbour, A. J. (2012), Systematic reduction of pore pressure response near the San Jacinto fault. AGU Fall Meeting Abstracts. Vol. 1..

Brace, W. F. (1980), Permeability of crystalline and argillaceous rocks, *International Journal of Rock Mechanics and Mining Sciences & Geomechanics Abstracts*, *17*(5), 241-251.

Brodsky, E. E., and S. G. Prejean (2005), New constraints on mechanisms of remotely triggered seismicity at Long Valley Caldera, *Journal of Geophysical Research: Solid Earth (1978–2012)*, *110*(B4).

Byerlee, J. (1993), Model for episodic flow of high-pressure water in fault zones before earthquakes, *Geology*, *21*(4), 303-306.

Caine, J. S., J. P. Evans, and C. B. Forster (1996), Fault zone architecture and permeability structure, *Geology*, *24*(11), 1025.

Candela, T., E. E. Brodsky, C. Marone, and D. Elsworth (2014), Laboratory evidence for particle mobilization as a mechanism for permeability enhancement via dynamic stressing, *Earth and planetary science letters, 392*, 279-291.

Candela, T., E. E. Brodsky, C. Marone, and D. Elsworth (2015), Flow rate dictates permeability enhancement during fluid pressure oscillations in laboratory experiments, *Journal of Geophysical Research: Solid Earth*, 2014JB011511.

Elkhoury, J. E., A. Niemeijer, E. E. Brodsky, and C. Marone (2011), Laboratory observations of permeability enhancement by fluid pressure oscillation of in situ fractured rock, *Journal of Geophysical Research*, *116*(B2), B02311.

Fialko, Y., D. Sandwell, D. Agnew, M. Simons, P. Shearer, and B. Minster (2002), Deformation on nearby faults induced by the 1999 Hector Mine earthquake, *Science*, *297*(5588), 1858-1862.

Freeze, R. A., and J. A. Cherry (1977), *Groundwater*, Prentice-Hall.

Hsieh, P. A., J. D. Bredehoeft, and J. M. Farr (1987), Determination of aquifer transmissivity from earth tide analysis, *Water Resources Research*, *23*(10), 1824-1832.

Hsieh, P. A., J. D. Bredehoeft, and S. A. Rojstaczer (1988), Response of well aquifer systems to Earth tides: Problem revisited, *Water Resources Research*, *24*(3), 468-472.

Hubbert, K. M., and W. W. Rubey (1959), Role of fluid pressure in mechanics of overthrust faulting: I. Mechanics of fluid-filled porous solids and its application to overthrust faulting, *Bulletin of the Geological Society of America*, *70*(2), 115.

Lawson, A. C., and H. F. Reid (1908), *The California Earthquake of April 18, 1906: Report of the State Earthquake Investigation Commission*, Carnegie institution of Washington.

Li, Y.-G., K. Aki, J. E. Vidale, W. H. K. Lee, and C. J. Marone (1994), Fine Structure of the Landers Fault Zone: Segmentation and the Rupture Process, *Science*, *265*(5170), 367-370.

Li, Y.-G., J. E. Vidale, K. Aki, F. Xu, and T. Burdette (1998), Evidence of shallow fault zone strengthening after the 1992 M7. 5 Landers, California, earthquake, *Science*, *279*(5348), 217.

Lockner, D., H. Naka, H. Tanaka, H. Ito, and R. Ikeda (2000), Permeability and strength of core samples from the Nojima fault of the 1995 Kobe earthquake, paper presented at Proceedings of the International Workshop on the Nojima Fault Core and Borehole Data Analysis, US Geol. Sur.

Rice, J. R. (1992), Fault stress states, pore pressure distributions, and the weakness of the San Andreas fault, *International Geophysics*, *51*, 475-503.

Roeloffs, E. (1996), Poroelastic techniques in the study of earthquake-related hydrologic phenomena, *Advances in geophysics*(37), 135-195.

Ross, D. C. (1970), Quartz gabbro and anorthositic gabbro: Markers of offset along the San Andreas fault in the California Coast Ranges, *Geological Society of America Bulletin*, *81*(12), 3647-3662.

Savage, H. M., and E. E. Brodsky (2011), Collateral damage: Evolution with displacement of fracture distribution and secondary fault strands in fault damage zones, *Journal of Geophysical Research: Solid Earth (1978–2012)*, *116*(B3).

Segall, P., and J. R. Rice (1995), Dilatancy, compaction, and slip instability of a fluid-infiltrated fault, *Journal of Geophysical Research: Solid Earth*, *100*(B11), 22155-22171.

Wang, H. F. (2000). Theory of linear poroelasticity. Princeton Series in Geophysics, Princeton University Press, Princeton, NJ.

Xue, L., et al. (2013), Continuous Permeability Measurements Record Healing Inside the Wenchuan Earthquake Fault Zone, *Science*, *340*(6140), 1555-1559.

Conclusions

In this thesis, I present investigations of fault zone behavior during earthquake cycles from hydrogeologic, geothermal and geodetic perspectives. The important accomplishments and conclusions are summarized as follows:

1. InSAR data combined with GPS data has a potential to resolve a long-wave length, small-deformation signal in a subduction zone. The GPS-InSAR integrated model shares similar long wavelength characteristics with the GPS-only model, but it improves model resolution and reveals more refined features at local scales. This allows for improved comparison with local seismic and aseismic events. The resultant fine feature comparison can help us learn the plate interface frictional properties and the mechanisms controlling the coupling variations.

2. The repeat temperature measurements of Wenchuan Fault Scientific Drilling indicate that the total energy dissipated frictionally at the locale penetrated by the WFSD-1 borehole is <29 MJ/m^2 and the dissipated energy on the previously identified fault surface is <1.2 MJ/m^2. The upper bound for the entire zone (29 MJ/m^2) is less than would be anticipated with a coefficient of friction of 0.6, and could be consistent with the range of coefficients of friction seen in dynamic weakening experiments. Other studies have inferred dramatic weakening for the Wenchuan fault material based on laboratory studies of fault zone rocks from surface outcrops subject to high-velocity shear. The high organic and clay content or presence of graphite may be critical factors. The Wenchuan earthquake fault appears to have been weak during slip.

3. The Wenchuan Fault Scientific Drilling project captured the permeability evolution in the critical post-earthquake period as damage heals and the stage is set for the next earthquake. The unexpectedly high average hydraulic diffusivity (2.4×10^{-2} m^2/s) measured here also implies substantial fluid circulation in the evolving fault zone. For most of the observation period, the permeability decreases rapidly as the fault heals. The trend is interrupted by abrupt permeability increases attributable to shaking from remote earthquakes. These direct measurements of the fault zone reveal a process of punctuated recovery as healing and damage interact in the aftermath of a major earthquake.

4. Fault zones have complex hydrogeologic architectures. Water well tidal responses provide a probe to measure the in situ hydrogeologic properties of fault zones. Even though the fault zone may be highly anisotropic, the inferred permeability is in a limited range. The permeability derived from an isotropic model gives the lower bound on the highest permeability.

5. We observed a high storage, high permeability zone near the San Andreas Fault. The contrast of storage creates a flow response to seismic shaking that can be sufficient to cause permeability enhancement. We also observed near the San Andreas fault that the competing effects of permeability and storage result in a relative uniform distribution of diffusivity which is similar to the Wenchuan Fault ($\sim10^{-2}$

m^2/s). Diffusivity is the controlling parameter for the buildup of the pore pressure. The buildup of pore pressure depends on different length scales of the fault zone hydrogeologic architectures during different stages of earthquake cycles. The hydrogeologic architecture of the fault slip zone controls the development of the pore pressure during the rupture process, and that of the fault damage zone controls the accumulated pore pressure during the interseismic period. Therefore, the utilization of open wells and well packers inside fault slip zones would give the hydrogeologic architecture of a fault zone on different scale. This strategy would provide a comprehensive understanding of the pore pressure role in the development of the faulting process.